



THE UNIVERSITY *of* EDINBURGH

This thesis has been submitted in fulfilment of the requirements for a postgraduate degree (e. g. PhD, MPhil, DClinPsychol) at the University of Edinburgh. Please note the following terms and conditions of use:

- This work is protected by copyright and other intellectual property rights, which are retained by the thesis author, unless otherwise stated.
- A copy can be downloaded for personal non-commercial research or study, without prior permission or charge.
- This thesis cannot be reproduced or quoted extensively from without first obtaining permission in writing from the author.
- The content must not be changed in any way or sold commercially in any format or medium without the formal permission of the author.
- When referring to this work, full bibliographic details including the author, title, awarding institution and date of the thesis must be given.

On the Transport Mechanisms of Fluids under Nanoscale Confinements

Carlos Manuel Corral-Casas



Doctor of Philosophy

THE UNIVERSITY OF EDINBURGH

2023

Abstract

The presence of fluids confined to the nanoscale has been known for some time in nature, as observed in geological formations, e.g. light hydrocarbon fluids trapped in shale reservoirs, or in biological systems, e.g. water in aquaporins. However, it is only recently that technological advances have stimulated interest in studying fluid behaviour under such conditions in more detail, due to the disruptive potential of engineering applications at these scales. Three important characteristic lengths can be identified in these flows, namely the molecular mean free path λ (denoting the average distance travelled by particles between collisions), the diameter of fluid constituent particles σ , and the channel size L . At the microscale, λ may become comparable to L , leading to an increased collision frequency of gas molecules with the confining walls rather than with other particles. In this scenario, the gas is no longer in quasi-local thermodynamic equilibrium state as assumed by continuum fluid dynamics, and the Boltzmann equation must be used to accurately describe its behaviour. At the nanoscale, where L is comparable to σ , excluded volume effects and non-locality of collisions become significant. Consequently, the Boltzmann description becomes invalid and alternative kinetic models, such as the Enskog equation, or a more fundamental approach, such as molecular dynamics simulations, must be considered. This thesis aims to contribute to the understanding of transport phenomena at the nanoscale, spanning fluid conditions from the dense to the rarefied gas, and considering different channel sizes, geometries and surface roughnesses. In order to do so, a fluid composed of hard spheres confined between mathematical surfaces has been studied because, despite its simplicity, this model retains the essential physics of more realistic systems.

Self-diffusion of atoms is the simplest possible transport mechanism, and yet it is not fully understood in the context of molecularly confined flows. Firstly, in this thesis, a systematic study of this process was carried out for a fluid within a slit geometry, delimited by two infinite parallel plates. One of the most distinctive features of the fluid behaviour in confined conditions is the preferential fluid structuring that occurs next to the boundaries, due to the limited mobility of particles in the normal dimension to the wall. To clarify a source of debate in the literature, it is proved that, despite the strong fluid inhomogeneities, the self-diffusivity based on the Einstein relation can still be used to describe Fickian diffusion under molecular confinements, the latter being explicitly computed in simulations by tracking the dynamics of tagged particles. The interplay of the underlying diffusion mechanisms, i.e. molecular and Knudsen diffusion, is then identified, by differentiating between fluid-fluid and fluid-wall collisions. The key finding

is that the Bosanquet formula, previously used for describing the diffusive transport of rarefied gases, also provides a good semi-analytical description of self-diffusivities for dense fluids under tight confinements, as long as the channel size is not smaller than five molecular diameters. Importantly, this allows one to predict the self-diffusion coefficient in a wide range of Knudsen numbers, including the transition regime, which was not possible before.

Although diffusion is believed to dominate the fluid transport at the nanoscale, it is shown that the Fick first law fails to describe the surprising fluid behaviour that occurs within confined straight channels. For example, since Knudsen’s experimental work circa 1910, it has been known that the Poiseuille mass flow rate along microchannels features a stationary point as the fluid density decreases, referred to as the Knudsen minimum. However, when the characteristic length L is further decreased, this minimum has been reported to disappear and the mass flow rate monotonically increases over the entire range of flow regimes. In this work, it is shown for the first time, using analytical means, that this vanishing occurs because the decay of the mass flow rate, due to the decreasing density effects, is overcome by the enhancing contribution to the flow provided by the fluid velocity slip at the wall. The latter becomes more important in tight geometries, ultimately being capable of modifying flow dynamics.

The physical mechanisms underlying fluid slippage at walls are not well understood at the nanoscale, where dense and confinement effects add several complexities with respect to the usual rarefied conditions. For example, it is unclear to what extent the Navier-Stokes equations with slip boundary conditions can accurately describe fluid behaviour under molecular confinements. Furthermore, the effects of fluid density and confinement as well as surface properties, such as curvature and microscopic roughness, on velocity slip are still not fully understood. Using a simple fluid-wall framework, it is shown that the interfacial friction coefficient, which is inversely proportional to the slip length, is linear with the peak fluid density at the wall, regardless of the nominal density, confinement ratio, and wall curvature. The peak density turns out to increase as the nominal density increases, with a mild dependence on confinement and curvature. Furthermore, the friction coefficient scales according to the Smoluchowski prefactor with respect to the influence of the accommodation coefficient, similar to the case of a rarefied gas when the same gas-surface dynamics are considered — despite the physics next to the wall are very different.

Altogether, these results represent a significant step forward in understanding the mechanisms of fluid flow in molecular-scale systems and have important implications for the design and optimisation of nanofluidic devices.

Lay Summary

The miniaturisation fever has revolutionised the electronics industry, leading to the manufacturing of smaller and lighter products that make our lives easier when, for instance, we have to carry personal belongings such as mobile phones or less chunky but more powerful laptops. Although less known to the general public, the same principles have been applied to systems that involve the flow of fluids, leading to the development of micro-electro-mechanical systems (MEMS). These have found widespread applications in our day-to-day activities by making devices smaller, more affordable, and highly functional. For example, inkjet printer heads use this technology to accurately dispense tiny droplets of ink, resulting in better resolution when printing. Microfluidic-based accelerometers are used in automotive airbags to detect rapid changes in acceleration for an optimal airbag deployment. Additionally, MEMS-based monitors offer non-invasive and precise monitoring of blood pressure for patients, enabling early detection of hypertension and other cardiovascular diseases.

However, these advancements would not have been possible without a clear understanding of the underpinning physical processes, permitting to build mathematical models that capture the system response. The concept of further scaling down is supported by the remarkable behaviour of biological systems at the tightest of scales. In general, water-based fluids move between cells through molecular-sized conduits, yielding an ultra-efficient filtration of materials without significant, if any, loss of valuable throughput. This ideal performance seems to defy the well known permeability-selectivity trade-off: it is not possible to obtain large quantities of a high-quality product, and, as such, we have not yet been able to replicate these promising results in artificial membranes. However, the results in synthetic structures with nanopores have exceeded the theoretical expectations, providing optimism for further progress in the field. Nature is therefore a constant source of inspiration for engineers and scientists, where understanding the principles of natural phenomena can push the boundaries of innovation and develop breakthrough technologies that benefit society.

Despite all the complexities that exist in real systems, it may be surprising to know that accurate descriptions can often be obtained using elegant approximations. These simplified models, although idealised, have proven to be remarkably useful in many practical applications, as they capture the very essence of the processes at stake. In the case of gases, for example, theoretical models treat the many particles as points that move rapidly and collide very frequently with each other or with the walls of the recipient they occupy. When the gas is rarefied, i.e. at low pressures, the most general

governing equation is the Boltzmann equation, from where expressions can be derived that model the motion of fluids at large scales, such as the flow of air around the wings of an airplane. However, these simplifications do not longer hold up when a fluid is confined at very tight scales, and we have to resort to more elaborate models.

Nevertheless, many insights can be gained by thinking of molecules as marbles, to take account of the fact that they occupy a volume comparable to the space in which they are confined. In addition, interactions with the impermeable walls confining the gas are expected to be more important. In our studies, we define the boundaries of the system in a mathematical way, which allows us to build a robust method for simulating the fluid confinement without including additional complexities that might obscure the analysis. This approach demonstrates the power of abstraction and simplification in science and engineering, allowing us to grasp the fundamental mechanisms of fluid behaviour and apply them to real-world applications. As might be expected, this subtle change (from points to marbles) will have some implications on the basic physics, that are already observed when dealing with the allegedly easier case of a fluid at rest that does not flow.

Let us imagine that there exist sufficiently powerful magnifying glasses that allow to observe the fluid-constituent particles, and that we pick and tag an individual marble with a different colour. One would observe that, despite our eye sees the fluid as quiescent, the tagged particle moves in a rather erratic way when using the loupe, constantly changing its direction after collisions with the other marbles, as a drunk person leaving a pub after having too many pints. These “random walks” are important because they theoretically bridge the small-scale world with the observable one — thanks to Einstein and his doctoral studies. However, the mobility of the marble is affected by the fluid structure when packing, which, at the same time, depends on the degree of confinement. Just imagine how much harder it would be to cross the Royal Mile in Edinburgh if the space available to people was halved due to some construction works on the footways. Rationalising these ideas and building up models that systematically capture the fluid behaviour under tight confinements is one of the aims of this thesis.

The study of fluids in motion, driven by external forces, raises more complicated phenomena that require further research. For instance, it has recently been discovered that some results that were taken for granted no longer hold at the nanoscale, which implies that deeper insights are needed to manipulate fluids in nano-engineering applications. In this thesis, we clarify why this happens by identifying the most important contributions to the fluid flow. In order to do so, we shed light on the intricacies that need to be modelled by treating the fluid as it is, a large number of individual molecules, where the underlying theories and assumptions are solved by computational means.

Acknowledgements

I would like to express my most sincere gratitude to those who have contributed to the successful completion of this PhD thesis, as their unwavering support and encouragement have been invaluable throughout this ride. As I now embark on the next phase of my journey, I carry with me the invaluable lessons and experiences gained during this remarkable task. If life really is a state of mind after all, these people deserve recognition for settling the best atmosphere I could have asked for to thrive. No matter how big or small the part they played was, their insights have been pivotal in refining the ideas contained in these pages.

Foremost, I am deeply indebted to my main supervisor, Livio, whose expertise, mentorship, and honesty have been instrumental in shaping the direction of this research. Your passion, constructive criticism, and dedicated guidance have challenged me to strive for excellence at every step. I just can hope that the work relationship built during my time in Edinburgh remains fruitful in the future. Likewise, I want to thank Matthew for his time and dedication in his role as assistant supervisor. Your work ethic has been inspirational to show up and match the expectations from our very first meeting.

My gratitude extends to my colleagues and fellow researchers, both within and outside the Multiscale Flow X group at the IMT, for engaging discussions and camaraderie. The random chit-chats and collaborative exchanges have immensely enriched my research experience. More importantly, it was great to share coffee breaks, meals, and the occasional pint while going through endless digressions on natural philosophy with all of you. Although I am not a big fan of clichés, you are the main reason why this place felt like *home away from home* to me, and I will forever cherish that. A wee bit of my heart is staying in Scotland for good.

Last but not least, my heartfelt appreciation also goes to my family and lifelong friends for their unconditional love and belief during the challenging periods of this academic pursuit. Your understanding provided the emotional strength needed to overcome obstacles (albeit these are the only true path) and persevere, taking the bull by the horns. You have proved to be the core of my life and, despite my somewhat annoying tendency of living abroad, I am fortunate to have all of you in my inner circle. As so far, my future steps will be dictated by decisions that, I hope, would make you proud. This thesis, which is the culmination of years of hard work and dedication, is as much yours as it is mine.

Declaration

I declare that this thesis has been composed by myself, and that the work contained herein is my own, except where stated otherwise in the text. This work has not been submitted for any other degree or professional qualification, except as specified. The included publications are a result of my own work, and will constitute the materials presented on Chapter 3, Chapter 4, and (tentatively) Chapter 5 of this document where, for the purpose of open access, the author has applied a CC BY public copyright licence to any Author Manuscript version arising from the submission to the corresponding publication journals.

Carlos Corral-Casas, 29th May 2023

Contents

Abstract	ii
Lay Summary	iv
Acknowledgements	vi
Declaration	vii
Figures and Tables	x
1 Introduction	1
1.1 Nanofluidics. Tiny Devices for Huge Ideas	1
1.2 Diffusion. Standing on Fick’s and Einstein’s Shoulders	4
1.2.1 What Happens at the Nanoscale?	6
1.3 Flow Transport. Hydrodynamic Governing Equations	7
1.3.1 Boundary Conditions and the Velocity Jump	9
1.3.2 What Happens at the Nanoscale?	10
1.4 Thesis Outline	12
2 Theoretical and Computational Background	13
2.1 The Fluid of Hard Spheres. A Game of Marbles	13
2.2 Kinetic Theory. The Boltzmann Equation	16
2.2.1 Knudsen Number. Flow Regimes Classification	19
2.3 Dense Fluids. The Enskog Equation	21
2.4 Stochastic Walls. Maxwell Scattering Kernel	23
2.5 Event-Driven Molecular Dynamics	25
3 Self-Diffusion of Confined Fluids	29
3.1 Literature Survey	29
3.2 Methodology	33
3.2.1 Problem Formulation	33
3.2.2 Simulation Setup	35
3.3 Results and Discussion	36
3.3.1 Fickian and Einstein Self-diffusivities	36
3.3.2 Splitting Fluid-Fluid and Fluid-Wall Collisions	40
3.3.3 A Semi-Analytical Model for Self-diffusivity	41

CONTENTS	ix
3.3.4 Scaling of Self-Diffusivities with Confinement	46
3.3.5 Effect of TMAC on Self-Diffusivities	47
3.4 Conclusions	49
4 On the Knudsen Minimum Disappearance	50
4.1 Literature Survey	50
4.2 Methodology	52
4.2.1 Simulation Setup and Problem Formulation	52
4.2.2 Flow Analytical Solutions. Hagen-Poiseuille Equations.	53
4.3 Results and Discussion	54
4.3.1 Knudsen Minimum Vanishing. Diffusion-Based Analysis	54
4.3.2 Knudsen Minimum Vanishing. Slip-Based Analysis	56
4.4 Conclusions	62
5 Fluid Velocity Slip at the Nanoscale	63
5.1 Literature Survey	63
5.2 Methodology	66
5.2.1 Theory for the Slip Boundary Conditions	66
5.2.2 Fluid and Geometry Characterisation	69
5.2.3 Simulation Setup	70
5.3 Results and Discussion	71
5.3.1 Numerical Evaluation of the Friction Coefficient	71
5.3.2 Quantitative Criterion for the Validity of the Slip Solutions	73
5.3.3 Rationalisation of the Interfacial Friction Coefficient Results	74
5.4 Molecular Dynamics Simulations	79
5.5 Conclusions	80
6 Concluding Remarks	83
6.1 Executive Summary	83
6.2 Future Work	84
6.2.1 Additional Studies with the Existing Modelling Approach	84
6.2.2 Extensions to Different Fluid and Wall Systems	86
Appendices	
A Maxwell Scattering Kernel in Cylindrical Geometry	88
B Computation of the Collision Time with Cylindrical Walls	91
C Friction Coefficient from Equilibrium EDMD Simulations	93
Bibliography	96

Figures and Tables

Figures

1.1	Resemblance in how density oscillations arise due to geometric constraints in monatomic fluids, both in the (a) bulk, where the only dependence is on density, and in (b) confined systems at the nanoscale. Note the inaccessible regions ($n = 0$) next to each wall, of $\sigma/2$ width, comprising a larger relative portion of R for smaller channels.	3
1.2	(a) Characteristic bell-shaped curves of diffusing particles, from following independent random walks. Molecules are initially located at the origin, with their distribution flattening as t goes on. (b) Depiction of Brownian motion for three molecules in the two-dimesional space, from the experiments of Perrin (Philibert, 2005).	6
1.3	Different analytical predictions based on the BCs choice: stick (red curve), real slip (blue curve), and apparent slip (green curve). The latter must be used to retrieve the actual velocity field (empty circles) in the Navier-Stokes framework.	11
2.1	Similarities in the shielding effect that occurs in the bulk and in the region adjacent to the wall. The more prominent excluded volume effects next to the walls cause particles to be <i>pushed</i> towards them, with the total force being represented by the big red arrow. Therefore, the fluid preferentially orders next to the boundary, depleting the central region of the channel. . .	15
2.2	EDMD simulations can be used to explore the whole range of fluid densities and confinements. However, this map shows the most computationally efficient technique for modelling the hard-sphere fluid ($\sigma = 0.4$ nm, $T = 298$ K) in each region, where the boundaries (i.e. solid lines for different λ and Kn) are based on major approximations.	16
2.3	Classification of flow regimes based on the Knudsen number. For small λ/L ratios, the Boltzmann equation leads to the exact balance equations of hydrodynamic fields. When rarefaction strikes, numerical approaches are needed for general solutions.	20

3.1	Two independent methods for computing the self-diffusivity of confined fluids: (a) Einstein relation, by measuring the average molecular MSD, and (b) Fick's law by changing the colour tag of particles (type A: red, type B: mustard) as these cross the boundaries, followed by computing the steady-state tagged transport flux.	33
3.2	Self-diffusivities computed using the Einstein relation (filled circles) and as a proportionality factor according to Fick's law (empty squares). Comparisons for accuracy in the large R limit are made with results from Heyes et al. (2007), represented by solid horizontal lines. Inset: fluid layering in confined channels, deviating from the homogeneity of bulk fluids defined by $n/n_0 = 1$	38
3.3	Self-diffusivities from EDMD simulations for various confinement ratios as they vary with: (a) Knudsen number and (b) reduced density. Dashed lines in (a) show data at equal packing fractions, where gas is considered as dense for $\eta \gtrsim 0.01$ and dilute otherwise. The solid line in (b) represents the theoretical prediction for the molecular self-diffusivity.	39
3.4	Fluid-fluid, fluid-wall, and total collision frequencies with respect to Knudsen number for $R = 2$ (green) and $R = 100$ (blue).	40
3.5	Ratio between fluid-fluid and total (fluid-fluid and fluid-wall) collision frequencies with respect to Kn	42
3.6	Comparison between self-diffusivities from EDMD simulations (solid circles) and Bosanquet predictions, equation (3.11) (solid lines). Dashed lines represent the molecular self-diffusivity approximation from equation (3.8), whereas dash-dotted lines show the Knudsen self-diffusivity from equation (3.10). Inset: ratio of predicted self-diffusion values over EDMD results. Same colour scheme for symbols is used as that in figure 3.3.	43
3.7	Scaling of all self-diffusivities by their R value, as a function of Kn for fully diffuse walls. The solid line at $Kn \geq 10$ is the free molecular approximation. Inset: non-linearity of molecular self-diffusivities in the continuum-based regimes (Erpenbeck & Wood, 1991).	46
3.8	Self-diffusivities as a function of the wall microscopic roughness, in tight ($R = 5$, squares) and quasi-bulk ($R = 100$, circles) channels. Coloured solid lines represent the Bosanquet predictions, defining D_k as in equation (3.13).	47

4.1	(a) Comparison between the dimensionless MFR provided by non-equilibrium simulations (symbols) and the theoretical predictions assuming Fickian diffusion, as given by equation (4.11) (lines). There is good agreement in the free molecular regime ($Kn \geq 10$), whilst Fick's law underestimates MFR elsewhere, which implies that convective transport terms cannot be neglected at any confinement. The normalising factor of the mass flow rate \dot{m}_n is presented in equation (4.10). (b) Dependence of the self-diffusivity D on the Knudsen number Kn and the confinement ratio R . Horizontal lines represent the theoretical value of the Knudsen self-diffusivity from equation (4.12) for each R	55
4.2	(a) Qualitative analysis of the dimensionless MFR curves against the Knudsen number. In sufficiently <i>large</i> channels (orange colour), where the continuum transport is larger than the free molecular one, the MFR curve develops two stationary points. In tighter confinements (blue colour), where the free molecular flow is larger than the continuum one, the MFR curve could either show the two stationary points or follow a monotonic increase instead, where the Knudsen minimum disappears. (b) Relative percentage error of the MFR predicted by the Navier-Stokes equations with slip, for different confinement ratios. Dashed horizontal lines are the average percentage error over the displayed range of Kn : the mean error is within 8% for the tighter $R = 5$, whereas it reduces to less than 4% for the largest $R = 50$ considered here. The inset shows the slip coefficients determined from EDMD simulations, for different R and η values, obtained by fitting the quadratic velocity profiles.	57
4.3	(a) Partial rates of change against the reduced specific volume, for $R = 20$, under the continuum framework of fluid modelling, which capture how flow transport is affected by a change of each of the underlying contributions. (b) Interplay between the continuum (dash-dotted) and the slip (dotted) contributions for different R . For sufficiently large R values, the continuum contribution dominates and the sum of all rates of change (solid) cross the x -axis, i.e. the Knudsen maximum appears. However, for tight channels, the continuum contribution is less relevant whereas slip remains the same, driving the overall rate of change to be positive throughout the entire range of ν values, with the Knudsen maximum disappearing as a consequence.	59
4.4	Graphical abstract showing the main findings of this piece of work.	62

5.1	Depiction of a planar channel with nominal height H and characteristic length $L = H - \sigma$, with typical density (left) and velocity (right) profiles. The density profile shows the fluid structuring close to the walls, with the first dip marking the boundary of the Δ -layer. As highlighted in the inset, three different velocity slips can be defined: the mean velocity in the Δ -layer, assuming that the density there is constant ($u_{s,\Delta}$), the apparent velocity at the boundary, which gives the Navier-Stokes velocity profile in the fluid bulk ($u_{s,app}$), or the real fluid velocity at the boundary ($u_{s,real}$).	66
5.2	Range of validity of the slip solution for both planar and cylindrical geometries, for fully diffuse walls ($\alpha = 1$). The solid symbols represent flow conditions for which the slip solution provides an accurate representation of the flow, while the empty symbols indicate flow conditions for which it does not, i.e. the linear stress-strain relationship no longer holds. The dashed lines represents the fluid conditions corresponding to $Kn = 0.1$	74
5.3	Friction coefficient versus the fluid peak density for the confinement ratios and nominal densities, corresponding to the solid symbols in figure 5.2 in cylindrical (red solid circles) and planar (blue solid squares) channels. The dashed black line represents the best linear fit of the results, and the solid black line represents the kinetic prediction for rarefied gases, equation (5.18). The inset zooms in this regime at the bottom left-hand side. Walls are fully diffuse ($\alpha = 1$).	75
5.4	Comparison of peak density at the wall and nominal reduced density for different confinement ratios, with insets showing the effect of fluid layering on bulk density reduction, i.e. depletion, at different levels of confinement. Walls are fully diffuse ($\alpha = 1$). The same colour scheme as in figure 5.2 was used for the confinement.	77
5.5	Friction coefficient versus the accommodation coefficient of the wall. As in the fully diffuse case, results do not depend on the channel geometry for partial TMAC (planar geometries are represented with empty symbols as a guide to the eye). Coloured dashed lines represent the Smoluchowski scaling for the black dashed line.	78
5.6	Friction coefficient versus fluid peak density for MD, in the same range of confinement ratios and nominal densities to those of the EDMD simulations. The solid line corresponds to the best linear fit of the MD results, whereas the dashed line represents the EDMD fit with the TMAC value from MD simulations (i.e., $\alpha = 0.49$).	80

5.7	Summary of the main results. When a fluid of nominal density η_0 is confined in a channel of confinement ratio R , oscillations in the density profile form in the region adjacent to the walls. The corresponding peak density η_p is a proxy for the collision frequency of the fluid molecules with the walls. The collision frequency, together with the accommodation coefficient, determines the amount of tangential momentum transferred from the fluid to the wall, which is ultimately related to the friction coefficient.	81
A.1	Decomposition of the circular-based radial (red) and tangential (blue) velocity components into their linear homologues.	89
B.1	Calculation of the collision point of a particle i , based on its velocity, with a cylindrical wall.	92
C.1	The correlation functions are normalised with respect to their maximum absolute value. (a) Example of the two correlation functions, showing that decorrelation occurs for short times. (b) Numerical Laplace transformation of the force-velocity correlation function, together with the best fit of the memory function.	94

Tables

3.1	Self-diffusivities for fluids at different confinements for $\eta = 5 \times 10^{-4}$. The Fickian (D^F) and Einstein (D^E) results are in very good agreement when $\ell_y \gtrsim 2\lambda$, expressed by bold rows	37
3.2	Self-diffusivities for fluids at different confinements for $\eta = 5 \times 10^{-3}$. Again, the two methodologies are in very good agreement when $\ell_y \gtrsim 2\lambda$	37
5.1	Planar channels. Comparison of interfacial friction coefficients $\xi_{0,\Delta}$ for nominal reduced densities η_0 and confinement ratios R of interest, using non-equilibrium (left column) and equilibrium (right column) approaches. Walls are fully diffuse ($\alpha = 1$).	72
5.2	Cylindrical channels. Comparison of interfacial friction coefficients $\xi_{0,\Delta}$ for nominal reduced densities η_0 and confinement ratios R of interest, using non-equilibrium (left column) and equilibrium (right column) approaches. Walls are fully diffuse ($\alpha = 1$).	73
5.3	Interatomic Lennard-Jones potential parameters ($\sigma_{LJ}, \epsilon_{LJ}$) used in the MD simulations. Molecular masses m [u]: Ar = 39.948, Pt = 195.084.	79

Introduction

This chapter provides a brief introduction to the challenges of describing simple fluids confined at the molecular scale ([Section 1.1](#)). In particular, the topics of self-diffusion and pressure-driven flows are explored. While the continuum-based Fick's laws ([Section 1.2](#)) and Navier-Stokes equations ([Section 1.3](#)) have proved effective at the macroscopic scale, they fail to capture the complex molecular interactions and confinement effects that characterise these transport mechanisms at the nanoscale. This emphasises the importance of moving from the traditional continuum approach to a molecular perspective, which will be discussed in the next chapter.

1.1 Nanofluidics. Tiny Devices for Huge Ideas

In the second half of the twentieth century, significant advances were made in the understanding of the dynamics of gas flows in small channels. This progress motivated the development of a new discipline, known as microfluidics, that reached its pinnacle with the large-scale production of micro-electro-mechanical systems (MEMS). These are devices with flow characteristic lengths L of less than 1 mm but greater than 1 μm ; that is, a size range of about four orders of magnitude smaller than the traditional hand-made artefacts but, at the same time, about four orders of magnitude larger than the size of the smallest atomic species. The flow characteristic length is the dimension that characterises the length scale of a physical system, which is typically the smallest one as the gradients of the macroscopic quantities along this direction are usually the most pronounced. MEMS have found applications in many fields ([Gad-el Hak, 1999](#)), including micro-heat exchangers that optimise the cooling of electronic circuits, micro-pumps for controlled drug delivery, or accelerometers for airbags in cars, to name a few. In general, the “active principle” of these small-scale devices is to decrease viscous shear in the bulk of the fluid, which minimises energy dissipation, and/or to induce flow-enhancing phenomena such as velocity slip — increasing the MEMS throughput and, therefore, its performance. However, shrinking the channel size can make the flow hydrodynamic resistance larger, producing the opposite effect to that desired, and so this is a challenging issue that requires careful consideration.

As it is known to occur in the field of electronics, one may wonder whether the efficiency of fluidic operations also improves by decreasing the flow characteristic length scale. Following the *savoir-faire* that has been obtained in the now mature field of microfluidics, nanofluidics has recently emerged as a discipline in its own right (Eijkel & van den Berg, 2005; Sparreboom et al., 2010). This term refers to the study of fluids confined at even smaller scales, spanning from the molecular order of magnitude (few Å) to around 0.1 µm. Fluids confined at the nanoscale are ubiquitous in nature, and a deeper understanding of their behaviour can have far-reaching consequences in many fields, increasing the potential for impactful advances. For instance, in biological systems, it is known that water-based liquids permeate across aquaporin structures of few Å (Murata et al., 2000), yielding an outstanding permeability-selectivity performance that has not been replicated yet in artificial membranes. Another example is the presence of light hydrocarbons within sedimentary strata, where fluids are trapped due to the extremely high pressures and nanometric size of rock pores. Despite these unfavourable conditions, the shale gas flow still exceeds the theoretical predictions coming from the long-standing correlations used in petroleum engineering (Zhang et al., 2019). Therefore, the extension of the study of fluids within smaller and smaller scales is an attractive goal, which draws great attention in terms of the breakthrough applications that would be harnessed from reverse engineering such natural phenomena (Bocquet, 2020).

As a matter of fact, experimental studies with novel materials like carbon nanotubes (Holt et al., 2006), boron nitride nanotubes (Siria et al., 2013), or graphene-based sheets (Joshi et al., 2014) have generated considerable optimism in the field of nanofluidic transport. These materials have demonstrated remarkable capabilities, including unexpectedly large mass flow rates, immense osmotic energy conversion, and enhanced filtration results. These are just some examples of membranes with nanopores that might see applications in social questions of great interest, such as seawater desalination. However, to turn these practical applications into tangible commercial realities, it is essential to develop accurate mathematical models that capture the underpinning physical mechanisms. The theoretical understanding is a challenging task since, for fluids within nanoscale geometries, a representative fraction of the fluid molecules is in constant interaction with the confining walls. An in-depth knowledge of both the fluid-fluid and fluid-wall relationships is needed to accurately control and manipulate fluids at these scales, which can be almost intractable from a modelling standpoint. This is the reason why, in order to shed light on the problem, models that approximate the fluid and wall behaviour are needed. These simplified representations of the system under study are usually solved numerically with computers; simulations can be quickly designed in comparison to actual experiments, allow to overcome the issues associated with the measurements of minute flow rates through single tubes (Secchi et al., 2016), and provide flexibility to carry out enlightening studies along the relevant scales.

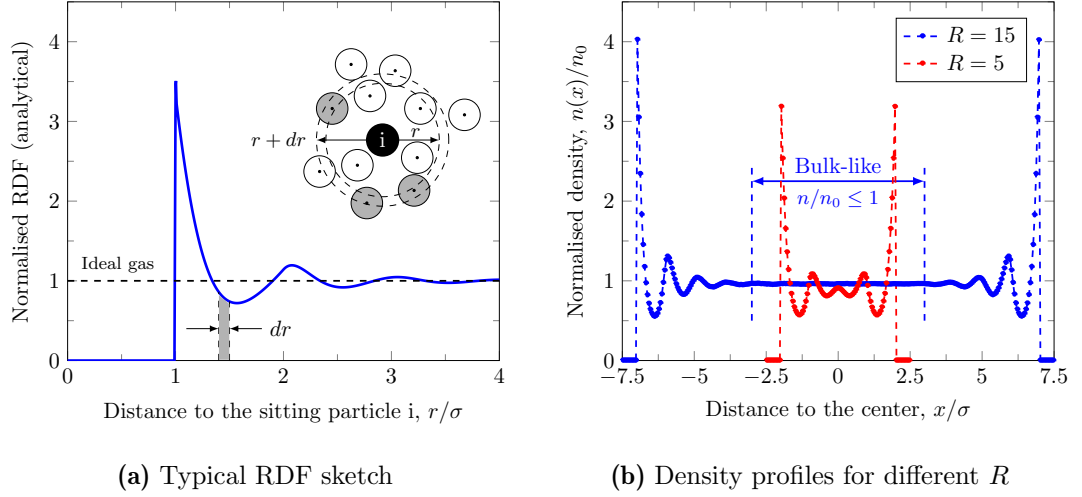


Figure 1.1: Resemblance in how density oscillations arise due to geometric constraints in monatomic fluids, both in the (a) bulk, where the only dependence is on density, and in (b) confined systems at the nanoscale. Note the inaccessible regions ($n = 0$) next to each wall, of $\sigma/2$ width, comprising a larger relative portion of R for smaller channels.

Regarding the wall modelling, it is worth noting that the boundaries will simply act as a space impenetrable to the fluid molecules. This is because the length scales associated with the oscillations induced by surfaces might reach up to several tens of nanometers (Kavokine et al., 2021), where quantum effects play no role and do not have to be modelled. When a fluid comes in contact with a solid interface, it experiences preferential layering adjacent to the surface due to excluded volume effects and the interactions between the fluid and the wall (Israelachvili, 2011). Its occurrence is, in principle, no different to the ordering that occurs in the bulk (Hansen, 2022), which is quantified through its radial distribution function (RDF), see Figure 1.1a. This property measures the probability density of finding a particle at a given distance r from a fixed particle position i , and shows the fundamental differences associated with how molecules are distributed in the different states of matter. This is depicted in Figure 1.1, where the analogies between the two different layering phenomena can be easily observed.

A convenient way of defining nanochannels is through their dimensionless confinement ratio $R = L/\sigma$, as the quotient between the flow characteristic length and the diameter of fluid particles σ . In unconfined geometries (large R values), the impact of the molecular ordering adjacent to the boundary on the flow outcome is relatively insignificant as the bulk behaviour, characterised by fluid-fluid interactions, prevails. On the other hand, it may be predominant in nanofluidic systems because of their larger surface-to-volume ratio. This is represented in Figure 1.1b, where the fluid behaviour for the same nominal density and different confinement ratios is shown. For $R = 5$ (red curve), the density oscillations extend even to the furthest region with respect to the walls (the middle of

the channel at $x = 0$), oppositely to “larger” cases such as $R = 15$ (represented by the blue curve), where a homogeneous region shows up in the region between $x \approx -3$ and $x \approx 3$. This structuring leads to unique phenomena that, at least locally, differ from the predictions of the classical fluid modelling based on continuum considerations. As such, gaps in knowledge are identified even at the most fundamental level of understanding.

1.2 Diffusion. Standing on Fick’s and Einstein’s Shoulders

In nanofluidic systems, where interactions with the boundaries play a non-negligible role, diffusive transport is anticipated to be important. This is the case, for example, with materials that have a network of interconnected nanopores spanning a wide range of connections, as in porous media. In fact, the permeability for these systems has to be predicted based on diffusive phenomena, rather than using the classical approaches valid for larger scales (Falk et al., 2015; Obliger et al., 2018). In essence, diffusion processes are the macroscopic manifestation of the tendency of a system to approach homogeneity, arising from microscopic collisions that cause the vanishing of gradients related to fluid properties, e.g. concentration. This can be easily illustrated by a drop of dye spreading within a glass of pure water, where there is no preferential direction of motion (no macroscopic flow) induced by a thermodynamic gradient, and yet over time a coloured liquid is produced. In the simpler case of a single-component quiescent fluid, the mobility of single “tagged” particles in a pool of otherwise identical molecules is also subjected to a special kind of diffusion, known as self-diffusion.

The classical modelling approach to diffusive processes in bulk fluids is based on the phenomenological Fick’s laws (Fick, 1855), from which the diffusion equation, that describes the evolution of the system according to diffusive processes with time t , can be derived, i.e.

$$\frac{\partial C(\mathbf{r}, t)}{\partial t} = D \nabla^2 C(\mathbf{r}, t). \quad (1.1)$$

Here, $C(\mathbf{r}, t)$ is the concentration of tagged particles (in the pool of tagged and untagged molecules), \mathbf{r} is the spatial location of the diffusing material, and D is the self-diffusion coefficient, also known as self-diffusivity. The partial differential equation in Eq. (1.1) is derived from the principle of mass conservation, $\partial C / \partial t + \nabla \cdot \mathbf{j} = 0$, where the constitutive relation is known as the Fick’s first law

$$\mathbf{j}(\mathbf{r}, t) = -D \nabla C(\mathbf{r}, t), \quad (1.2)$$

that links the flux of diffusing material $\mathbf{j}(\mathbf{r}, t)$ with its driving force, i.e. the concentration gradient of tagged molecules. The negative sign is included to denote that particles move from high to low concentration regions.

The Fick’s description was devoted to complete the first systematic study of diffusion. It was carried out by the Scottish chemist Thomas Graham circa 1830, but without a mathematical relation that captured the experimental results (Graham, 1833). The basis of this treatment is the continuum hypothesis, which assumes that it is possible to describe the fluid on a much coarser scale of resolution than the molecular scale, as if the fluid was an entity that completely filled the space it occupies. This implies that is possible to define the local properties of the fluid as averages over continuous elements, which are large compared with the molecular structure of the fluid but small enough in comparison with the scale of macroscopic phenomena (Gad-el Hak, 1999). Fick had the intuition that diffusion could be described by the same mathematical formalism as heat conduction (initially proposed by Fourier in 1822), and concluded that the constant of proportionality, as in the case of the thermal conductivity, was “*dependent upon the nature of substances*”. It is a testament to Fick’s model of diffusion that all of the subsequent developments have in no way undermined the validity of his conclusions. However, it contains the self-diffusion coefficient, that can only be determined through experimentation or theoretically, based on a molecular description of the fluid.

The link between the continuum-like Fick’s laws and a first-principles theoretical basis was first provided by Albert Einstein. Besides his PhD thesis (from his 1905 *annus mirabilis*), he published several seminal papers (Einstein, 1956) on the topic. The starting point was “*a closer consideration of the irregular movements which arise from thermal molecular movement*”, from where he studied how far a molecule travels in the x -dimension (for ease of understanding, although the conclusions do not change when generalising the study to the three-dimensional actual motion of molecules) in a given amount of time. Molecules would move throughout the bulk according to random walk dynamics, initially discovered by the Scottish botanist Robert Brown (Brown, 1828). Assuming that all particles move independently, let $p(x, t)$ be the probability density function for a particle to be around location x at time t . After making some probabilistic assumptions, it is possible to retrieve the same functional form of Eq. (1.1), $\partial p / \partial t = D \partial^2 p / \partial x^2$. For the initial condition at time $t = 0$, it is assumed that the N independent particles start from the origin $x = 0$, mathematically corresponding to a Dirac delta function. The partial differential equation is then solved to give

$$p(x, t) = \frac{N}{\sqrt{4\pi Dt}} e^{-\frac{x^2}{4Dt}}, \quad (1.3)$$

that is, a probability density function of Gaussian nature with a sharp bell-shape at initial times (corresponding to the peak in the Dirac delta function), and that flattens down with time until reaching a more uniform distribution — achieved at long times after particles have spread following diffusive mechanisms, see Figure 1.2a.

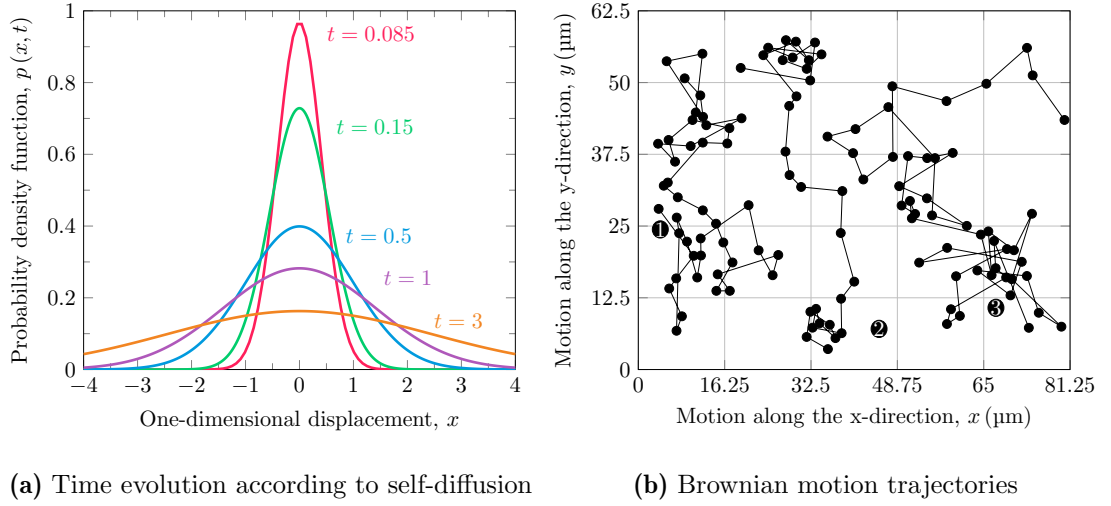


Figure 1.2: (a) Characteristic bell-shaped curves of diffusing particles, from following independent random walks. Molecules are initially located at the origin, with their distribution flattening as t goes on. (b) Depiction of Brownian motion for three molecules in the two-dimensions space, from the experiments of Perrin (Philibert, 2005).

This closed-form mathematical expression allows for an analytical determination of how far a particle goes, on average, in a given time. If one computes the first moment, the probability vanishes unexpectedly, as a particle following Brownian motion is equally likely to move to the left as it is to move to the right. On the other hand, the second moment produces

$$\langle x^2(t) \rangle = \frac{1}{\sqrt{4\pi Dt}} \int dx x^2 e^{-\frac{x^2}{4Dt}} = 2Dt, \quad (1.4)$$

the famous Einstein relation that links the self-diffusion coefficient, i.e. macroscopic behaviour of a system, with the mean squared displacement (MSD) of particles $\langle x^2(t) \rangle$, i.e. its underlying microscopic dynamics. Therefore, the self-diffusion process is based on the random molecular motion, that is graphically conceptualised for a two-dimensional system in Figure 1.2b. If considering an n -dimensional space, the relationship between the MSD and the self-diffusion coefficient is trivially generalised to $\langle \mathbf{r}^2(t) \rangle = 2nDt$.

1.2.1 What Happens at the Nanoscale?

Despite self-diffusion constitutes the simplest possible transport mechanism, the elemental physics are still not fully understood in the context of molecularly confined fluids. The Fickian approach clearly cannot be applied under extremely tight confinements, where molecules move without being able to overtake each other, abiding to their original order in the row. This anomalous transport process is known as single-file diffusion (Hahn & Kärger, 1998), characterised by a slowing down of the diffusive dynamics where the relationship between the MSD and the self-diffusivity is no longer linear as in Eq. (1.4).

For “larger” but still moderately confined channels, with $R \sim O(10)$, the Fick's first law is assumed to be valid but there are doubts about the proportionality factor to be used in its formulation. Specifically, particles travel through regions with different local densities, e.g. see [Figure 1.1b](#), which will affect the random walk dynamics and, accordingly, the squared displacements of molecules. Thus, it is not clear whether the Einstein relation breaks down in this condition, let alone how the self-diffusion coefficient is affected by confinement. The novel study of these issues is presented in [Chapter 3](#) of this thesis, where we propose a semi-analytical model that allows to evaluate the transition between the different diffusive mechanisms occurring for different fluid and wall conditions.

1.3 Flow Transport. Hydrodynamic Governing Equations

The classical modelling approach for fluids in motion relies on the hydrodynamic theories, which describe the fluid as a continuum in analogy to the Fick's laws. The axioms of fluid dynamics in the classical mechanics framework ([Leal, 2007](#)) are the mass conservation and the balances for linear momenta, i.e. Newton's second law of motion, and energy, i.e. first law of thermodynamics

$$\frac{\partial \rho}{\partial t} + \nabla \cdot (\rho \mathbf{v}) = 0, \quad (1.5)$$

$$\frac{\partial}{\partial t} (\rho \mathbf{v}) + \nabla \cdot (\rho \mathbf{v} \mathbf{v} - \boldsymbol{\sigma}) = \mathbf{F}, \quad (1.6)$$

$$\frac{\partial}{\partial t} (\rho E) + \nabla \cdot (\rho E \mathbf{v} - \boldsymbol{\sigma} \mathbf{v} + \mathbf{q}) = \mathbf{F} \cdot \mathbf{v}, \quad (1.7)$$

where ρ is the mass density, \mathbf{v} is the macroscopic flow velocity, \mathbf{F} are the external forces acting on the control volume (e.g. gravitational and other external forces), $\boldsymbol{\sigma}$ is the stress tensor, E represents the total energy acting on the system (including the internal and kinetic terms), and \mathbf{q} denotes the heat flux vector. The stress tensor consists of the normal components (P for pressure) and the deviatoric term $\boldsymbol{\tau}$, so that $\boldsymbol{\sigma} = -P\mathbf{I} + \boldsymbol{\tau}$, \mathbf{I} being the unit tensor. The equations of motion are therefore obtained by considering the balance of forces experienced by the infinitesimal element of bodies.

The general balances presented in [Eq. \(1.5\)](#) – [Eq. \(1.7\)](#) remain incomplete since the stress and heat flux terms are unknown, and information based on the fluid microscopic behaviour is needed to close this approach. The missing piece of the puzzle is provided by empirical constitutive relations, where the theoretical predictions are compared with experimental measurements to ascertain their validity. For an isotropic fluid that obeys Newtonian laws, the deviatoric stress tensor $\boldsymbol{\tau}$ is a linear function of the velocity gradient (strain rate)

$$\boldsymbol{\tau} = \mu \left[\nabla \mathbf{v} + (\nabla \mathbf{v})^T \right] + \zeta (\nabla \cdot \mathbf{v}) \mathbf{I}, \quad (1.8)$$

where μ is the (shear) first coefficient of viscosity and ζ is the (bulk) second coefficient of viscosity. For monatomic gases, the two viscosity coefficients are related by the so-called Stokes hypothesis, $\zeta + 2/3\mu = 0$. This implies that the fluid is in quasi-thermodynamic equilibrium, characterised by a very large amount of collisions between fluid molecules. An important fact is that Newtonian fluids are also generally found to follow Fourier's law of heat conduction in its isotropic form (Leal, 2007), and so this would serve as the closure for the heat flux. By assuming the less general case of an isothermal fluid in which the shear viscosity is constant (μ does not depend on the pressure), the Navier-Stokes equations for the viscous transport of linear momentum in a non-relativistic system, where mass is conserved, read

$$\rho \left(\frac{\partial \mathbf{v}}{\partial t} + \mathbf{v} \cdot \nabla \mathbf{v} \right) = \mathbf{F} - \nabla P + \mu \nabla^2 \mathbf{v} + \frac{1}{3} \mu \nabla (\nabla \cdot \mathbf{v}), \quad (1.9)$$

which were independently obtained by Navier (Navier, 1823) and Stokes (Stokes, 1845). In addition to the constitutive relations, an equation of state relating the different thermodynamic properties (temperature, pressure) is required as well — otherwise, the final system of equations would be under-determined. Eventually, a system composed of five coupled equations (one for mass, three for momentum, one for energy) and the equation of state is built, involving six unknowns, namely ρ , P , T and \mathbf{v} . The formidable challenge posed by the non-linearity of the convective term $\mathbf{v} \cdot \nabla \mathbf{v}$ implies that analytical solutions are very difficult to obtain. Therefore, the Navier-Stokes equations are tackled numerically in computational fluid dynamics (CFD) solvers, where the governing expressions are solved using discretisation techniques.

The Navier-Stokes equations can be used to analytically describe the fluid behaviour in a channel, where certain simplifications can be applied to the full expression presented in Eq. (1.9). The comprehensive experimental studies of fluid flows within capillary vessels performed by Poiseuille (Sutera, 1993) granted that pressure-driven flows in conduits are broadly named after him nowadays. In the steady state, under the assumption of low speeds, as is the case for nanofluidic systems, the time-derivative and the convective terms vanish. The fluid can be considered as incompressible in these conditions, for which the continuity equation simplifies to $\nabla \cdot \mathbf{v} = 0$, yielding the following equation of motion for horizontal flows (no gravity effects, and so $\mathbf{F} = 0$)

$$\mu \nabla^2 \mathbf{v} = \nabla P. \quad (1.10)$$

The solution of Eq. (1.10) with the appropriate boundary conditions produces the so-called Poiseuille and Hagen-Poiseuille equations for planar and cylindrical geometries, respectively. These expressions describe the quadratic velocity profile, characterising pressure-driven flows, in the streamwise direction.

1.3.1 Boundary Conditions and the Velocity Jump

The hydrodynamic differential equations require a certain number of boundary conditions (BCs) to produce closed-form mathematical expressions that allow the study of flow problems. The governing equation, Eq. (1.10), involves a second-order derivative of the velocity, and so two velocity BCs are required to yield the velocity profile. Firstly, the normal velocity component at the fluid-solid interface simply states that a fluid cannot penetrate an impermeable wall, $\mathbf{v} \cdot \tilde{\mathbf{n}}|_{r_w} = 0$, where $\tilde{\mathbf{n}}$ is the unit vector normal to the wall and r_w is the hydrodynamic wall position that defines the accessible space for the fluid. Secondly, the tangential velocity component provides information about how the streamwise momentum is exchanged between the fluid and the wall.

Based on empirical considerations, it was initially assumed that the fluid layer next to the wall moves with the same velocity as the surface (Stokes, 1846) and that, if slip existed, it was too small to make any observable difference on the macroscopic scale. Seminal experiments from Poiseuille, Darcy, and Helmholtz hinted that the velocity of a fluid adjacent to a solid wall was not necessarily the same of the surface. However, it was not clear whether the very small values could be considered different from the non-slip condition, owing to the limitations of the experimental apparatus and measurement techniques. In the case of Poiseuille flows, where the walls are static, this involves the definition of the stick boundary condition $\mathbf{v} \cdot \tilde{\mathbf{t}}|_{r_w} = 0$, where $\tilde{\mathbf{t}}$ is the tangential unit vector parallel to the wall in the flow direction.

The idea behind this ad-hoc Dirichlet boundary condition is that within the fluid there cannot be any finite discontinuity of velocity, as this would involve infinite velocity gradients. This would result in infinite viscous stresses that destroy the finite relative motion of particles close to each other. Theoretically, the stick boundary condition is strictly true if the fluid undergoes an infinite number of collisions with the wall. In other words, the wall information is entirely transmitted near the boundary, where the adjacent fluid adopts the wall velocity without affecting the behaviour in the central (bulk) region of the channel. This is represented by the red line in Figure 1.3, where the Navier-Stokes equations are solved with the stick boundary condition to predict a null velocity of the fluid layer immediately next to the wall. Beyond this limit, the fluid-wall collision frequency is not high enough for the fluid to adopt the wall velocity, and a certain degree of tangential velocity slip has to be allowed.

This was pointed out by Navier in his groundbreaking studies on the laws of fluids in motion (Navier, 1823), where he proposed that the tangential fluid velocity follows a linear Neumann boundary condition with the strain rate

$$\xi_0 (\mathbf{v} \cdot \tilde{\mathbf{t}})_{r_w} + \mu \frac{\partial (\mathbf{v} \cdot \tilde{\mathbf{t}})}{\partial (\mathbf{r} \cdot \tilde{\mathbf{n}})} \bigg|_{r_w} = 0, \quad (1.11)$$

where the hydrodynamic wall position is not necessarily the same as the actual wall (Hansen, 2022). Throughout his derivation, Navier acknowledged that the shear viscosity μ represents the resistance resulting from the sliding of any two fluid layers on top of each other, and that the interfacial friction coefficient ξ_0 represents the resistance per unit area resulting from the sliding of the fluid layer in contact with the wall. Thus, two different coefficients of friction, i.e. μ for fluid-fluid and ξ_0 for fluid-wall, are needed to ascertain the behaviour of the fluid adjacent to the boundary. With the advent of microfluidics and the improvements of experimental techniques (Neto et al., 2005), more accurate measurements are now available that definitely confirm the need to account for partial slip BCs, where slip-modified parabolic velocity profiles can even be observed directly in experimentation (Fratantonio et al., 2020).

By construction, the role of the boundary condition is to simply shift the velocity profile by the magnitude of the velocity slip value. The flow prediction that results from using Eq. (1.11) to solve the Navier-Stokes equations is identical to the actual velocity far away from the boundaries, where the quasi-local equilibrium condition holds, see green line in Figure 1.3. In contraposition with the bulk region of the fluid, the region next to the wall is said to be in local non-equilibrium because there are not enough intermolecular collisions. Therefore, the hydrodynamic treatment does not allow to retrieve the true velocity field next to the wall (Hadjiconstantinou, 2006) — that can be only captured by accounting for the molecular structure of the fluid, as the Stokes hypothesis underpinning Eq. (1.9) breaks down.

Following this approach, the correct Navier-Stokes solution for the velocity field predicts an apparent velocity at the plane of the wall, $v_{\text{slip}}^{\text{NS}}$, that does not correspond to its actual value. If the BCs were instead implemented as the true velocity slip, see blue curve in Figure 1.3, the hydrodynamic equations would not capture the flow dynamics in the bulk. Nevertheless, the width of the non-equilibrium region (known as Knudsen layer in the kinetic theory of rarefied gases, see Chapter 2) is very small compared to the flow characteristic length and, therefore, the discrepancy associated with the poor predictive capability of the green curve next to the boundaries will not affect the accuracy of the continuum-based analysis, as the bulk dynamics still prevail.

1.3.2 What Happens at the Nanoscale?

The classical approach to fluid dynamics modelling was developed to explain the behaviour of fluids on a macroscopic scale, and the question is to what extent it can be applied to fluids confined in a molecular scale. The rule of thumb is that the continuum hypothesis surprisingly remains valid for confinements as tight as $R \sim 3$, which is sustained by results coming from experiments and computational simulations (Bocquet

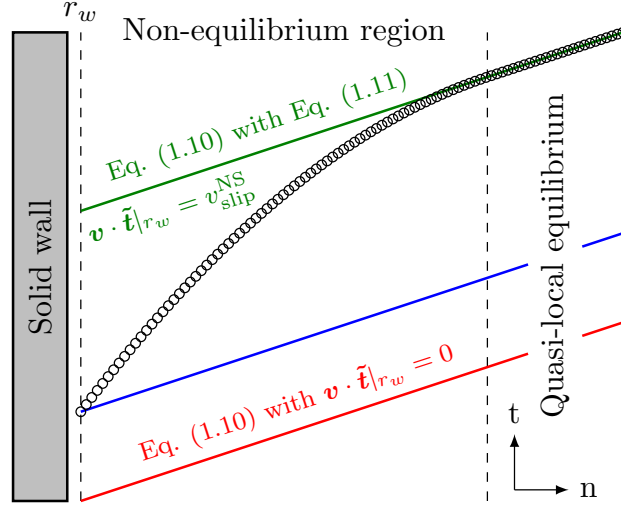


Figure 1.3: Different analytical predictions based on the BCs choice: stick (red curve), real slip (blue curve), and apparent slip (green curve). The latter must be used to retrieve the actual velocity field (empty circles) in the Navier-Stokes framework.

& Charlaix, 2010). On the other hand, the departure with respect to the quasi-local thermodynamic equilibrium, because of a reduced number of intermolecular collisions, will more frequently restrict the use of hydrodynamics — with the need to account for the fluid molecular nature to capture its true physics.

One example of the surprising results found at molecular-like confinements is illustrated by the study of Poiseuille mass flow rates in straight channels. At the microscale, a stationary point in the form of a minimum is observed at intermediate densities (Cercignani & Daneri, 1963; Pollard & Present, 1948). However, at the nanoscale, when the confinement ratio further decreases, the minimum disappears and the mass flow rate monotonically increases with decreasing density (L. Wu et al., 2016). While molecular-based approaches hold promise in capturing the physics of fluids, it is still not known why this happens. This novel study of these issues is presented in Chapter 4 of this thesis, where, for the first time, an analytical treatment of the underlying flow mechanisms (diffusion, viscous convection, velocity slip) justifies the vanishing phenomenon.

The key to explain the Knudsen minimum disappearance will be the more predominant role of the velocity slip at the wall. At the nanoscale, the influence of density and confinement effects is more involved than in classical rarefied conditions, and so the conventional assumptions are invalidated. The intricacies of the velocity jump phenomena are subjected to further studies in Chapter 5. This probe serves as a stepping stone for a better understand of the velocity slip at the nanoscale, and contributes to the development of predictive hydrodynamic models for nanofluidic scenarios.

1.4 Thesis Outline

The remaining chapters of this thesis read:

Chapter 2 – Theoretical and Computational Background gives an overview of fluid modelling based on its molecular structure, treating the constituent particles as hard spheres, which is required to provide a more complete description of the fluid and flow behaviour. First, the statistical methodology is presented, epitomised by the Boltzmann and Enskog equations. Second, a comprehensive review of the deterministic procedure that captures the exact time evolution of the hard-sphere system, event-driven molecular dynamics (EDMD), is included.

Chapter 3 – Self-Diffusion of Confined Fluids is the first chapter that presents new results. The contribution to the current knowledge is on some uncertain aspects of the self-diffusion process for confined fluids. First, the validity of the Einstein relation within tight geometries is proved by comparing the MSD-based results with explicit Fick's law calculations. Second, the crossover between diffusive mechanisms in different regimes is analysed systematically using appropriate theoretical means.

Chapter 4 – On the Knudsen Minimum Disappearance is the second chapter that presents new findings. The contribution to the current knowledge is on the explanation of a recently discovered confined flow phenomenon that does not happen at larger scales. First, we conclude that diffusion on its own cannot be used to rationalise the transport phenomena in confined straight channels, in contrast to what occurs in porous media. Second, using an analytical approach based on the hydrodynamic principles, we show that the mass flow rate behaviour is justified by the more notorious contribution of velocity slip in smaller channels.

Chapter 5 – Fluid Velocity Slip at the Nanoscale is the final chapter that presents original research. The contribution to the current knowledge is on shedding light on the contradictory results that have been reported for the velocity jump in pressure-driven flows. First, we study the range of validity of the Navier-Stokes equations with slip boundary conditions, to clarify whether the criterion established for rarefied gases also applies to dense fluids. Second, we perform a comprehensive numerical investigation on how the velocity slip depends on several properties, such as fluid nominal density, confinement ratio, channel geometry and wall microscopic roughness.

Chapter 6 – Concluding Remarks provides a summary of the main findings and discusses several possibilities for continuing the work started with this thesis, in the form of research directions that might be of interest for investigation in the future.

Theoretical and Computational Background

This chapter provides a brief overview of the mathematical models and simulation tools that can be used for the molecular description of fluids at the nanoscale. In all cases, the fluid is considered to be composed of hard spheres, which means that long-range interactions are assumed to be negligible compared to the short-range ones (Section 2.1). It is important to note that different models can be used depending on the density of the fluid. For extremely dilute conditions, the Boltzmann equation can be used (Section 2.2). At moderate densities, the Enskog equation must be used because of the need to account for spatial correlations between molecules (Section 2.3). In the kinetic theory framework, the wall is modelled as a mathematical surface that conveniently modifies the fluid distribution around it, using the so-called scattering kernels (Section 2.4). Finally, at high densities, a more fundamental approach is required, based on molecular dynamics simulations that follow the motion of individual fluid particles (Section 2.5).

2.1 The Fluid of Hard Spheres. A Game of Marbles

Even though the hard-sphere model is a highly simplified representation of real systems, it is a powerful and useful tool for theoretical and computational studies of simple fluids (Dyre, 2016). This is because some of the key properties of fluids are mainly determined by the excluded volume effect, i.e. molecules are prevented from occupying the same physical space due to their size and shape. In real systems, this effect occurs because of the overlap of electron orbitals, which produces a extremely strong repulsion between atoms when being at very close distances. To mimic this behaviour in a tractable fluid model, impenetrable hard spheres with no rotational degree of freedom solely interact with an infinite mutual repulsion whenever a collision takes place, which is mathematically expressed by a pairwise potential of the form

$$\Phi_{\text{HS}}(\mathbf{r}_i, \mathbf{r}_j) = \begin{cases} \infty, & r_{ij} \leq \sigma, \\ 0, & r_{ij} > \sigma, \end{cases} \quad (2.1)$$

where $r_{ij} = \|\mathbf{r}_i - \mathbf{r}_j\|$ is the Euclidean distance between the pair of interacting particles i and j . Thus, the model of hard spheres is a good representation of the behaviour of extremely dilute, where long-range interactions are relatively small, and/or liquid-like systems, where short-range interactions dominate. The most important variable in a fluid of monatomic hard spheres is the dimensionless packing fraction η (also referred to as reduced density), representing the number of fluid particles in the theoretical volume occupied by one sphere of diameter σ , $\eta = n\pi\sigma^3/6$. Its equation of state is accurately predicted by the Carnahan-Starling compressibility factor Z (Carnahan & Starling, 1969)

$$Z = \frac{1 + \eta + \eta^2 - \eta^3}{(1 - \eta)^3}. \quad (2.2)$$

The hard-sphere fluid model allows to capture one of the key properties in nanofluidics, in particular the one that underlies the departure with respect to the continuum-like behaviour of the fluid (Kavokine et al., 2021). Namely, Eq. (2.1) permits to capture the preferential fluid structuring, see Figure 1.1b, because it is mainly determined by the dominant repulsive interactions at short-range. Next to the wall, particles pack very close to each other in a problem where the main constraint is of geometric nature. It is hypothesised that this fluctuating density profile arises because a portion of the surface of the spherical particle close to the boundary is shielded from collision, and so it feels a pushing force towards the wall (Cutchis et al., 1977; Frezzotti, 1997).

A rough sketch of this mechanism is attached in Figure 2.1, which shows how, when two particles approach each other, there is a portion of the spherical surface protected from collisions — building up an effective attraction between them. This is depicted by the red shield in front of each molecule. A similar rationale applies when a particle approaches a different element in the system, such as the confining wall. This behaviour resembles the adsorption process, where fluid molecules behave as if they *stick* to the wall, although the underpinning physics must necessarily be different. Adsorptive phenomena would only be possible if there are attractive Van der Waals forces¹, not modelled by Eq. (2.1), between the fluid and wall particles. A more elaborate model that can, for instance, model adsorption is defined by the Lennard-Jones potential (Allen & Tildesley, 2017), which, in similarity to the hard-sphere potential, predicts strong repulsions at short distances. However, there is a mild attraction between atoms at intermediate r_{ij} , which continuously dies out with distance until it becomes negligible. Some insights about the implications of using the Lennard-Jones model are given in Chapter 6, where possible extensions of the work presented in this thesis are critically discussed.

1. In general, the Van der Waals potential describes the intermolecular forces, of both repulsive and attractive nature, that describe interactions for particles separated by a distance larger than σ , i.e. not undergoing a collision. These must exist in reality to form the liquid and solid states of matter.

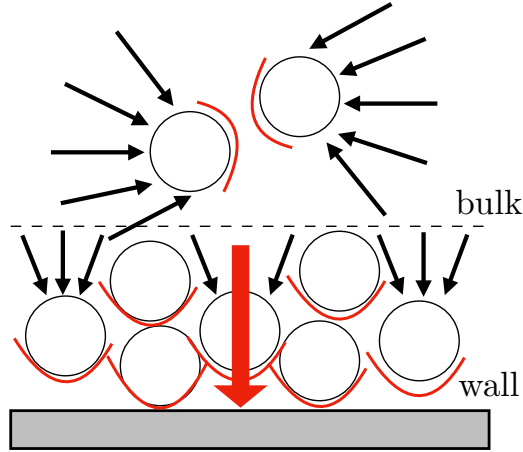


Figure 2.1: Similarities in the shielding effect that occurs in the bulk and in the region adjacent to the wall. The more prominent excluded volume effects next to the walls cause particles to be *pushed* towards them, with the total force being represented by the big red arrow. Therefore, the fluid preferentially orders next to the boundary, depleting the central region of the channel.

To sum up, the fluid of hard spheres encapsulates a rich structural and thermodynamic behaviour, while keeping a certain degree of simplicity that permits to obtain perspectives impossible to infer otherwise (Kjellander & Sarman, 1991; Wertheim, 1963). Since the repulsive forces are modelled by the step function, i.e. it is a discontinuous potential, and attractive forces are not accounted for in Eq. (2.1), the hard-sphere fluid is unique in the sense that it is a single-phase fluid, where the only energy available to the particles is kinetic. Therefore, the results obtained for a fluid of hard spheres can be compared directly with those coming from standard kinetic equations. Specifically, it presents gas-phase behaviour at low densities and liquid-phase behaviour at moderate-to-high densities, before crystallising into a solid-like state at very high densities. Moreover, it may serve as a foundation for the so-called perturbation theories that accurately treat more realistic systems (Barker & Henderson, 1967). For all these reasons, and considering the scope of our research, the use of a fluid of hard spheres is fully justified.

In our investigations, this fluid model is examined over a wide range of fluid reduced densities and confinement ratios, in which different methodologies can be used to study its behaviour. These procedures mainly obey two classifications: continuum-based, as those described in Chapter 1, or molecular-based, which can be statistical or deterministic. The effective limits of these major approximations are presented in Figure 2.2. The different molecular approaches (based on the kinetic theory, where the governing analytical equations are nonetheless solved numerically most of the times owing to its detailed microscopic description, or event-driven molecular dynamics) will be discussed in the following sections of this chapter.

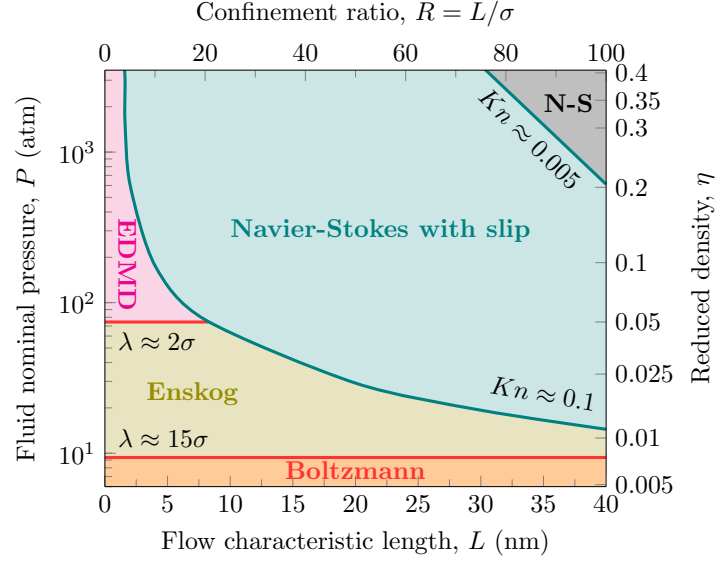


Figure 2.2: EDMD simulations can be used to explore the whole range of fluid densities and confinements. However, this map shows the most computationally efficient technique for modelling the hard-sphere fluid ($\sigma = 0.4$ nm, $T = 298$ K) in each region, where the boundaries (i.e. solid lines for different λ and Kn) are based on major approximations.

2.2 Kinetic Theory. The Boltzmann Equation

The continuum-based description of fluid flows is justified when collisions between molecules play a dominant role, and so molecular information is homogeneously distributed throughout the fluid (Struchtrup, 2005). In this condition, the gas approaches the quasi-local thermodynamic equilibrium state in a short time compared to the characteristic time scale of the system, from where the phenomenological stress-strain, Eq. (1.8), and heat flux constitutive relations turn out to be valid. Therefore, the fluid flow can be captured by the Navier-Stokes equations, see Section 1.3. However, the hydrodynamic modelling breaks down in physical situations of very different nature, ranging from the predominant fluid-structure interactions in micro and nano-electro-mechanical systems to the re-entry of spacecrafts in upper planetary atmospheres. In the former, the flow characteristic length is very small due to the device dimension, whereas gas rarefaction effects occur at low pressures in the latter. In all these cases, the common factor is that there are not enough intermolecular collisions to bring the gas to a quasi-local equilibrium state and, therefore, a kinetic theory description of gas flows is required.

The kinetic theory considers the gas composed by a large number of molecules that rapidly move in straight lines in the absence of external body forces, whose trajectories are briefly interrupted when colliding with each other or with the walls of the recipient where they are contained (Kremer, 2010). The Scottish physicist James Clerk Maxwell

was the first one to postulate (Maxwell, 1860) that the gas should be statistically described by means of a distribution function $f(\mathbf{r}, \mathbf{u}, t)$ over the microscopic state of particles, which is defined as the probability to find, at a certain time t , a molecule within the elementary volume defined by $[\mathbf{r}, \mathbf{r} + d\mathbf{r}]$ and $[\mathbf{u}, \mathbf{u} + d\mathbf{u}]$, i.e. around the position $\mathbf{r} = (x, y, z)$ with a molecular velocity close to $\mathbf{u} = (u_x, u_y, u_z)$. The distribution function evolves in space and time according to a non-linear integro-differential kinetic equation which typically takes the form of a balance equation in the six-dimensional phase space — comprising the three spatial and velocity dimensions. It was initially postulated by Boltzmann, assuming that binary collisions are the only encounter between particles presenting uncorrelated velocities (the molecular chaos assumption), and thus was named eponymously after his work (Boltzmann, 1872)

$$\frac{\partial f}{\partial t} + \underbrace{\mathbf{u} \cdot \frac{\partial f}{\partial \mathbf{r}} + \mathbf{F}_a \cdot \frac{\partial f}{\partial \mathbf{u}}}_{\text{streaming}} = \underbrace{Q_B(f, f)}_{\text{collision}}, \quad (2.3)$$

being the central equation of the kinetic theory of rarefied gases. The left-hand side in Eq. (2.3) is analogous to the material derivative in the Navier-Stokes equations, Eq. (1.9), but here the molecular velocity is also an independent variable. Essentially, it describes the evolution of the distribution function with time as the particles move in space according to their molecular velocities and, if so, as they are accelerated due to an external body force exerted per unit mass of molecules \mathbf{F}_a , e.g. gravity. The right-hand side, which is referred to as collision integral, is a source/sink term which takes into account molecular interactions. For a fluid of hard spheres it reads

$$Q_B(f, f) = \int \int \mathbf{g} \cdot \tilde{\mathbf{k}} [f'_1(\mathbf{r}, \mathbf{u}'_1, t) f'(\mathbf{r}, \mathbf{u}', t) - f_1(\mathbf{r}, \mathbf{u}_1, t) f(\mathbf{r}, \mathbf{u}, t)] d^2\tilde{\mathbf{k}} d\mathbf{u}_1, \quad (2.4)$$

where $\mathbf{g} = \mathbf{u} - \mathbf{u}_1$ denotes the relative velocity between the two colliding particles, and $\tilde{\mathbf{k}}$ is the unit apsidal vector that assigns the relative position of two molecules at the time of their impact. The collision integral calculates the effect of collisions on the distribution of particles with velocity \mathbf{u}' , studying possible interactions with particles having all other velocities \mathbf{u}'_1 . The first term within brackets is the source term, referring to the particles that had a velocity around \mathbf{u}' and, after an interaction with other particle, obtain a different velocity \mathbf{u} following hard-sphere dynamics, that is $\mathbf{u}' = \mathbf{u} + \mathbf{g} \cdot \tilde{\mathbf{k}}$ and $\mathbf{u}'_1 = \mathbf{u}_1 - \mathbf{g} \cdot \tilde{\mathbf{k}}$ for the two molecules undergoing a collision. The second term within brackets is the sink term, referring to the particles that, after an encounter, obtain a post-collisional velocity around \mathbf{u} . Given the inherent complexity of Eq. (2.4), the collision integral can be simplified by means of the so-called kinetic models (Sharipov & Seleznev, 1998), so that an exact method of solution can be applied to these approximate equations that maintain the fundamental properties of the full form.

Another seminal contribution coming from Boltzmann is the so-called \mathcal{H} –Theorem, where the \mathcal{H} function is always a non-increasing function of time ($d\mathcal{H}/dt \leq 0$)

$$\mathcal{H} = \int f \log f d\mathbf{u}, \quad (2.5)$$

which would remain constant ($d\mathcal{H}/dt = 0$) if and only if the distribution function f is of the original form proposed by Maxwell (Maxwell, 1867)

$$f^M(\mathbf{r}, \mathbf{u}, t) = n(\mathbf{r}, t) \left(\frac{m}{2\pi kT} \right)^{3/2} e^{-\frac{m(\mathbf{u} - \mathbf{v})^2}{2kT}}, \quad (2.6)$$

where $n(\mathbf{r}, t)$ denotes the local number density, m the molecular mass, k the Boltzmann constant, and T the temperature of the system. Since there is a quantity that decreases, namely \mathcal{H} , any non-equilibrium distribution function would evolve monotonically towards a Maxwellian due to intermolecular collisions. In other words, the \mathcal{H} –theorem proves that the collision integral in Eq. (2.4) vanishes when the distribution function is evaluated as f^M , whence the gas is said to be in thermodynamic equilibrium. The Maxwellian distribution can be considered as a basic natural law, as it stipulates the most probable velocity distribution of a monatomic single-species gas in the equilibrium state, which can be proved through experimentation using molecular beam techniques (Shen, 2005).

Macroscopic fields, such as number density, flow velocity, temperature, and so forth, are velocity-weighted moments of the distribution function (Kremer, 2010)

$$n = \int f(\mathbf{r}, \mathbf{u}, t) d\mathbf{u}, \quad (2.7)$$

$$n\mathbf{v} = \int f(\mathbf{r}, \mathbf{u}, t) \mathbf{u} d\mathbf{u}, \quad (2.8)$$

$$nT = \frac{m}{3k} \int f(\mathbf{r}, \mathbf{u}, t) (\mathbf{u} - \mathbf{v})^2 d\mathbf{u}. \quad (2.9)$$

The scalar pressure can be obtained by evaluating the normal stress elements from which, in combination with the temperature, the equation of state for the rarefied gas ($P = nkT$) can be retrieved. It is hence evident that, starting from Eq. (2.3), one could determine the distribution function and eventually the observable information (e.g. thermodynamic properties, transport coefficients) of rarefied gases by integrating over the microscopic velocity, although this represents a formidable task in itself. Indeed, before the advent of computers, there were instances in which thousands of random collisions were computed by hand (Thomson, 1901) to obtain further insights. Of course, Lord Kelvin did not perform this task himself. Eventually, it took almost 40 years to first obtain approximate analytical solutions of the Boltzmann equation, from an expansion of a parameter inversely proportional to the gas density (Hilbert, 1912).

2.2.1 Knudsen Number. Flow Regimes Classification

Since the Boltzmann equation is defined in a high-dimensional phase space, it is more convenient to use rational methods that allow to derive transport equations for the macroscopic quantities. An important concept in kinetic theory is the mean free path λ , which represents the average distance travelled by particles between two consecutive collisions. For a fluid of hard spheres (Bird, 1994), given the unambiguous definition of its molecular diameter, there is a closed-form mathematical expression in the form of

$$\lambda = \frac{1}{\sqrt{2}n\sigma^2}, \quad (2.10)$$

which shows its reciprocal relationship with the gas density. The ratio between the mean free path and the characteristic length of the channel is an important dimensionless group known as the Knudsen number $Kn = \lambda/L$. As already hinted in Chapter 1, the characteristic length scale is usually identified with the channel size that bounds the fluid under study in internal flows. The reciprocal Knudsen number turns out to weight the collision integral on the right hand side of the Boltzmann equation in its dimensionless form, with respect to the streaming term due to the motion of molecules on the left hand side. Despite Eq. (2.3) provides an accurate description of rarefied gas flows over the entire range of Kn , it is also true that analytical solutions are either very difficult to obtain or have not been attained yet, and numerical solutions are expensive when compared to hydrodynamic-based CFD solvers, that model the fluid without a detailed microscopic description. Therefore, the importance of introducing the Knudsen number stems from the fact that it helps to classify the gas flow into distinct regimes, see Figure 2.3, where different approximation methodologies for obtaining solutions apply.

In the continuum limit when the Knudsen number goes to zero, it is possible to prove, by using the so-called Chapman-Enskog expansion (Chapman & Cowling, 1952), that the Boltzmann equation simplifies to the Navier-Stokes equations with stick BCs. However, even in this limit, the kinetic theory description is richer than the hydrodynamic one in that it also provides an explicit expression for the transport coefficients, viscosity and heat conductivity, in terms of the particle interatomic potential of choice. For slightly rarefied gas flows, where the Knudsen number is no longer zero but is still small ($Kn \lesssim 0.1$), asymptotic expansions of the Boltzmann equation have shown that the constitutive relations underpinning the continuum approach are still valid (Sone, 2007), but accurate results are only obtained if modifying the boundary conditions that complement the governing equations. Therefore, the no-slip boundary conditions must be changed so that the gas is allowed to slip along the confining surface, see Section 1.3.1, and so this range of Kn is known as slip regime. All non-equilibrium effects occur in a very thin region next to the wall (Shen, 2005), which is known as the Knudsen layer,

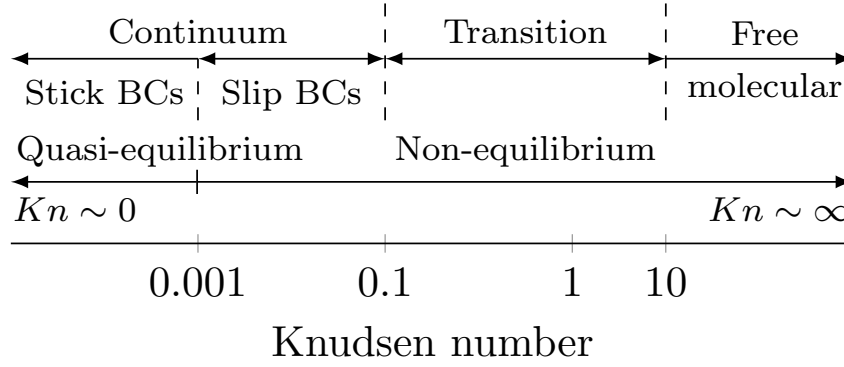


Figure 2.3: Classification of flow regimes based on the Knudsen number. For small λ/L ratios, the Boltzmann equation leads to the exact balance equations of hydrodynamic fields. When rarefaction strikes, numerical approaches are needed for general solutions.

whose width is on the order of magnitude of λ . It is here where Maxwell introduced the rather bold assumption of no intermolecular collisions, i.e. the impinging gas stream towards the wall is of the same character as in the bulk of the gas. A treatment based on the framework of liquids, where the analysis relies on the interfacial friction coefficient, is also possible (Kennard, 1938), although less common.

For moderate Knudsen numbers, in the early transition regime ($Kn \lesssim 1$), continuum-like models can still be analytically derived from kinetic equations, albeit a larger set of variables and/or higher derivatives are needed in comparison to the classical Navier-Stokes equations (Gu & Emerson, 2009; Struchtrup, 2005). The highly rarefied behaviour is found in the free molecular regime, for $Kn > 10$, where particles undergo ballistic motion following collisionless flights between interactions with confining walls. It is just in this regime, in the limit where $Kn \sim \infty$, when analytical solutions of the Boltzmann equation are always achievable given that the collision integral is nought. However, in order to describe gas flows in a wider range of Knudsen numbers, kinetic equations have to be solved numerically. The numerical solution of kinetic equations for realistic flows is a challenging task for, at least, two reasons. The first one is that the distribution function, which is the unknown, depends on seven variables — three for position, three for velocity, and time; the second reason is that the collision integral is very complicated.

Numerical methods for solving the Boltzmann equation can be roughly divided into three groups. Regular and semi-regular methods are similar in that the distribution function is discretised on a grid in the phase space, and the streaming term is approximated by using finite difference, finite element or finite volume methods. These procedures differ in the way the collision integral is evaluated: regular methodologies, such as the discrete velocity method (Broadwell, 1964; Valougeorgis & Naris, 2003) or based on

Galerkin methods (Ghioldi & Gibelli, 2014) amongst many others, adopt deterministic integration schemes, while semi-regular ones adopt Monte Carlo or quasi Monte Carlo quadratures (Frezzotti & Sgarra, 1993; Nordsieck & Hicks, 1967). On the other hand, particle-based methods, such as Direct Simulation Monte Carlo (DSMC), are the most widely used choice because of their computational efficiency. The basic idea (Bird, 1994) is to represent f by a number of sample particles which move in the computational domain and collide according to stochastic rules derived from the kinetic equation. Macroscopic fields are then obtained by time averaging particle properties.

2.3 Dense Fluids. The Enskog Equation

For the Boltzmann equation to hold, the mean free path of gas molecules has to be much larger than the molecular size, and so the collision integral is localised as if particles were point-like. The heuristic generalisation of kinetic theory principles beyond the dilute gas idealisation, for $\lambda \sim \sigma$, was first developed by Enskog (1922), considering a dense gas whose molecules repel one another like hard, smooth, perfectly elastic spheres. The main difference with respect to the Boltzmann molecular chaos assumption is that molecules are correlated in space, so that the collision integral reads (Kremer, 2010)

$$Q_E(f, f) = \sigma^2 \int \int \mathbf{g} \cdot \tilde{\mathbf{k}} \{ \chi^{\text{HS}} [\mathbf{r}, \mathbf{r} + \sigma \tilde{\mathbf{k}} | n] f'_1(\mathbf{r} + \sigma \tilde{\mathbf{k}}, \mathbf{u}'_1, t) f'(\mathbf{r}, \mathbf{u}', t) - \chi^{\text{HS}} [\mathbf{r}, \mathbf{r} - \sigma \tilde{\mathbf{k}} | n] f_1(\mathbf{r} - \sigma \tilde{\mathbf{k}}, \mathbf{u}_1, t) f(\mathbf{r}, \mathbf{u}, t) \} d^2 \tilde{\mathbf{k}} d\mathbf{u}_1, \quad (2.11)$$

where the pre-collisional velocities $(\mathbf{u}', \mathbf{u}'_1)$ are transformed into the post-collisional ones $(\mathbf{u}, \mathbf{u}_1)$ through elastic hard-sphere scattering dynamics, and χ^{HS} is the two-point pair correlation function of a hard-sphere fluid, that gives the probability to find molecules at positions \mathbf{r} and \mathbf{r}_1 in a density field $n(\mathbf{r}, t)$ in equilibrium. Besides extending the kinetic theory principles to evaluate systems of arbitrary density, the Enskog equation is also required to study the behaviour of molecularly confined fluids. This is because $L \sim \sigma$, from where excluded volume effects, underpinning the ordering near the walls, need to be considered for an accurate flow description. In general, these cannot be captured with kinetic equations developed for dilute gases, although some derivations based on the Boltzmann equation have been proposed to study confined systems (Brey et al., 2016). These agree with results obtained from more general statistical mechanics approaches (Schmidt & Löwen, 1997), but are restricted to further constraints ($L \approx 2\sigma$).

In this phenomenological theory, the assumption of binary collisions still holds, but now they occur at a distance of one molecular diameter σ , namely one particle (with velocity \mathbf{u}') is at point \mathbf{r} and the other one (with velocity \mathbf{u}'_1) is at point $\mathbf{r} \mp \sigma \tilde{\mathbf{k}}$ when a collision occurs. The \mp sign is introduced so that it refers to interactions that take $(\mathbf{u}, \mathbf{u}_1)$ or

$(\mathbf{u}', \mathbf{u}'_1)$ as initial velocities, respectively. Likewise, due to the excluded volume effects, there is an increase in the collision frequency characterised by χ^{HS} , which adopts a value of unity for the rarefied gas and increases with the gas density n . In the standard Enskog theory framework, χ^{HS} is set equal to the equilibrium pair correlation function χ taken at the midpoint of the line joining the centres of colliding atoms. Where the Enskog equation is used in the present thesis (see [Chapter 5](#)), the actual value of the density at the contact point is replaced with the value of the density field averaged over a spherical volume of diameter σ , using the Fischer-Methfessel prescription ([Fischer & Methfessel, 1980](#)). Thus, χ^{HS} becomes a functional of the local density

$$\chi^{\text{HS}}[\mathbf{r}, \mathbf{r} \pm \sigma \tilde{\mathbf{k}} | n] = \chi \left[\bar{n} \left(\mathbf{r} \pm \frac{1}{2} \sigma \tilde{\mathbf{k}}, t \right) \right], \quad (2.12)$$

where χ is given by the equation of state of the hard-sphere fluid proposed by [Carnahan and Starling \(1969\)](#), and

$$\bar{n}(\mathbf{r}, t) = \frac{3}{4\pi\sigma^3} \int_{\mathbb{R}^3} n(\mathbf{r}_1, t) w(\mathbf{r}, \mathbf{r}_1) d\mathbf{r}_1, \quad (2.13)$$

$$w(\mathbf{r}, \mathbf{r}_1) = \begin{cases} 1, & \|\mathbf{r}_1 - \mathbf{r}\| \leq \sigma, \\ 0, & \|\mathbf{r}_1 - \mathbf{r}\| > \sigma. \end{cases} \quad (2.14)$$

As in the rarefied gas case, macroscopic quantities are obtained as velocity moments of the distribution function. The non-locality of collisions implies that the transfer of momentum and energy owing to intermolecular interactions cannot be neglected anymore, and hence the equation of state now would read $P = nkTZ$, where the extra term Z captures the deviations with respect to the rarefied gas behaviour, see [Eq. \(2.2\)](#).

In the limit for small Knudsen numbers, the application of the Chapman-Enskog method for getting analytical solutions of the Enskog equation suggests that the Navier-Stokes equations are still valid ([Chapman & Cowling, 1952](#)) for describing the flow behaviour in the bulk of the fluid. However, large discrepancies from the hydrodynamic behaviour are expected in the vicinity of solid boundaries, where non-equilibrium effects take place that will, unsurprisingly, affect transport phenomena and its modelling ([Travis et al., 1997](#)). Given the complex interplay of mechanisms at these scales, the departure with respect to the classical modelling is very difficult to rationalise, which shows in the lack of analytical insights. For instance, the functional form of the slip relation cannot be analytically computed through asymptotic expansions of the Enskog equation, as in the rarefied gas framework, but strong empirical evidence suggests that the same procedure holds. That is, modifying the boundary conditions that complement the Navier-Stokes equations to allow for some tangential velocity of the fluid adjacent to the boundary, in the form of a velocity jump between the fluid and the wall ([Shu et al., 2017](#)).

In analogy to the rarefied gas scenario, high-order hydrodynamic-like models can be developed to extend the analytical treatment to the early transition regime (de Haro & Garzó, 1993; Kremer & Rosa, 1988), where the fluid still behaves as a continuum but is not in quasi-equilibrium. Finally, in the free molecular regime, analytical solutions of the collisionless Enskog equation are feasible, although these will be different to the Boltzmann results in a trivial way owing to the non-locality of collisions of particles with the walls. Nevertheless, as for when the Boltzmann equation governs the gas dynamics, numerical solutions are once again required for a general description of the dense gas behaviour. Following the same rationale presented in Section 2.2.1, particle-based methods, such as the DSMC extension proposed by Frezzotti (1997), are usually preferred for simplified problems. In this algorithm, momentum and energy are conserved in every collision and not just in a statistical sense (Montanero & Santos, 1996). Modifications with the classical DSMC occur in the collision algorithm due to the non-local structure of Q_E , where, in general, collisions involve the closest neighbour cells.

2.4 Stochastic Walls. Maxwell Scattering Kernel

So far, the different descriptions of the gas behaviour have only taken into account interactions between its constituent particles, but no terms in Eq. (2.4) or Eq. (2.11) have been introduced to address collisions with the boundaries of the system. Therefore, unless the distribution function of the velocities next to the wall is defined, the full description of the gas behaviour will be clearly incomplete. Despite some attempts have been made to superimpose gas-surface interactions in the collision integral of kinetic equations (Aoki et al., 2022; Frezzotti & Gibelli, 2008), it is true that their accuracy requires further research, and so the most common approach involves the use of empirically-derived kinetic boundary conditions, in the form of the so-called scattering kernels. By construction, scattering kernels neglect the precise microscopic structure of the boundary, and simply allow to relate the incident (f^i) and reflected (f^r) fluxes of molecules for each possible incident velocity on a surface of interest, in the form of a probability density function (Kremer, 2010)

$$f^r(\mathbf{u}) = - \int_{\mathbf{u}' \cdot \tilde{\mathbf{n}} < 0} \frac{\mathbf{u}' \cdot \tilde{\mathbf{n}}}{\mathbf{u} \cdot \tilde{\mathbf{n}}} S(\mathbf{u}' \rightarrow \mathbf{u}) f^i(\mathbf{u}') d\mathbf{u}', \quad \mathbf{u} \cdot \tilde{\mathbf{n}} > 0, \quad (2.15)$$

where $\tilde{\mathbf{n}}$ denotes the unit vector normal to the wall pointing towards the half-space occupied by the fluid and $S(\mathbf{u}' \rightarrow \mathbf{u})$ is the scattering kernel representing the probability that an impinging molecule with velocity \mathbf{u}' is scattered, at the same exact point, with a velocity \mathbf{u} after colliding with the wall. The scattering kernel must satisfy the basic properties of normalisation (i.e. the surface of the wall is impermeable and gas molecules re-emerge after collision), positiveness and reciprocity (Kuřcher, 1971).

The first attempt to express “the conditions which must be satisfied by a gas in contact with a solid planar wall” was carried out by [Maxwell \(1879\)](#). Given its simplicity and that it serves for the purpose of our work (low-speed flows over engineering surfaces), it will be the boundary condition used throughout this thesis. Without further delving in its physical identification (that is, the differentiation between rough and smooth walls), the Maxwell scattering kernel assumes that a fraction of the incident gas molecules is diffusely thermalised to the wall temperature T_w , namely molecules can be scattered to any direction in the half-space occupied by the fluid with a uniform distribution regardless of their impinging velocities

$$S_D(\mathbf{u}' \rightarrow \mathbf{u}) = \frac{1}{2\pi} \mathbf{u} \cdot \tilde{\mathbf{n}} \left(\frac{m}{kT_w} \right)^2 e^{-\frac{m\mathbf{u}^2}{2kT_w}}, \quad (2.16)$$

whereas the remaining partition is specularly reflected, where the normal component of the velocity changes its sign but the impinging momentum is conserved

$$S_S(\mathbf{u}' \rightarrow \mathbf{u}) = \delta[\mathbf{u}' - \mathbf{u} + 2(\mathbf{u} \cdot \tilde{\mathbf{n}}) \tilde{\mathbf{n}}], \quad (2.17)$$

where δ is the Dirac delta function. The partition related with diffuse reflections is called the tangential momentum accommodation coefficient α , also known as TMAC for short, and so the Maxwell scattering kernel reads

$$S_M(\mathbf{u}' \rightarrow \mathbf{u}) = \alpha S_D(\mathbf{u}' \rightarrow \mathbf{u}) + (1 - \alpha) S_S(\mathbf{u}' \rightarrow \mathbf{u}). \quad (2.18)$$

The computational implementation of the Maxwell scattering kernel in a tube accounting for appropriate geometric arguments is described in [Appendix A](#), as well as some other technicalities.

Besides the Maxwell scattering kernel, which is the most used one in the literature by far, some other descriptions of molecular distributions have been proposed as well ([Cao et al., 2009](#)). Examples of different scattering kernels are attributed to Epstein, whose distribution function for reflected molecules takes into account the velocities of the incident particles ([Epstein, 1967](#)), and Cercignani & Lampis, which reproduces the lobular pattern characteristic of molecular beam experiments ([Lord, 1991](#)). It is important to note that the use of stochastic walls is not just limited to the case of solving kinetic equations — but also when dealing with more direct simulation methods, instead of explicitly addressing fluid-wall interactions based on the interatomic potential of choice. Nonetheless, fully understanding the dynamics of gas-surface interactions is a very complicated task. The detailed investigation of this problem requires the involvement of expensive molecular dynamics simulations ([Y. Chen et al., 2022](#)), as well as results obtained from experimental setups ([Arkilic et al., 2001](#); [Ewart et al., 2007](#)).

2.5 Event-Driven Molecular Dynamics

The Enskog equation presented in [Section 2.3](#) has been found to be accurate up to relatively large fluid densities ([Frezzotti, 1999](#)), until correlated collision sequences come into play and the molecular chaos assumption no longer holds. Up to date, there are not accurate first-principles theories that account for higher density effects ([Janssen, 2018](#)), and most of the analytical work in the field is driven by practical applications using empirical correlations. This already challenging problem becomes even more formidable when such fluids are confined to very small spaces. Therefore, one should resort to a more fundamental description of the fluid behaviour, where further insights are obtained by directly simulating the flow physics based on the interactions between particles.

These deterministic techniques model the time evolution of individual atoms and their collisions through pairwise potential energy functions, by solving their corresponding Newton’s equation of motion. In the case of hard spheres, the exact description in the whole range of fluid densities is produced using event-driven molecular dynamics (EDMD) simulations ([Alder & Wainwright, 1959](#)). The key assumption underpinning the EDMD routine is that at any time instant in the entire system, there occurs at most one collision of infinitesimal duration. Simulations based on discrete potentials, such as the hard-sphere one in [Eq. \(2.1\)](#), are event-driven, in the sense that the time of the next collision can be fully determined on beforehand. Therefore, the system is analytically integrated, in a single numerical time step, to the time at which the next event occurs. A brief overview of the different steps involved in the algorithm for EDMD is presented next ([Pöschel & Schwager, 2005](#)). Despite the availability of some open-source alternatives ([Bannerman et al., 2011](#)), in this case we have preferred to develop our own in-house code using Fortran 90 language.

Initially, particles are randomly distributed in the computational domain, ensuring that they do not overlap, i.e. their centres are separated by a distance larger than σ . Likewise, the initial velocities are sampled from the Maxwellian distribution by using the Box-Muller algorithm ([Box & Muller, 1958](#)). This process should produce a null mean velocity if working with an infinite number of particles in the simulation box, as the Maxwellian in one dimension is a standard normal distribution. Nevertheless, when working with a finite number of molecules, the mean velocity sampled from this methodology could be different from zero, and so the initial velocities are re-set by subtracting the average velocity to each particle i — which, otherwise, might cause drifting issues in the transient state.

The most computationally demanding part of EDMD simulations is to compute the collision times of each pair of interacting particles, which are needed to determine the next collision event occurring in the system. It is worth to emphasise that the system time is not advanced by a fixed time step as in regular MD, but according to the

sequence of collision events which depends on the positions and velocities of particles. In order to determine whether two particles i and j are going to collide based on their current velocities \mathbf{u}_i and \mathbf{u}_j , there must be a solution t_{ij}^* larger than the current time t that satisfies

$$\left| \left[\mathbf{r}_i + (t_{ij}^* - t) \mathbf{u}_i + \frac{1}{2} \mathbf{F}_a (t_{ij}^* - t)^2 \right] - \left[\mathbf{r}_j + (t_{ij}^* - t) \mathbf{u}_j + \frac{1}{2} \mathbf{F}_a (t_{ij}^* - t)^2 \right] \right| = \frac{\sigma_i}{2} + \frac{\sigma_j}{2}. \quad (2.19)$$

To express this equation in a more convenient quadratic form, we can mathematically rearrange it as a function of the relative positions $\mathbf{r}_{ij} = \mathbf{r}_i - \mathbf{r}_j$ and velocities $\mathbf{u}_{ij} = \mathbf{u}_i - \mathbf{u}_j$, so that

$$(t_{ij}^* - t)^2 + 2(t_{ij}^* - t) \frac{\mathbf{r}_{ij} \cdot \mathbf{u}_{ij}}{\mathbf{u}_{ij}^2} + \frac{\mathbf{r}_{ij}^2 - \sigma_{ij}^2}{\mathbf{u}_{ij}^2} = 0, \quad (2.20)$$

where $\sigma_{ij} = \sigma_i/2 + \sigma_j/2$. The (trivial) necessary condition for a collision is that particles must approach each other, $\mathbf{r}_{ij} \cdot \mathbf{u}_{ij} < 0$, which occurs when [Eq. \(2.20\)](#) has a solution, namely if the following inequality is satisfied

$$\left[\frac{\mathbf{r}_{ij} \cdot \mathbf{u}_{ij}}{\mathbf{u}_{ij}^2} \right]^2 + \frac{\sigma_{ij}^2 - \mathbf{r}_{ij}^2}{\mathbf{u}_{ij}^2} > 0. \quad (2.21)$$

The time t_{ij}^* at which the collision between particles i and j occurs is therefore

$$t_{ij}^* = t + \frac{\mathbf{r}_{ij}^2 - \sigma_{ij}^2}{- \mathbf{r}_{ij} \cdot \mathbf{u}_{ij} + \sqrt{(\mathbf{r}_{ij} \cdot \mathbf{u}_{ij})^2 + \mathbf{u}_{ij}^2 (\sigma_{ij}^2 - \mathbf{r}_{ij}^2)}}. \quad (2.22)$$

Besides collisions between molecules themselves, the other kind of event that particles can experience is with the walls of the channel. Provided that all particles continue to move at their present velocity, the collision time with the boundaries can be determined based on the distance they have to travel as if there were no other elements in the system. Importantly, we must account for the finite size of molecules, and so the collision would take place when the centre of the molecule is one radius $\sigma/2$ away from the wall. For planar geometries, this procedure is straightforward as there are two walls, whereas for cylindrical ones we would need to determine the exact collision spot with the circular-shaped wall first. This methodology is detailed in [Appendix B](#).

The behaviour of the particles close to the boundaries of the simulation box in the non-confined dimensions is described by periodic boundary conditions (PBCs). These are introduced to mimic the thermodynamic limit, i.e. systems composed of an infinite number of particles, which cannot be simulated in practice due to computational constraints. When a particle leaves on one side of the simulation box, it re-enters from the opposite side at the same plane with its velocity unchanged. Therefore, the use

of PBCs allows the simulation to proceed as if the simulation box was surrounded by identical copies of itself. Importantly, the minimum image convention, widely used in regular MD simulations, is not applicable in event-driven methods because a particle i does not necessarily collide with the nearest image of the particle j .

An important aspect to consider are rounding errors in the numerical calculations of the collision times, which can cause overlap between particles in fluid-fluid collisions or penetration of the particle inside the boundary in fluid-wall collisions. Despite there is not perfect protection against these errors, most overlaps are avoided by not performing the propagation step in full length, such that the particles always keep a small distance before collisions. Therefore, to reduce the occurrence of these problems, a small tolerance value (in the order of magnitude of 10^{-8}) is subtracted from the earliest collision time for each event.

The pairwise particle collision times has to be initially computed for all combinations of molecules i, j in the system, as well as the collision times of all molecules i with the walls so that the next event can be selected based on the minimum of all of these, t^* . Once the collision time for the upcoming event has been determined, the positions of all particles is updated and advanced to this time t^*

$$\mathbf{r}_i^* = \mathbf{r}_i + (t^* - t) \mathbf{u}_i + \frac{1}{2} \mathbf{F}_a (t^* - t)^2. \quad (2.23)$$

The post-collisional velocities of the collision partners ci, cj are obtained from the pre-collisional ones through elastic hard-sphere dynamics

$$\mathbf{u}_{ci}^* = \mathbf{u}_{ci} - \left[(\mathbf{u}_{ci} - \mathbf{u}_{cj}) \cdot \tilde{\mathbf{k}} \right] \tilde{\mathbf{k}}, \quad (2.24)$$

$$\mathbf{u}_{cj}^* = \mathbf{u}_{cj} + \left[(\mathbf{u}_{ci} - \mathbf{u}_{cj}) \cdot \tilde{\mathbf{k}} \right] \tilde{\mathbf{k}}, \quad (2.25)$$

whereas if the event involves a fluid-wall collision, then its post-collisional velocity \mathbf{u}_{ci}^* is calculated from the Maxwell scattering kernel, as detailed in [Section 2.4](#).

The EDMD algorithm advances by seeking the next event, and the standard procedure involves producing an information list that stores the next collision time and collision partner (either another molecule or the wall) for each particle in the system. When a collision occurs, the only entries from this list that are updated from scratch are those associated with the collision partners, since their velocity vectors have changed according to the aforementioned rules. The remaining collision times are easily recomputed by subtracting the time of the current event to the previous calculations, and so the next event can be identified. This methodology can be further accelerated by building up more efficient versions using neighbouring lists, link cells methods, and other procedures more commonly used in expensive MD simulations ([Allen & Tildesley, 2017](#)).

Macroscopic fields are evaluated as weighted averages of the of molecular positions \mathbf{r}_i and velocities \mathbf{u}_i . Computer simulations produce information at the microscopic level, generating ensembles of the microscopic information for the N molecules in the system. A larger number of molecules will decrease the intrinsic noise characteristic of particle-based methods, albeit at the expense of a greater computational burden. In itself, this information is of little relevance compared to (macroscopic) thermodynamic quantities, which are generally evaluated using P_t partitions that divide the simulation domain along the flow characteristic length in “bins” or “cells” of equal width, with volume V_c . For the fluid-wall system of consideration, we found that cell widths of either $\sigma/20$ or $\sigma/10$ did not affect the simulation results. The number density is computed based on the positions of individual molecules as

$$\langle n_c(r) \rangle = \frac{\langle N_c(r) \rangle}{V_c(r)} = \frac{1}{SV_c(r)} \sum_{k=1}^S \sum_{c=1}^{P_t(t_k)} N_c(r, t_k), \quad (2.26)$$

where S is the total number of samples, $N_c(t_k)$ denotes the number of molecules occupying a given cell c at sampling time k and $\langle \cdot \rangle$ denotes mean quantities. On the other hand, for the velocity, several procedures might be carried out as reviewed by [Tysanner and Garcia \(2004\)](#). In the case of non-equilibrium systems, where an external force \mathbf{F}_a is included in the simulation to induce uni-directional flow, the cumulative average measurement yields the unbiased mean velocity

$$\langle \mathbf{v}_c(r) \rangle = \frac{\mathbf{v}_c(r)}{N_c(r)} = \frac{\sum_{k=1}^S \sum_{c=1}^{P_t(t_k)} N_c(r, t_k) \mathbf{u}_c(r, t_k)}{\sum_{k=1}^S \sum_{c=1}^{P_t(t_k)} N_c(r, t_k)}. \quad (2.27)$$

Starting from the microscopic velocities, one can also obtain the temperature of the system using the famous equipartition theorem ([Allen & Tildesley, 2017](#)), that relates the kinetic energy of the system with its temperature. If the simulations are run for a sufficiently long time, results based on time averages, i.e. sampling positions and velocities at different instantaneous times t within a single run, will agree with results based on ensemble averages, i.e. performing multiple independent runs of the same system with different initial conditions. This constitutes the so-called ergodic hypothesis, which states that all accessible microstates are equally probable over a long period of time, for which there is no general proof but overwhelming practical evidence. The caveat is that the minimum time for which the ergodic hypothesis holds true is not known on beforehand, and therefore results are likely to be associated with statistical uncertainties — that can be attenuated by running for longer simulation times.

Self-Diffusion of Confined Fluids

N.B. This chapter has been published in: Corral-Casas, C., Gibelli, L., Borg, M.K., Li, J., Al-Afnan, S.F.K., Zhang, Y. “Self-diffusivity of dense confined fluids”. *Physics of Fluids* 33, 082009 (2021). Editor’s Pick.

Molecular transport through tight porous media is crucial to shale gas exploration, but deeper insights of the elemental physics are still required, particularly under high pressures and nanoscale confinements, where the Navier-Stokes and Boltzmann solutions are no longer valid. In this work, a fundamental and systematic study of self-diffusion is carried out using event-driven molecular dynamics simulations, varying fluid rarefaction, confinement and surface microscopic roughness. Often a source of debate, here it is proved that the self-diffusivity from the Einstein relation can still be used with the Fickian formalism, despite the strong fluid inhomogeneities under confinement. We differentiate between fluid-fluid and fluid-wall collisions to identify the interplay of the underpinning diffusive mechanisms, namely molecular and Knudsen diffusion. We find that the Bosanquet formula, which has been used for describing rarefied gases, is also able to provide a good semi-analytical description of self-diffusivities in confined fluids, as long as the pore height is not smaller than five molecular diameters. Importantly, this allows us to predict the self-diffusion coefficient, regardless of the fluid rarefaction, confinement state, and surface roughness, in a wide range of Knudsen numbers that was not possible before. Finally, we notice that a previously identified linear scaling of self-diffusivities with confinement is only valid in the limit of low densities and frictionless walls.

3.1 Literature Survey

Fluids confined to nanoscale geometries are ubiquitous in biological and engineering applications (Casanova et al., 2020; Celebi et al., 2014; Holt et al., 2006), such as in nanocatalyst construction (Fihri et al., 2011), nanostructured water filtration membranes (Shannon et al., 2008), and proton transport within fuel cells (Z. Liu et al., 2002).

A notable application that motivates this research is the transport of hydrocarbon fluids stored within sedimentary shale rocks (Cathles et al., 2012; Germanou et al., 2020; Phan et al., 2020), where the gas-gas and gas-surface physics through the naturally-formed nanopores deviate from our current understanding and modelling capabilities.

In general, the behaviour of confined fluids is still poorly understood for several reasons. The first challenge appears when the mean free path (MFP) λ is comparable to the flow characteristic length, related to the pore height H , and so the ratio between both quantities, i.e. Knudsen number, is moderately larger than zero. In this case, the assumption of local thermodynamic equilibrium breaks down (Gad-el Hak, 1999), and subsequently the continuum description of fluids fails. One of the most recognisable consequences of non-equilibrium effects at the microscale is the so-called Knudsen paradox, which shows up when a constant pressure difference drives a rarefied flow along a narrow straight channel. The mass flow rate displays a characteristic minimum as the inlet pressure is reduced (Knudsen, 1909), being in sharp contrast with the monotonic decrease predicted by the Navier–Stokes equations.

A second challenge occurs when the pore characteristic length is similar to the diameter of fluid molecules σ , as typically occurs in shale reservoirs, where pore sizes are very tight with mesopores ($H \sim 20\text{--}200 \text{ \AA}$) and micropores ($H < 20 \text{ \AA}$) dominating the storage of light hydrocarbon fluids (Loucks et al., 2009). In these conditions, molecular ordering happens inside the pores and the effect of dense fluid packing is magnified. Surprisingly, the recent measurement of Poiseuille mass flow rates through ultra-tight pores, which are characterised by small confinement ratios $R = H/\sigma$, was found to follow a monotonic increase with Knudsen number (L. Wu et al., 2016). Although the Boltzmann equation predicts the existence of the Knudsen minimum (Bahukudumbi & Beskok, 2003; Cercignani & Daneri, 1963; Tatsios et al., 2015) and it may explain its disappearance in bent (W. Liu et al., 2018) and short (Ho et al., 2020) channels, it cannot be used to investigate the effects arising due to confinement, which are responsible for the Knudsen minimum disappearance observed in straight channels.

A third challenge arises when one considers the high pressures in these unconventional reservoirs. Pressures can range from 5 to 50 MPa (K. Wu et al., 2016), and consequently fluid densities are beyond the dilute-gas Boltzmann limit (Kremer, 2010). Therefore, the space correlations of molecules, which are disregarded in the derivation of the Boltzmann equation, need to be considered. The Enskog equation approximately considers that the positions of molecules are statistically correlated in dense fluids, and recently it has been shown to predict the Knudsen minimum disappearance within straight channels of molecular dimensions (Sheng et al., 2020). However, a satisfactory explanation of the underlying mechanisms that justify these mass flow rates is missing, particularly in the transition range of flow regimes ($0.1 \lesssim Kn \lesssim 10$).

A possible theoretical explanation of the Knudsen minimum disappearance in straight channels relies on a change of the underpinning physics, where mass transport is no longer occurring because of viscous convection. In pressure-driven flows within very tight geometries, there is not enough room for molecules to develop different velocities based on their spatial position, because of the limited number of molecular layers in the confining direction and the large amount of collisions with walls. Indeed, the fluid velocity profile switches from the Poiseuille parabolic shape to plug-like as the characteristic dimension of the channel reduces (J. Chen et al., 2017; Kazemi & Takbiri-Borujeni, 2016), suggesting that diffusion now dictates the fluid dynamics in this context. Given that the Knudsen minimum only disappears when the confinement is on the molecular scale, it is clear that a deeper understanding of diffusive dynamics is of paramount importance to better explain the fluid behaviour, and so this will be the scope of the present work.

The classical modelling approach to diffusive processes is based on Fick's law, where diffusion follows a linear response with the gradient of the species' concentration along the streamwise direction. The simplest diffusive phenomenon, i.e. Brownian motion of identical particles without a net flow induced by a thermodynamic gradient, is referred to as self-diffusion and can be studied by a process of tagging and tracking particles. In a bulk system of a pure substance at equilibrium, the self-diffusion is defined as a measure of the mobility of a single tagged particle within the pool of mechanically indistinguishable particles. The constant of proportionality, which is known as the self-diffusivity D , is commonly identified with the mean square displacement (MSD) of molecules in bulk fluids, see Section 1.2. The value of D depends on the physical mechanisms that govern diffusion, e.g. molecular and Knudsen diffusion amongst many others (Xiao & Wei, 1992). Molecular diffusion dominates in the hydrodynamic limit for $Kn \lesssim 0.01$, when interactions are mainly between fluid particles, whereas for $Kn \gtrsim 10$ the diffusive dynamics can be simplified to Knudsen diffusion, consisting of free flights of particles between collisions with walls.

Although Fick's law is the cornerstone of modelling diffusion transport in porous media (Coasne, 2016), its validity at the nanoscale is not obvious and so it has been subjected to many studies (Cui, 2005; Mon & Percus, 2002). For the range of confined channels in which single-file diffusion does not take place, this linear theory is assumed to be valid but some doubts arise with respect to the proportionality factor that has to be used within its formulation. Specifically, the non-bulk structure of the fluid may involve the breakdown of the MSD approach for evaluating the self-diffusion coefficient (MacElroy et al., 2001; Schoen et al., 1988) and, indeed, the lower R threshold that dictates the validity of the MSD-based self-diffusivity in the Fickian framework

is still not well defined (McDermott & MacElroy, 2004). Local diffusion coefficients have also been introduced to cope with the fluid inhomogeneity (Krekelberg et al., 2017; P. Liu et al., 2004; Mittal et al., 2008), but the procedures for averaging the local values to compute global quantities are somehow phenomenological in nature.

Molecular dynamics (MD) computer experiments have served as a useful reference for evaluating the self-diffusion coefficient in both bulk (Alder et al., 1970; Erpenbeck & Wood, 1991; Sigurgeirsson & Heyes, 2003; Speedy, 1987) and confined fluids (Cracknell et al., 1995; Krekelberg et al., 2011; Mittal et al., 2006, 2007). However, a satisfactory overall picture of the diffusion dynamics of fluids under confinement is still lacking, and there are no analytical derivations to predict self-diffusivities accurately in the entire range of Knudsen numbers. Importantly, the crossover between molecular and Knudsen diffusive mechanisms has not been generalised beyond the rarefied description of non-confined gases (Lund & Berman, 1966; Pollard & Present, 1948; Roberts, 1971), and as we explain above, this transition flow regime under tight confinement and high fluid packing is an area with critical implications to shale gas media.

The aim of this chapter is to systematically investigate the effect of rarefaction, confinement, and wall microscopic roughness on the self-diffusion process. The novelty of this study is presented next: first, we measure the self-diffusion coefficient in a wide range of fluid densities (from dense to rarefied), channel heights (from tight to quasi-bulk), and microscopic wall properties (from rough to frictionless) that has not been subjected to investigation before. Here, we use event-driven molecular dynamics (EDMD), which, compared to the Enskog theory, provides the exact description of the monatomic hard-sphere dynamics in the whole range of reduced fluid densities. Second, we assess the validity of using the well-known MSD procedure for studying diffusion in strongly inhomogeneous fluids. Third, we use a splitting procedure of the colliding molecules to understand the interplay between molecular and Knudsen mechanisms in the transition regime, and how these are influenced by confinement and rarefaction. This calls into question previously observed diffusive scaling laws. Fourth, we develop a semi-analytical theory that predicts the self-diffusion coefficient in the wide parametric space of consideration, which has so far been missing in the literature.

The rest of the chapter is organised as follows. In Section 3.2 we outline the EDMD methodology and the procedures for calculating self-diffusivities, from either following particles' trajectories through their random walk or according to Fickian theory. Results for self-diffusivity are presented in Section 3.3, including the validation of MSD and Fickian approaches, splitting results of diffusive mechanisms, and demonstration of the proposed theory. Finally, Section 3.4 concludes this piece of work by summarising the main findings.

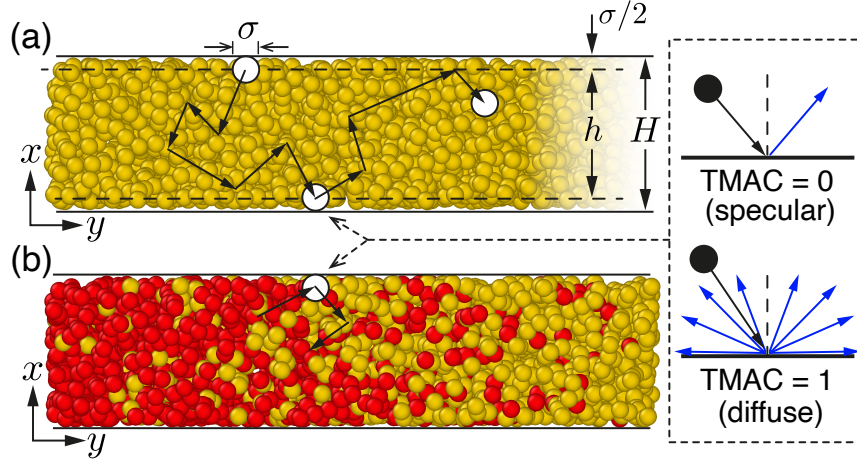


Figure 3.1: Two independent methods for computing the self-diffusivity of confined fluids: **(a)** Einstein relation, by measuring the average molecular MSD, and **(b)** Fick's law by changing the colour tag of particles (type A: red, type B: mustard) as these cross the boundaries, followed by computing the steady-state tagged transport flux.

3.2 Methodology

3.2.1 Problem Formulation

A system composed of N hard-sphere particles with diameter σ is studied in a slit geometry, defined by two infinite parallel plates at a distance $H = h + \sigma$ apart, where h is the effective transversal space accessible to the centre of spherical molecules (see [Figure 3.1](#)). The walls are assumed to be structureless flat surfaces, and the fluid-wall interactions are described by the Maxwell scattering kernel with tangential momentum accommodation coefficient (TMAC). Namely, a fraction of the molecules impinging on the wall (given by TMAC) is diffusely re-emitted after being thermalised with the wall, while the remaining partition ($1 - \text{TMAC}$) is specularly reflected. This is the simplest possible simulation setup that permits one to capture the key features of the diffusion process ([H. Liu et al., 1998](#)).

The self-diffusion coefficient is evaluated by two different methods, as illustrated in [Figure 3.1](#):

(a) Under equilibrium conditions, the self-diffusivity is computed using the Einstein relation ([Einstein, 1956](#)), measuring the squared deviation of each particle position \mathbf{r}_i , with respect to a reference position over time t , as follows

$$D^E = \lim_{t \rightarrow \infty} \frac{\langle \Delta \mathbf{r}^2(t) \rangle}{2dt} = \lim_{t \rightarrow \infty} \frac{1}{N\tau} \sum_{i=1}^N \sum_{j=0}^{\tau} \frac{|\mathbf{r}_i(t + t_j) - \mathbf{r}_i(t_j)|^2}{2dt}. \quad (3.1)$$

Here, d is the dimensionality of the system, and $\langle \Delta \mathbf{r}^2(t) \rangle$ is double averaged over the number of particles N and multiple time origins τ , where $\tau > t_j$ for all j . Unlike the bulk case, diffusion is not an isotropic process in confined geometries (Karniadakis et al., 2005), and the self-diffusivity in the x -direction takes a lower value than in the yz -plane, with $d = 2$ to compute the mean D^E in these two symmetric dimensions.

(b) In the presence of a concentration difference in the streamwise direction, the self-diffusivity is computed by using the phenomenological Fick's first law (Cussler, 2009), i.e. as the proportionality factor between the concentration gradient dC/dy and the flux of particles J that arises as a result of this driving force

$$D^F = -\frac{J}{dC/dy}. \quad (3.2)$$

Two remarks are in order. First, the Fick's law refers to the linear relation between mass flux and concentration gradient, regardless of the fluid rarefaction state and not only in the continuum regime (Guo et al., 2019). Second, the Fickian self-diffusivity is different from the transport diffusivity that is defined in presence of a convective flow (Li et al., 2021).

Three dimensionless groups can be identified to systematically describe the different diffusive processes that may take place in the current problem formulation: the Knudsen number $Kn = \lambda/h$, the confinement ratio $R = H/\sigma$, and the reduced density $\eta = n\pi\sigma^3/6$, where n is the number density. Besides differentiating between flow regimes, the Knudsen number determines the diffusive mechanism that prevails at a given rarefaction and confinement degrees. The reduced density represents the packing fraction of the fluid, e.g. larger η implies less free space for the particles to move. By using the Enskog theory, these groups are interrelated through

$$Kn = \frac{\sigma}{6\sqrt{2}\eta\chi(\eta)} \frac{1}{h} = \frac{1}{6\sqrt{2}\eta\chi(\eta)} \frac{1}{R}, \quad (3.3)$$

where χ is the contact value of the pair correlation function in a hard-sphere fluid in uniform equilibrium (Kremer, 2010). An approximate but accurate expression for χ can be obtained from the hard-sphere fluid equation of state proposed by Carnahan and Starling (1969)

$$\chi = \frac{1}{2} \frac{2 - \eta}{(1 - \eta)^3}. \quad (3.4)$$

3.2.2 Simulation Setup

The time evolution of the hard-sphere dynamics is simulated using event-driven molecular dynamics (EDMD), which is an adaptation of MD simulations to discrete potential systems. This simulation technique is event-driven in the sense that the state of the system jumps from one time to another corresponding to the earliest collision event. The time step is not constant throughout the simulation run, like in MD simulations, as it depends on the spatial coordinates and velocities of all molecules in the system. The algorithm consists of three basic steps: **(a)** evaluating the time of the earliest collision event, **(b)** moving ballistically all particles for that time interval, and **(c)** updating the velocity of the particles that have collided with another particle or the wall, according to hard-sphere dynamics or the Maxwell scattering kernel, respectively. Beyond this brief outline, a more complete review has been already presented in [Section 2.5](#).

The main advantage of EDMD relies on the computational savings with respect to simulations that consider soft potentials, like Lennard-Jones, because it avoids the expensive calculation of multibody intermolecular forces. To simplify the notation and data analysis in the rest of the paper, all the physical quantities are made dimensionless by considering the molecular diameter σ as the reference length, the particle mass m as the reference mass, and $\sigma/\sqrt{kT/m}$ as the reference time, where the denominator is the reference thermal velocity, with k being the Boltzmann constant and T the temperature. Accordingly, self-diffusivities will be expressed in dimensionless $\sigma\sqrt{kT/m}$ units.

The computational domain is an orthogonal box of dimensions $[H; \ell_y; \ell_z]$, applying periodic boundary conditions in the y - and z -directions. The cross section of the simulation box $H \times \ell_z$ is chosen to match the target reduced density η . Note that a careful choice of the streamwise length ℓ_y is required when evaluating the self-diffusivity through [Eq. \(3.2\)](#), as will be discussed in [Section 3.3.1](#). The number of particles was set over 5×10^3 in order to reduce the system-size dependence of the computed self-diffusivities ([Yeh & Hummer, 2004](#)). Initially, molecules are randomly placed across the simulation box ensuring that they do not overlap, and velocities are sampled from the Maxwell-Boltzmann distribution by using the Box-Muller algorithm. The reduced density is varied in the range $\eta = [0.00005, 0.35]$, with confinement ratios within $R = [2, 100]$. Consequently, the Knudsen number spans all flow regimes, i.e. $Kn \sim [0.001, 1000]$ as given by [Eq. \(3.3\)](#).

As detailed in [Section 3.2.1](#), the self-diffusion coefficient has been computed using two different approaches. The computation of self-diffusivities by [Eq. \(3.1\)](#) is performed based on equilibrium simulations. Time averaging starts when the initial ballistic regime dies out and the simulation time is set long enough to ensure that the ergodic hypothesis is satisfied. Note that there are two main sources of uncertainties in evaluating self-diffusion coefficients using this technique. First, accurate self-diffusivity results require

an unbiased MSD, and therefore uncorrelated sampling (Pranami & Lamm, 2015) needs to be considered when maximising the number of samples per run, e.g. multiple time origins t_j besides the initial simulation time t_0 . Secondly, using the Einstein relation is associated with relevant uncertainties, because of the unattainable search of perfectly linear regions between MSD and time (Fayon & Sarkisov, 2019).

The calculation of the self-diffusivity by Eq. (3.2) uses the same setup, but particles are tagged as either type A (tracer) or type B (solvent), with all fluid molecules being mechanically indistinguishable. The overall density, accounting all tagged and non-tagged particles, remains constant throughout the entire domain in the streamwise dimension. Initially, all molecules are assigned to type B. During the simulation, those which cross the right-hand and left-hand side boundaries of the simulation box are assigned to type A (red) and type B (mustard), respectively, independently of their initial tag (see Figure 3.1). This mimics the presence of two reservoirs, virtually full of tracers and of solvent in both ends of the channel. Molecular motion and collisions are performed in the same manner for both types, but macroscopic quantities such as number density and mean velocities are collected separately for each of them. The concentration profile of type A particles is then allowed to relax, and the time averaging starts at the steady state when the profile becomes linear in the middle of the simulation box, a few molecular diameters away from the boundaries to avoid non-diffusive end effects. The concentration gradient is then computed by minimising the mean square error of the linear fit to the concentration field of type A particles in this central region.

3.3 Results and Discussion

3.3.1 Fickian and Einstein Self-diffusivities

The Einstein and Fickian self-diffusivities match under bulk conditions (Kärger & Valiullin, 2013), but their agreement has been questioned in tightly confined geometries, as introduced in Section 1.2.1. Preferential fluid packing next to the walls extends to a larger relative portion of the channel when R values are low. In this condition, most of the MSD trajectories are made up of contributions from particles crossing inhomogeneous areas with different local densities. Accordingly, it is not obvious whether the microscopic Einstein self-diffusivity still agrees with the coefficient coming from the macroscopic Fickian theory. In order to shed light on this question, we compute the self-diffusion coefficients based on Eq. (3.1) and Eq. (3.2) for a wide range of η and R , with emphasis on large reduced densities that preferentially lead to non-homogeneous density profiles.

Table 3.1: Self-diffusivities for fluids at different confinements for $\eta = 5 \times 10^{-4}$. The Fickian (D^F) and Einstein (D^E) results are in very good agreement when $\ell_y \gtrsim 2\lambda$, expressed by **bold rows**.

$\eta = 5 \times 10^{-4}$	$R = 50$		$R = 2$	
$\ell_y (\ell_y/\lambda)$	D^F	D^E	D^F	D^E
10 (0.042)	20.157	49.014	1.262	2.319
40 (0.170)	28.688	48.828	1.745	2.261
80 (0.340)	34.243	48.483	1.896	2.301
500 (2.124)	46.862	47.221	2.359	2.340
1000 (4.248)	47.501	48.590	2.376	2.396

Table 3.2: Self-diffusivities for fluids at different confinements for $\eta = 5 \times 10^{-3}$. Again, the two methodologies are in very good agreement when $\ell_y \gtrsim 2\lambda$.

$\eta = 5 \times 10^{-3}$	$R = 20$		$R = 5$	
$\ell_y (\ell_y/\lambda)$	D^F	D^E	D^F	D^E
10 (0.430)	7.627	10.376	3.073	3.944
20 (0.859)	8.557	10.357	3.396	3.883
30 (1.289)	9.073	10.383	3.558	3.951
50 (2.148)	10.297	10.241	3.789	3.889
75 (3.222)	10.349	10.368	3.817	3.893

However, a preliminary observation in our results must be made before moving into a more detailed comparison. As shown in [Table 3.1](#) and [Table 3.2](#), the Einstein self-diffusivity D^E does not significantly depend on the length of the domain in the streamwise direction, ℓ_y , which is expected since the MSD measurements of particles continue seamlessly across the periodic boundaries, as if to represent an infinitely long slit. On the other hand, this is not the case for the Fickian self-diffusivity, in which D^F is seen to increase steadily with ℓ_y and eventually levels off for $\ell_y \gtrsim 2\lambda$, regardless of the confinement ratio and the fluid density. This occurs because D^F is now influenced by the inlet– and outlet–type boundary conditions, and a critical length is required to offset the non-equilibrium perturbation of particles changing tag at the boundaries. We find this requirement on the streamwise length to be particularly severe in the rarefied regime, due to the inverse proportionality between η and λ .

[Figure 3.2](#) shows the Einstein and Fickian self-diffusivities as a function of the confinement ratio R for different large packing fractions, when walls are fully diffuse (TMAC = 1). For the reasons mentioned above, the Fickian self-diffusivities are obtained by running simulations where the streamwise length of the computational box is larger than two molecular mean free paths. Our results reveal that the self-diffusion results obtained from [Eq. \(3.1\)](#) and [Eq. \(3.2\)](#) are almost indistinguishable in the whole parametric

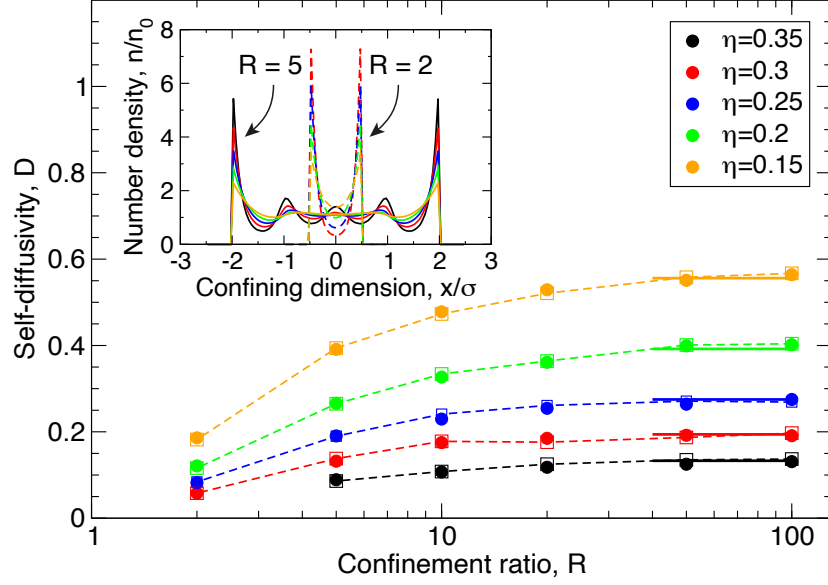


Figure 3.2: Self-diffusivities computed using the Einstein relation (filled circles) and as a proportionality factor according to Fick's law (empty squares). Comparisons for accuracy in the large R limit are made with results from Heyes et al. (2007), represented by solid horizontal lines. Inset: fluid layering in confined channels, deviating from the homogeneity of bulk fluids defined by $n/n_0 = 1$.

space. Particularly, Einstein and Fickian self-diffusivities agree under tight confinement ($R \lesssim 20$) despite the strong fluid inhomogeneities that exist (see the inset of Figure 3.2, note that the density profiles are defined based on H and not in h , as in Figure 1.1b or in subsequent chapters). It is worth stressing that this conclusion may be a consequence of the slit geometry considered in this study, which allows particles to swap places in the spanwise z -direction even in molecular-like confinements ($R \leq 3$) where single-file transport is expected in the streamwise direction. Hence, diffusion is not anomalous although there is not enough room for particles to overtake their counterparts through the confining x -dimension, see Table 3.1 for $R = 2$ results. This 2D planar channel feature ensures that the linearity between MSD and time assumed by Eq. (3.1) always holds, and anomalous diffusion never takes place.

Also in Figure 3.2, it can be observed that at a given reduced density η , the molecular mobility decreases with narrower channels because, on average, particles collide more frequently with the confining walls. Throughout these collisions, particles experience a change in momentum that hinders their displacement in the two non-constrained y, z -directions, parallel to the walls (as $\text{TMAC} = 1$). For this reason, the self-diffusivity shows a decreasing tendency with increasing confinement, which is logarithmic-like as predicted theoretically by some studies (Bocquet & Barrat, 1995; Simonnin et al., 2017) (dashed lines are here included as a guide to the eye). If the confinement ratio is large ($R \geq 50$), an excellent agreement is found between our simulations of a dense fluid

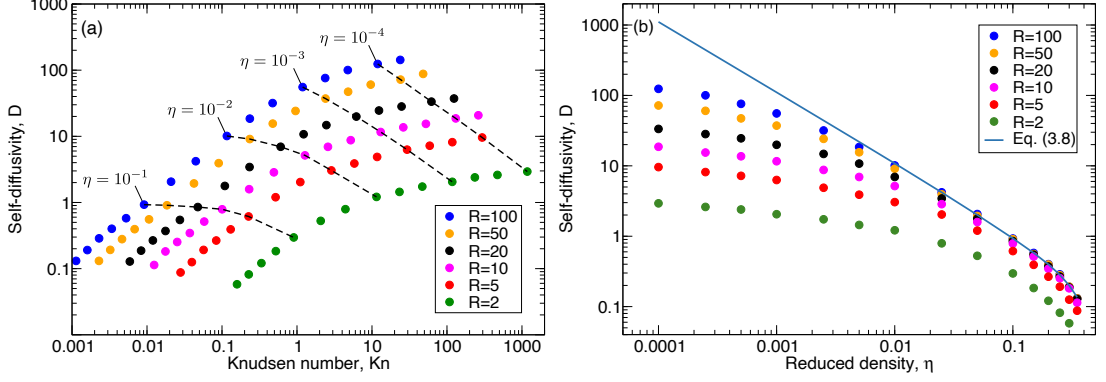


Figure 3.3: Self-diffusivities from EDMD simulations for various confinement ratios as they vary with: (a) Knudsen number and (b) reduced density. Dashed lines in (a) show data at equal packing fractions, where gas is considered as dense for $\eta \gtrsim 0.01$ and dilute otherwise. The solid line in (b) represents the theoretical prediction for the molecular self-diffusivity.

and the bulk self-diffusion coefficients at the same reduced density, with all deviations below 2.5%. The results shown in Table 3.1, Table 3.2 and Figure 3.2 represent the validation of the EDMD code, which was developed in house, to accurately compute the self-diffusion coefficient for both confined and bulk-like fluids.

The self-diffusivity results that are presented in the remaining part of the chapter are obtained using the Einstein relation from Eq. (3.1). This choice stems from its overall lower computational cost over the Fickian approach, and also because of the convenience of producing self-diffusivities independent of ℓ_y , as shown in Table 3.1 and Table 3.2. To provide a more comprehensive picture, besides the self-diffusivities reported in Figure 3.2, we also show results for the rarefied end of reduced densities (lower η) in Figure 3.3. Note that $\eta \approx 0.01$ can be roughly considered as the threshold between dense and dilute gas, since for lower values of the reduced density the compressibility factor of the fluid deviates from unity (ideal gas behaviour) less than 5%, see Eq. (2.2).

Self-diffusion coefficients are presented as a function of Kn in Figure 3.3a, while the analysis is performed with respect to η in Figure 3.3b. As expected, self-diffusivities increase (decrease) with Knudsen number (packing fraction) because particles have more room to move freely before colliding with another entity in the system. The Knudsen diffusion mechanism, where Kn goes to infinity because of the zero density limit, is associated with the largest mobility for a given R . The lower self-diffusivity threshold is related to larger reduced densities through the molecular diffusion mechanism, where the fluid enters the metastable regime after freezing at $\eta = 0.494$ (Sigurgeirsson & Heyes, 2003).

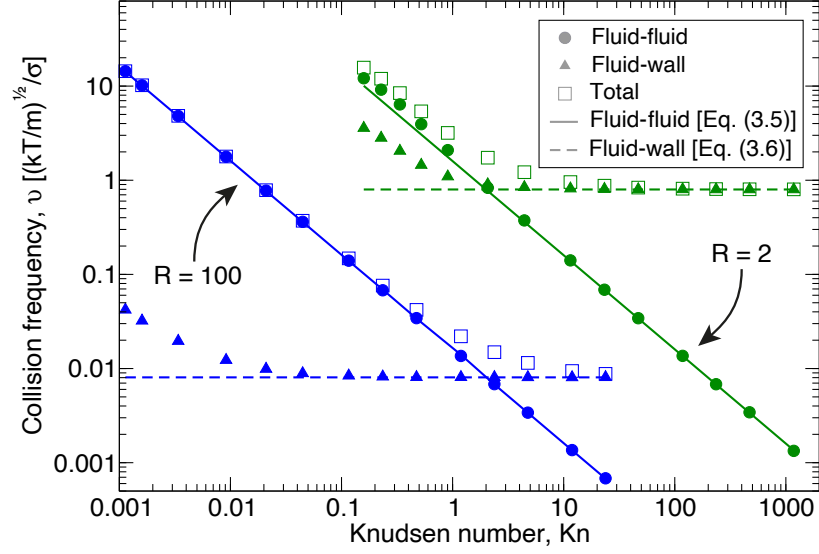


Figure 3.4: Fluid-fluid, fluid-wall, and total collision frequencies with respect to Knudsen number for $R = 2$ (green) and $R = 100$ (blue).

3.3.2 Splitting Fluid-Fluid and Fluid-Wall Collisions

Collisions are the main driving mechanism for diffusion, and as such, making a distinction between fluid-fluid (molecular) and fluid-wall (Knudsen) collisions would give us a better understanding of how these are influenced by rarefaction and confinement. Particles are scattered isotropically when they collide with other particles, which is in clear contrast to when they collide with the wall, where particle re-emission occurs towards the half-space occupied by the fluid.

Figure 3.4 shows the different collision frequencies, defined per unit molecule, between fluid particles (ν_{FF}), fluid particles and the wall (ν_{FW}), and the overall sum ($\nu_{FF} + \nu_{FW}$), measured directly from our EDMD simulations in two slits characteristic of tight ($R = 2$) and unconfined ($R = 100$) conditions. For “small” Knudsen numbers ($Kn \lesssim 2$), fluid-fluid collisions dominate as expected. At $Kn \sim 2$, we observe a crossover point for both slits at which fluid-wall and fluid-fluid collisions are similar. For larger Knudsen numbers ($Kn \gtrsim 2$), fluid-wall prevail with respect to intermolecular collisions. A tight confinement has a role in both increasing the number of collisions (ν_{FW} and ν_{FF}), which is attributed to dense effects becoming more prominent, and in narrowing the difference between ν_{FW} and ν_{FF} in the earlier Knudsen numbers, which in this case is at least two orders of magnitude, i.e. ν_{FW} becomes more important for small R .

The fluid-fluid collision frequency ν_{FF} can be estimated from elementary arguments of kinetic theory of a dense gas as the mean thermal speed \bar{v} over the mean free path λ

$$\nu_{FF} = \frac{\bar{v}}{\lambda} = \frac{24}{\sqrt{\pi}} \frac{\eta \chi}{\sigma} \sqrt{\frac{kT}{m}}, \quad (3.5)$$

while a different theoretical derivation is involved when evaluating the fluid-wall collision frequency ν_{FW} , where the characteristic length is no longer the MFP but the particle-centre accessible region h

$$\nu_{FW} = \frac{1}{2} \frac{\bar{v}}{h} = \frac{1}{2} \sqrt{\frac{8kT}{\pi m}} \frac{1}{h}. \quad (3.6)$$

Eq. (3.5) for fluid-fluid collisions agrees very well with our EDMD results, except for slight deviations at low Knudsen numbers in the tight channel ($R = 2$), which occur because small density inhomogeneities are apparent in the middle of the channel for ultra-tight confinements (bulk behaviour is never retrieved within the slit channel). Fluid-wall interactions deviate significantly from Eq. (3.6) at high fluid packing. This occurs because the ordering of fluid density near the wall can be several times higher than the nominal density, on which the theoretical equation has been derived, which leads to an increase in the collision frequency with the wall. For $R = 100$, this effect of fluid-wall collisions due to layering is negligible on the total number of collisions, as can be seen in Figure 3.4, where $\nu_{FF} \gg \nu_{FW}$. However, its effect on $R = 2$ is not negligible.

These findings emphasise the importance of the transition regime ($0.1 \lesssim Kn \lesssim 10$), in which there is an interplay of both fluid-fluid and fluid-wall collisions impacting the self-diffusivity, which are also influenced by ordering at low Kn and high confinement. A more convenient parameter that we will use to distinguish the interplay between the different collision frequencies is the intermolecular collision frequency ratio β , defined as

$$\beta = \frac{\nu_{FF}}{\nu_{FF} + \nu_{FW}} = \frac{2}{2 + Kn}. \quad (3.7)$$

A very good agreement was found between this theoretical approximation and our EDMD results for channels with large R , whereas, as shown in Figure 3.5, Eq. (3.7) overpredicts the actual β with increasing magnitude as R gets smaller. The largest discrepancies are associated with the dense η limit, which produces the lower Knudsen numbers according to Eq. (3.3). As before, the underpinning reason of this discrepancy is that Eq. (3.7) assumes that the fluid is homogeneous, which is not the case for high confinements.

3.3.3 A Semi-Analytical Model for Self-diffusivity

In this section, we derive a semi-analytical model that allows us to predict the self-diffusivity results presented in Figure 3.3. The diffusion assessment will be based on the β values at different flow regimes which, by definition, must take values in the range $[0, 1]$. Small Knudsen numbers, i.e. the continuum regime, are related to β close to unity because of the predominant role of fluid-fluid interactions. On the other hand, large Knudsen numbers in the free molecular regime are associated with small β , which eventually tends to zero when there are just collisions with walls in the ballistic limit.

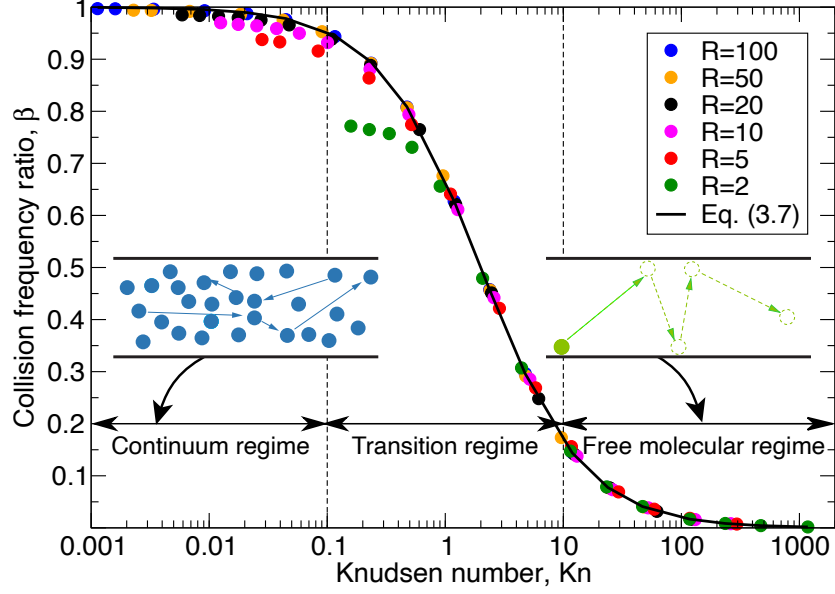


Figure 3.5: Ratio between fluid-fluid and total (fluid-fluid and fluid-wall) collision frequencies with respect to Kn .

Finally, the analysis for transitional Knudsen numbers considers intermediate β values, accounting for both fluid-fluid and fluid-wall collisions in varying degrees. In each case, we identify the predominant physical mechanism and discuss the appropriate analytical expressions for the self-diffusivity.

Continuum Regime (large β values)

For β close to unity, fluid-fluid collisions are the most predominant form of interaction, and the fluid approaches the continuum regime. The classical description of molecular diffusion in the bulk applies, and the following semi-empirical formula can be used to predict the molecular self-diffusivity of a hard-sphere fluid (Erpenbeck & Wood, 1991)

$$D_m = D_E (1 + c_1 \eta + c_2 \eta^2 + c_3 \eta^3), \quad (3.8)$$

where the fitting parameters are $c_1 = 0.0730$, $c_2 = 11.6095$, and $c_3 = -26.9511$, and D_E is the first order approximation of the self-diffusivity according to the Enskog kinetic theory for dense fluids, whose definition involves the Boltzmann-based prediction over the pair correlation function χ

$$D_E = \frac{\sigma}{16\eta} \sqrt{\frac{kT\pi}{m}} \frac{1}{\chi} = \frac{3R\sigma Kn}{8} \sqrt{\frac{2kT\pi}{m}}. \quad (3.9)$$

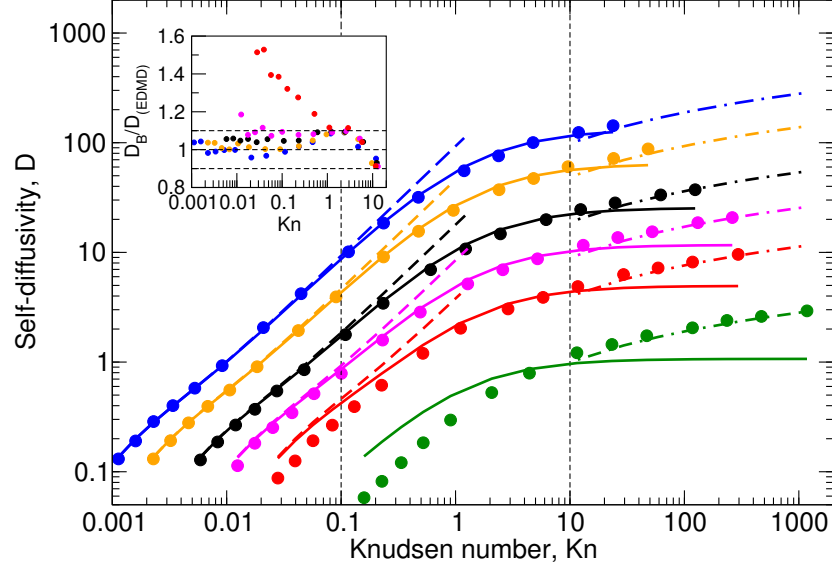


Figure 3.6: Comparison between self-diffusivities from EDMD simulations (solid circles) and Bosanquet predictions, Eq. (3.11) (solid lines). Dashed lines represent the molecular self-diffusivity approximation from Eq. (3.8), whereas dash-dotted lines show the Knudsen self-diffusivity from Eq. (3.10). Inset: ratio of predicted self-diffusion values over EDMD results. Same colour scheme for symbols is used as that in Figure 3.3.

Note that this semi-empirical approximation accurately reproduces simulation results for $\beta \geq 0.9$, i.e. $Kn \leq 0.1$, showing a maximum 5.7% relative error with respect to our EDMD results when $R \geq 20$, as emphasised by the dashed lines in Figure 3.6. In Eq. (3.8), the term within brackets is a correction factor that accounts for dense effects not captured by the Enskog theory.

Free Molecular Regime (small β values)

The first comprehensive experimental study of the free molecular regime was carried out by Martin Knudsen, inspired by the experimental prowess of Poiseuille and the consequences of the kinetic theory derived by Maxwell and Boltzmann (Knudsen, 1909). By studying the pressure-driven flow of gases through capillaries, Knudsen first found agreement with the slip-modified version of the laws of Poiseuille, and then kept decreasing the inlet pressure until the point in which the mean free path was much larger than the capillaries size, i.e. very large Kn . By doing this, he found that the representation of the normalised flow output exhibits an unexpected behaviour when being represented with respect to the inlet pressure, with no clear explanation at the time¹. Specifically, the mass flow rate curve shows a monotonic increase in the free

1. “What the effect of all this will be is hard to say, the problem has not yet been solved even in its first approximation. Perhaps somebody in the audience would like to solve the problem”. Martin Knudsen (1933), transcription of a “Molecular flow of gases through tubes” lecture delivered in London.

molecular regime, which cannot be predicted using hydrodynamic equations. For β close to zero, fluid-wall collisions are the most predominant form of interaction, and the fluid accordingly approaches the free molecular regime ($Kn \sim \infty$). The first-order kinetic theory prediction of the Knudsen self-diffusivity in infinite planar channels is given by [Hiby and Pahl \(1952\)](#)

$$D_k = \sqrt{\frac{8kT}{\pi m}} \frac{R\sigma}{4} \left(\frac{3}{4} + \ln \frac{Kn}{\gamma} \right), \quad (3.10)$$

where $\gamma = e^C = 1.781$ and $C \approx 0.5772$ is the Euler-Mascheroni constant. In [Figure 3.6](#), the predictions given by [Eq. \(3.10\)](#) are the dash-dotted lines presented in the collisionless regime, for $Kn \gtrsim 10$. Note that [Eq. \(3.10\)](#) underpredicts the self-diffusivity when $Kn \lesssim 50$, with deviations larger than 5%, because intermolecular collisions are not properly considered in this range of Kn while still being relevant, i.e. this can be seen by closer inspection of [Figure 3.5](#), where $\beta \sim 0.1$ for these Knudsen numbers.

It is worth noticing that the Knudsen self-diffusivity, as predicted by [Eq. \(3.10\)](#), scales linearly with the confinement ratio R and shows a logarithmic divergence with respect to the Knudsen number. This self-diffusivity singular behaviour can be attributed to the slit geometry ([Arya et al., 2003](#)). Indeed, when Kn goes to infinity, there are a growing number of outlier molecules with zero (or sufficiently close to zero) x -velocity components (normal to the walls) that do not experience any collisions. Therefore, their contribution to the MSD grows linearly in time and eventually causes the self-diffusion coefficient to grow without any bound. The presence of this type of particle behaviour is likewise responsible for the mass flux divergence of a flow driven by a pressure gradient ([Cercignani & Daneri, 1963](#)).

Transition Regime (intermediate β values)

For intermediate β values, both fluid-fluid and fluid-wall collisions are relevant and must be considered. This situation corresponds to the more challenging transition regime, where self-diffusivities take a value in between the molecular and Knudsen results. From [Figure 3.5](#), we can roughly estimate that fluid-wall collisions can no longer be neglected at about $Kn \sim 0.1$, as they represent well above 10% of the total number of collisions.

The Bosanquet interpolating formula has been used in the past to deal with bulk and rarefied gases ([Pollard & Present, 1948](#)) inside cylindrical capillaries or porous media. In this work, we find that the Bosanquet formula is an acceptable model also for dense, confined fluids, and allows us to predict the self-diffusivity for these intermediate β values

$$\frac{1}{D_B} = \frac{1}{D_m} + \frac{1}{D_k}. \quad (3.11)$$

The rationale underlying the applicability of Eq. (3.11) is that in the diffusion process, particles perform a random walk composed of steps whose length follow the Poisson distribution, with mean equal to the particle collision frequency. In the transition regime, both fluid-fluid and fluid-wall collisions must be considered, and the corresponding collision frequencies sum up because this constitutes the mean of the sum of two independent Poisson distributions. As the self-diffusivity is proportional to the reciprocal of the collision frequency, Eq. (3.11) follows this tendency as well.

It is worth noticing that, by construction, the Bosanquet formula agrees exactly with the molecular self-diffusivity in the continuum regime, and with the Knudsen self-diffusivity in the free molecular one. However, using D_k from Eq. (3.10) within the Bosanquet formalism in Eq. (3.11) leads to self-diffusivity predictions in poor agreement with numerical results in the transition regime. This can be explained by the fact that the formal definition of Knudsen self-diffusivities encompass two very different effects, namely the logarithmic divergence due to the slit geometry and the increasing importance of fluid-wall collisions. In order to decouple these two effects and quantify the contribution of fluid-wall collisions (which is the only one that the Bosanquet formula may capture), the Knudsen self-diffusivity has to be defined in a different way, e.g. by phenomenologically extending the expression derived for a cylindrical capillary (Bonilla & Bhatia, 2011) to a planar channel configuration

$$D_k = \frac{R\sigma}{3} \sqrt{\frac{8kT}{\pi m}} a_1^*. \quad (3.12)$$

The factor $a_1^* = 4/5\pi$ is a fitting parameter², which was tuned to match the EDMD data within the early transition regime, in order to capture the initial deviations with respect to the continuum values. This approach leads to good predictions of the self-diffusivities across $0 \lesssim Kn \lesssim 10$ for most of the channel heights considered in our study, as it can be observed from solid lines in Figure 3.6.

More specifically, Eq. (3.11) provides fairly good predictions of the self-diffusivity except for tight confinement (i.e. $R \leq 5$), with a relative error below 10% — see the inset in Figure 3.6. The deviations for small confinement ratios R can be explained by the poor accuracy of the D_m prediction, as given by Eq. (3.8). Indeed, the continuum regime is never reached in tight channels because the Kn is still remarkably larger than zero when the freezing reduced density is reached.

2. “With four parameters I can fit an elephant, and with five I can make him wiggle his trunk”. John von Neumann to Enrico Fermi.

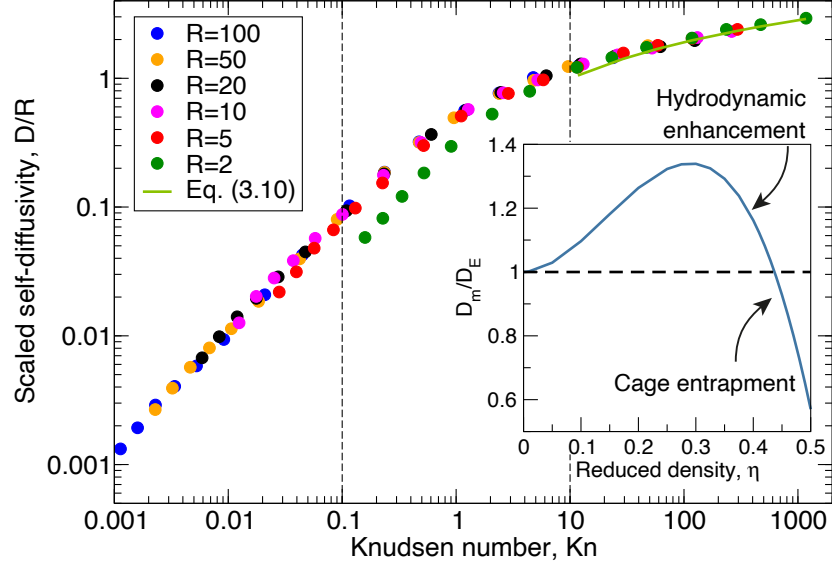


Figure 3.7: Scaling of all self-diffusivities by their R value, as a function of Kn for fully diffuse walls. The solid line at $Kn \geq 10$ is the free molecular approximation. Inset: non-linearity of molecular self-diffusivities in the continuum-based regimes (Erpenbeck & Wood, 1991).

3.3.4 Scaling of Self-Diffusivities with Confinement

From visual inspection of Figure 3.3a, it seems that self-diffusivities scale linearly with R , which would imply that D/R ratios are equivalent at a given Knudsen number, independently on the fluid rarefaction state and channel characteristic length. The collapse of self-diffusivities, which had already been suggested in previous studies (Mittal et al., 2006, 2007), may also be inferred from Figure 3.7, where we present the EDMD simulation results divided by the confinement ratio at which the simulations were performed. Despite the master curve (representing the scaled results for $R \geq 5$) looks particularly good on a log-log plot, it is needed to point out that the linear scaling of self-diffusivities with confinement does not actually hold true.

The functional form of Eq. (3.10) reveals that the linear relationship between D_k and R exists in the free molecular regime, but this is no longer the case in the continuum regime, where fluid-fluid collisions drive the diffusion process. Indeed, the Enskog self-diffusivity D_E , Eq. (3.9), depends linearly on the confinement ratio R , but the true molecular self-diffusivity D_m , Eq. (3.8), includes a correction factor that varies with the packing fraction η and, in turn, with the confinement ratio for equal Kn (as emphasised in the inset of Figure 3.7). More specifically, at intermediate packing fractions (up to $\eta \sim 0.3$), the self-diffusivity is larger than the prediction from Eq. (3.9) due to hydrodynamic enhancement consequences (Alder & Wainwright, 1967), whereas at

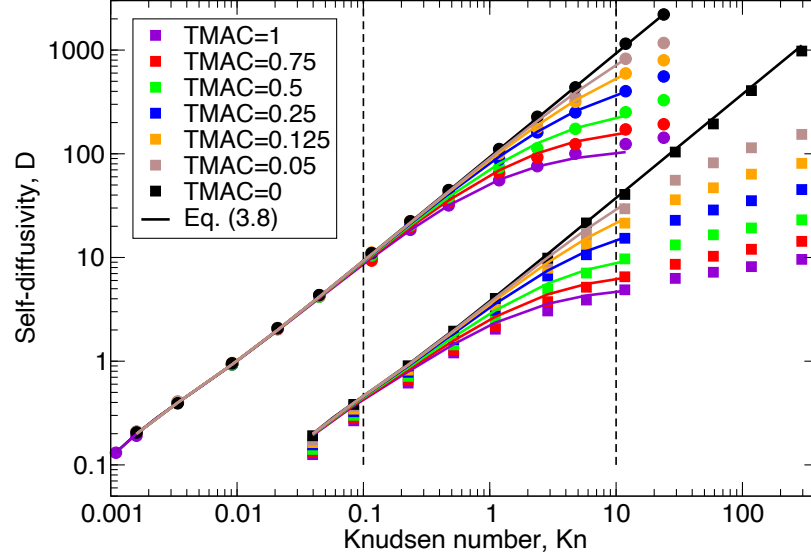


Figure 3.8: Self-diffusivities as a function of the wall microscopic roughness, in tight ($R = 5$, squares) and quasi-bulk ($R = 100$, circles) channels. Coloured solid lines represent the Bosanquet predictions, defining D_k as in Eq. (3.13).

higher reduced densities, the cage entrapment of particles comes into play causing the actual self-diffusivity to drop (Speedy, 1987). Since this property breaks down in the continuum regime, by extension the linear scaling with R cannot be considered as universal throughout the entire range of Kn .

Regardless, it is worth noticing that the linear scaling assumption may provide a rough estimate of the self-diffusivity, with deviations within 3% as long as the packing fraction is low enough, e.g. $\eta \lesssim 0.05$. Therefore, it is clear that this simplifying assumption is especially inaccurate for small R , i.e. in shale gas reservoir applications, where the continuum regime can only be reached at a very large fluid density.

3.3.5 Effect of TMAC on Self-Diffusivities

The wall roughness is anticipated to affect the self-diffusivity, especially for small β values (Krekelberg et al., 2011). In the Maxwell scattering kernel, the wall roughness is represented by the tangential momentum accommodation coefficient, i.e. from ideal perfectly smooth walls (TMAC = 0) to more realistic engineering walls (TMAC = 1). Simulations are performed at different TMACs = [0, 0.05, 0.125, 0.25, 0.5, 0.75, 1], and the resulting self-diffusivities are reported in Figure 3.8 as a function of Kn . Results are presented for two different cases, which are representative of loose ($R = 100$) and tight ($R = 5$) geometries.

When the fluid is loosely confined, diffusivity results for various TMACs collapse in the continuum regime ($Kn \leq 0.1$) as expected, whereas this is not the case in the tightly confined scenario. A close inspection of the results for continuum-like Kn reveals an increase in self-diffusivity with decreasing TMAC, which indicates that fluid-wall collisions remain important for low R values in this regime, and cannot be neglected. Note that when molecules are subjected to a specular reflection with the wall, there is no tangential momentum transfer, and so this represents the zero friction limit where the presence of walls is no longer felt by the fluid. Accordingly, the upper limit of self-diffusivities is associated with $\text{TMAC} = 0$.

As in [Section 3.3.3](#), here we also derive a semi-analytical formula for retrieving the self-diffusivities as a function of TMAC. Although the Maxwell scattering kernel is used in this study, one cannot expect to use the Smoluchowski prefactor ([Bhatia et al., 2011](#)) to rescale the Knudsen self-diffusivity D_k defined through [Eq. \(3.12\)](#). Indeed, the latter is just an ad hoc definition introduced to permit one to capture the crossover between molecular and Knudsen self-diffusivity using the Bosanquet formula.

A phenomenological approach is used here for extending the self-diffusivity predictions to the case of partial accommodation coefficients. More specifically, numerical experiments suggest that the following functional form for this prefactor is more appropriate to scale the Knudsen self-diffusivity ([Liang & Li, 2019](#))

$$D_k = \left(1 + f \frac{1 - \text{TMAC}}{\text{TMAC}}\right) D_k^{\text{TMAC}=1}, \quad (3.13)$$

where $f = 1.2261$ is a fitting parameter and $D_k^{\text{TMAC}=1}$ is the Knudsen diffusivity obtained for fully diffuse walls, as introduced in [Eq. \(3.12\)](#).

In [Figure 3.8](#), we show that [Eq. \(3.13\)](#) provides an accurate estimate of the self-diffusivity of a fluid confined within walls of different roughness, as a function of TMAC. For the loose confinement cases, where [Eq. \(3.8\)](#) accurately reproduces the diffusive dynamics in the continuum regime, the average relative error of the Bosanquet prediction is below 3.2% for the different accommodation coefficients in our assessment. For tighter geometries, where the influence of fluid-wall collisions is more notorious, the transition between molecular and Knudsen self-diffusivities is also successfully predicted at different TMAC values, when defining D_k as in [Eq. \(3.13\)](#).

Finally, it should be mentioned that [Eq. \(3.13\)](#) predicts an infinite Knudsen self-diffusivity for fully specular walls, i.e. $\text{TMAC} = 0$. For this case, $1/D_K = 0$ and this term can be neglected from [Eq. \(3.11\)](#), giving $D = D_m$ for all Knudsen numbers and confinement ratios. This prediction is represented by the black solid lines in [Figure 3.8](#), showing the maximum self-diffusivity at a given rarefaction state, i.e. bulk behaviour of the fluid with no confinement influence.

3.4 Conclusions

We have carried out a comprehensive and fundamental study of the self-diffusion process for a hard-sphere fluid confined between two parallel infinite walls, with data measured from EDMD simulations. Three dimensionless groups were adopted to characterise the self-diffusion process, namely the Knudsen number, the confinement ratio and the reduced density. The tangential momentum accommodation coefficient was used to define the roughness of the wall.

We found that the Bosanquet formula was able to provide a very satisfactory prediction of the self-diffusivity from the continuum to the early free molecular regime ($Kn \leq 10$), beyond moderately low confinements ($R > 5$) and from smooth to rough surfaces (all TMACs). Importantly, this work provides insights and predictions of self-diffusivity into the challenging transition regime, that was missing in the literature. A splitting procedure of the colliding particles has identified the interplay between the underpinning diffusive mechanisms, namely molecular and Knudsen diffusion for dense, confined fluids. Some deviations between the theory and the results for extremely tight geometries ($R \leq 5$) were observed, which can be explained by the inability of the fluid to show a continuum behaviour, i.e. fluid-wall collisions cannot be neglected even at densities close to the fluid freezing point, that corresponds to the smallest attainable Kn .

In summary, we can now predict self-diffusivity for dense hard-sphere fluids confined in two-dimensional slit geometries for any roughnesses, using Eq. (3.8), Eq. (3.9), Eq. (3.11), Eq. (3.12) and Eq. (3.13) for $0 < Kn \leq 10$ and Eq. (3.10) for $Kn > 10$. In the validation part of our study, we have analysed the suitability of using the widely established Einstein relation for describing the diffusion of strongly inhomogeneous fluids. Despite molecules traverse regions with different local densities, the MSD-based approach yields the same values as the Fickian benchmark model, and therefore the Einstein self-diffusivity is valid for predicting the diffusive flux even at the molecular scale.

Finally, we have also assessed previous work on the scaling of self-diffusivities with confinement. It was concluded that this relationship can only be considered approximately linear when the fluid is sufficiently rarefied ($\eta \leq 0.05$) or whether it is confined inside fully specular (frictionless) walls, none of them being appropriate for shale gas flows. This work lays the foundation to a more precise modelling of dense, confined flows for engineering applications, where there is an interplay between diffusive and convective processes, and to build on this for more realistic fluid and surfaces. As a matter of fact, the self-diffusivity results obtained in this work were later compared with methane gas results within realistic kerogen samples corresponding to a similar range of confinement ratios and Knudsen numbers (Alafnan, 2022), showing good quantitative agreement in general. This shows the capability of our simple, but robust, fluid-wall configuration to economically capture the true physics in more realistic configurations.

On the Knudsen Minimum Disappearance

N.B. This chapter has been published in: Corral-Casas, C., Li, J., Borg, M.K., Gibelli, L. “Knudsen minimum disappearance in molecular-confined flows”. *Journal of Fluid Mechanics* 945, A28 (2022).

It is well-known that the Poiseuille mass flow rate along microchannels shows a stationary point as the fluid density decreases, referred to as the Knudsen minimum. Surprisingly, if the flow characteristic length is comparable to the molecular size, the Knudsen minimum disappears, as reported for the first time by [L. Wu et al. \(2016\)](#). However, there is still no fundamental understanding why the mass flow rate monotonically increases throughout the entire range of flow regimes. Although diffusion is believed to dominate the fluid transport at the nanoscale, here we show that the Fick’s first law fails in capturing this behaviour, and so diffusion alone is insufficient to explain this confined flow phenomenon. Rather, we show that the Knudsen minimum disappears in tight confinements because the decay of the mass flow rate due to the decreasing density effects is overcome by the enhancing contribution to the flow provided by the fluid velocity slip at the wall.

4.1 Literature Survey

Fluids confined within geometries of molecular dimensions are commonly encountered in geological and biological systems ([Bocquet & Charlaix, 2010](#)), as well as in many engineering applications, e.g. membrane science ([Mistry et al., 2021](#)), that have been constantly growing in recent years — fostered by the technological progress in the fabrication of nanofluidic devices ([Kavokine et al., 2021](#)). In these flows, three significant length scales can be identified: the diameter of fluid constituent particles σ , the flow characteristic length, which is related to the channel diameter d , and the molecular mean free path (MFP) λ , which represents the average distance travelled by particles between two consecutive collisions. The interplay of phenomena occurring at these scales leads to complex fluid behaviour. Indeed, the continuum approach based on the

Navier-Stokes (NS) equations breaks down with increasing rarefaction ($\lambda \sim d$), since the local thermodynamic equilibrium condition is not fulfilled. Likewise, the standard kinetic theory description is no longer accurate at the nanoscale where dense ($\lambda \sim \sigma$) and confinement ($d \sim \sigma$) effects come into play, implying that the Boltzmann equation must be replaced by more complicated kinetic models, such as the Enskog equation (Kremer, 2010).

Despite the availability of computational procedures to describe the flow of confined fluids, the fundamental understanding of many phenomena occurring under tight confinement is still lacking. A notable example is that, for simple fluids, the Poiseuille mass flow rate (MFR) is found to monotonically increase in channels of molecular dimensions when the fluid density decreases, by using numerical solutions of the Enskog equation (L. Wu et al., 2016) and event-driven molecular dynamics simulations (Sheng et al., 2020). This behaviour is in sharp contrast with the long-standing recognition of flow mechanics in microchannels, which instead exhibits a non-monotonic variation of the MFR and the formation of a stationary point referred to as the Knudsen minimum (Cercignani & Sernagiotto, 1966; Pollard & Present, 1948; Tatsios et al., 2015), as long as the channel is sufficiently long and does not contain any bends (Ho et al., 2020).

A possible explanation of the Knudsen minimum disappearance is that the transport in dense fluids changes from convection to molecular diffusion under tight confinements, which already served as the foundation for the study presented in Chapter 3. Here, molecular diffusion is referred to as the diffusive mechanism which is driven by the interactions between fluid particles in the continuum limit ($\lambda \ll d$), and it is distinguished from the Knudsen diffusion phenomenon that takes place in the free molecular limit ($\lambda \gg d$), where particles only collide ballistically with the wall (Xiao & Wei, 1992). The dominance of diffusive transport at the nanoscale is known to take place for long alkanes in porous media, where the hydrodynamic description breaks down, although doubt remains for single-site gas molecules (Falk et al., 2015; Obliger et al., 2018). Despite there is no unequivocal evidence that this behaviour also occurs for non-tortuous channels, some hints supporting the diffusive nature of Poiseuille flow transport in tight geometries are provided by the analysis of velocity profiles. These are no longer parabolic as expected for force/pressure-driven flows, but show a plug-like behaviour instead, suggesting the predominance of diffusive mechanisms (Firouzi & Wilcox, 2013). However, a conclusive proof regarding a crossover from convection to molecular diffusion in these systems, that is triggered by the fluid confinement, has still not been given.

The aim of this chapter is to perform a detailed investigation of the Knudsen minimum disappearance in straight nanochannels, and elucidate the underpinning physical reasons. There are two main findings. First, despite the molecular-like confinements, we show that diffusion does not dominate transport, and so the convective flow contribution cannot

be neglected outside the free molecular regime. Second, we show that the monotonic increase of MFR can be attributed to the larger relative importance of the velocity slip at the wall, compared to the other physical mechanisms that are normal contenders at the microscale. The rest of the chapter is organised as follows. In [Section 4.2](#) we outline the simulation approach used to numerically study the transport process, as well as the theoretical formulation for predicting the flow of fluids using the Navier-Stokes equations. In [Section 4.3.1](#) we show that the Knudsen minimum vanishing in straight nanochannels cannot be attributed to diffusive processes, whereas in [Section 4.3.2](#) we prove that the contribution of the fluid slippage at the confining solid surface provides a satisfactory explanation of this recently discovered feature. A summary of the main results and conclusions follow in [Section 4.4](#).

4.2 Methodology

4.2.1 Simulation Setup and Problem Formulation

We consider force-driven Poiseuille flows inside a long tubular geometry with diameter d , where the fluid is modelled using a system composed of hard-sphere particles with molecular diameter σ . The wall is assumed to be a structureless cylindrical surface and the fluid-wall interactions are described by the Maxwell scattering kernel with full tangential momentum accommodation coefficient, where impinging particles are diffusely reflected after being thermalised with the wall. A comprehensive overview of the EDMD algorithm can be found in [Section 2.5](#), whereas more information on the simulation setup is presented in [Corral-Casas et al. \(2021\)](#).

Three dimensionless groups can be identified to systematically describe the different transport processes that may take place in this system, namely the reduced density, the confinement ratio, and the Knudsen number. The reduced density $\eta = n\pi\sigma^3/6$, where n is the number density, represents the number of fluid particles in the theoretical volume occupied by one hard-sphere. This first dimensionless group defines the degree of fluid rarefaction, allowing to differentiate between dense (large η values) and rarefied (low η values) gas flows. The confinement ratio $R = d/\sigma$ provides information about the degree of fluid inhomogeneity that arises because of the presence of walls, where tight confinements (low R values) are associated with an increase of the collision frequency of fluid particles with the wall. Finally, the Knudsen number $Kn = \lambda/(d - \sigma)$ quantifies the departure of the fluid from its local quasi-equilibrium case. The continuum approach can be used for $Kn \lesssim 0.01$, while non-equilibrium effects come progressively into play in the following three regimes: slip ($0.01 < Kn \lesssim 0.1$, where the continuum model still holds but different boundary conditions are needed to capture the “slippage” of fluid particles at the solid surface), transition ($0.1 < Kn \lesssim 10$, where the continuum

description breaks down and kinetic equations must be used instead), and free molecular ($Kn > 10$, where molecules move ballistically between collisions with the confining wall). The expression of the MFP, derived from kinetic theory, is given by (Kremer, 2010)

$$\lambda = \frac{16}{5\pi} \frac{\mu}{P} \sqrt{\frac{\pi kT}{2m}}, \quad (4.1)$$

where m is the molecular mass and P is the pressure, related to the density through $P = nkTZ$, in which k is the Boltzmann constant, T the temperature of the system, and Z is the fluid compressibility factor that can be accurately approximated by the equation of state in Eq. (2.2). According to the Enskog theory, the shear viscosity μ of a hard-sphere fluid is given by

$$\mu = \frac{5}{16\sigma^2} \sqrt{\frac{mkT}{\pi}} \mu_f = \frac{5}{16\sigma^2} \sqrt{\frac{mkT}{\pi}} \frac{1}{\chi} \left[1 + \frac{16}{5} \eta \chi + \frac{64}{25} \left(1 + \frac{12}{\pi} \right) \eta^2 \chi^2 \right], \quad (4.2)$$

where μ_f is the dense gas correction for the viscosity of a rarefied gas, and χ represents the contact value of the pair correlation function in a hard-sphere fluid in uniform equilibrium, which from the aforementioned equation of state reads

$$\chi = \frac{1}{nb} \left(\frac{P}{nkT} - 1 \right) = \frac{1}{2} \frac{2 - \eta}{(1 - \eta)^3}, \quad (4.3)$$

where $b = 2\pi\sigma^3/3$ is the second virial coefficient (Kremer, 2010). Only two out of the three dimensionless groups are independent, as they are interrelated through the Knudsen number

$$Kn = \frac{\lambda(\eta)}{d - \sigma} = \frac{\mu_f(\eta)}{6\sqrt{2}\eta Z(\eta)R}. \quad (4.4)$$

4.2.2 Flow Analytical Solutions. Hagen-Poiseuille Equations.

The Navier-Stokes equations (in cylindrical coordinates) for the incompressible flow of a Newtonian fluid through an infinite tubular channel simplify to

$$\frac{1}{r} \frac{\partial}{\partial r} \left(r \frac{\partial u_z}{\partial r} \right) = \frac{1}{\mu} \frac{dP}{dz}, \quad (4.5)$$

where u_z is the fluid macroscopic velocity in the streamwise direction, and r is the radial direction. The first-order slip at the wall, $r = d/2$, can be written as

$$u_s = -\alpha \lambda \left. \frac{\partial u_z}{\partial r} \right|_{r=d/2}, \quad (4.6)$$

where u_s is the slip velocity, and $\alpha = 2/\sqrt{\pi}$ is the velocity slip coefficient (Lei et al., 2016). The straightforward solution of the boundary value problem comprising Eq. (4.5) and Eq. (4.6) reads

$$u_z(r) = \frac{1}{4\mu} \frac{dP}{dz} \left(r^2 - d\alpha\lambda - \frac{d^2}{4} \right). \quad (4.7)$$

The spatial integration of the velocity field over the circular cross section yields the Hagen-Poiseuille solution for the MFR

$$\dot{m}_h = mn \int_0^{d/2} u_z(r) 2\pi r dr = -\frac{mn\pi d^4}{128\mu} \frac{dP}{dz} (1 + 8\alpha Kn). \quad (4.8)$$

The dimensionless MFR in the continuum limit, $Kn \approx 0$, can be obtained from Eq. (4.8) by setting $\alpha = 0$, namely the non-slip solution, and $\eta_0 = 0.494$, i.e. the freezing density of a hard-sphere fluid (Sigurgeirsson & Heyes, 2003)

$$\frac{\dot{m}_h}{\dot{m}_n} = \frac{3R\eta_0}{5\sqrt{\pi}\mu_f(\eta_0)}, \quad (4.9)$$

where \dot{m}_n is a normalising factor for the mass flow rate defined as

$$\dot{m}_n = -mn_0 \frac{\pi d^2}{4} \frac{1}{m} \frac{1}{n_0} \frac{dP}{dz} \frac{d}{\sqrt{kT/m}} = -\frac{\pi d^3}{4\sqrt{kT/m}} \frac{dP}{dz}. \quad (4.10)$$

4.3 Results and Discussion

4.3.1 Knudsen Minimum Vanishing. Diffusion-Based Analysis

The Knudsen minimum disappearance, which was initially presented for the slit geometry in L. Wu et al. (2016), is demonstrated for a cylindrical pipe in this work, where it is seen to occur between $R = 20$ and $R = 8$ in Figure 4.1a. Here, we show transport results from non-equilibrium EDMD simulations that are performed in the presence of an external unidirectional force per molecule F along the axis of the channel, whose value is assumed to be sufficiently low so that the flow remains in the linear response regime — the artificial addition of heat is adequately dissipated by the wall. The numerical evaluation of the MFR for each case, depending on η and R , is obtained from a spatial integration of local densities and velocities.

As mentioned in Section 4.1, the Knudsen minimum vanishing might be explained by supposing that, under molecular confinements, a crossover from convective to diffusive transport takes place up to the late transition regime ($Kn \lesssim 10$). This hypothesis is tested by comparing the actual MFR (from EDMD simulations) with the analytical estimate assuming that the transport is solely driven by diffusion, which is based on the

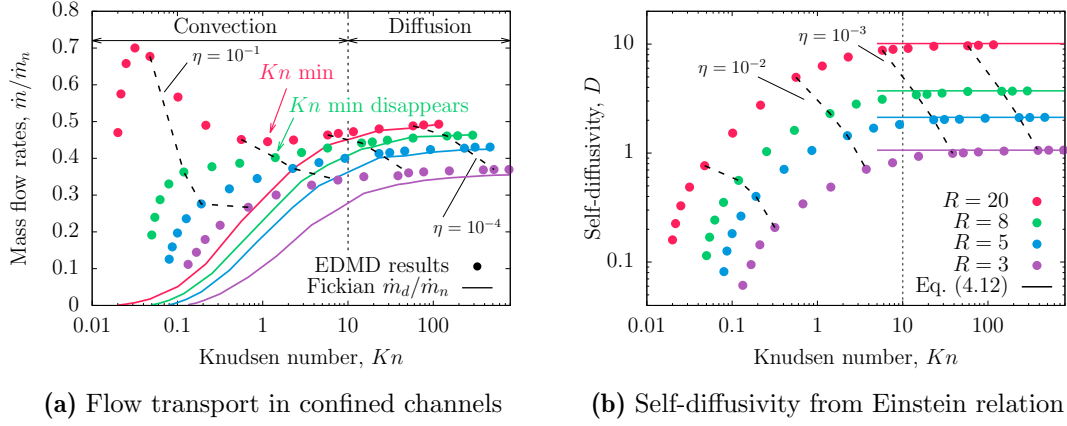


Figure 4.1: (a) Comparison between the dimensionless MFR provided by non-equilibrium simulations (symbols) and the theoretical predictions assuming Fickian diffusion, as given by Eq. (4.11) (lines). There is good agreement in the free molecular regime ($Kn \geq 10$), whilst Fick's law underestimates MFR elsewhere, which implies that convective transport terms cannot be neglected at any confinement. The normalising factor of the mass flow rate \dot{m}_n is presented in Eq. (4.10). (b) Dependence of the self-diffusivity D on the Knudsen number Kn and the confinement ratio R . Horizontal lines represent the theoretical value of the Knudsen self-diffusivity from Eq. (4.12) for each R .

Fick's first law where the MFR of diffusing particles \dot{m}_d follows a linear response with the density gradient along the axial z -direction dn/dz

$$\dot{m}_d = -\frac{\pi d^2}{4} m D \frac{dn}{dz} = -\frac{D \pi d^2 m}{4 k T \left(Z + \eta \frac{dZ}{d\eta} \right)} \frac{dP}{dz}, \quad (4.11)$$

in which D is the self-diffusion coefficient. Note that the number density n and pressure P are interconnected using Eq. (2.2), with the pressure gradient being identified with the force F through the fundamental relation given by $-dP/dz = nF$.

However, before comparing the MFR simulation results with the predictions given by Eq. (4.11), self-diffusion results D are needed as this information is unavailable in the literature for the cylindrical geometry under confinement. Therefore, a set of equilibrium EDMD simulations is carried out, see details in Chapter 3, where the self-diffusion coefficients are determined by means of the Einstein relation in the entire range of flow regimes, for different confinement ratios of interest. These simulation results are shown in Figure 4.1b, where it can be seen that, from a qualitative standpoint, self-diffusivities increase with Knudsen number because the MFP becomes larger and therefore particles have more mobility before colliding with another entity in the system. At the same time, self-diffusivities increase with the flow characteristic length for a given Kn , as large R values imply less collisions with the diffuse wall model that hinder the molecular displacement in the streamwise direction. Note that in the free molecular limit, where

there are just diffuse collisions with the wall, numerical results perfectly agree with the analytical Knudsen self-diffusivity prediction from kinetic theory (Xiao & Wei, 1992)

$$D_k = \frac{(d - \sigma)}{3} \sqrt{\frac{8kT}{\pi m}}, \quad (4.12)$$

where it has been accounted for the fact that the effective transversal space accessible to the centre of molecules is $d - \sigma$, that is, the flow characteristic length. The dimensionless MFR in the free molecular limit ($Kn \sim \infty$) is provided by the equation for diffusive transport, Eq. (4.11), with the Knudsen self-diffusivity from Eq. (4.12) as the proportionality factor, $Z = 1$, and using the normalisation from Eq. (4.10)

$$\frac{\dot{m}_d}{\dot{m}_n} = \frac{D_k}{d} \sqrt{\frac{m}{kT}} = \frac{2}{3} \sqrt{\frac{2}{\pi}} \left(1 - \frac{1}{R}\right). \quad (4.13)$$

As presented in Figure 4.1a, it is found that the Fick's first law unsurprisingly reproduces the MFR simulation results very well in the free molecular regime. The slight disagreement in the tightest of confinements (for $R = 3$) can be attributed to the transition from Fickian to anomalous diffusion (e.g. of single-file type) as particles cannot overtake each other when moving along the channel. However, it is evident that Eq. (4.11) underestimates the mass transport along the remaining flow regimes ($Kn \lesssim 10$), and therefore the governing mechanism in this range of Kn is no longer purely diffusive. This clearly proves that, in straight channels, the supposed crossover from convection to diffusion does not occur even under tight confinements and, consequently, cannot explain the Knudsen minimum disappearance. Note that these results do not imply that diffusion is not the governing transport mechanism within more complex geometries, such as in nanoporous media, which will need to be addressed separately.

4.3.2 Knudsen Minimum Vanishing. Slip-Based Analysis

As discussed so far, there are a number of mechanisms that influence the MFR through a channel, and so the best explanation for describing the features of the MFR dynamics can be inferred in the limits of the continuum ($Kn \approx 0$) and free molecular ($Kn \sim \infty$) regimes, as we illustrate in Figure 4.2a. As suggested by the analysis from Section 4.3.1, the fluid flow is convective in nature in the hydrodynamic regime, regardless of R . When moving towards the free molecular regime (i.e. decreasing density values), the MFR initially increases as the viscosity decreases, implying that the fluid velocity arising as a response to a given external driving force will be larger. By contrast, the fluid flow

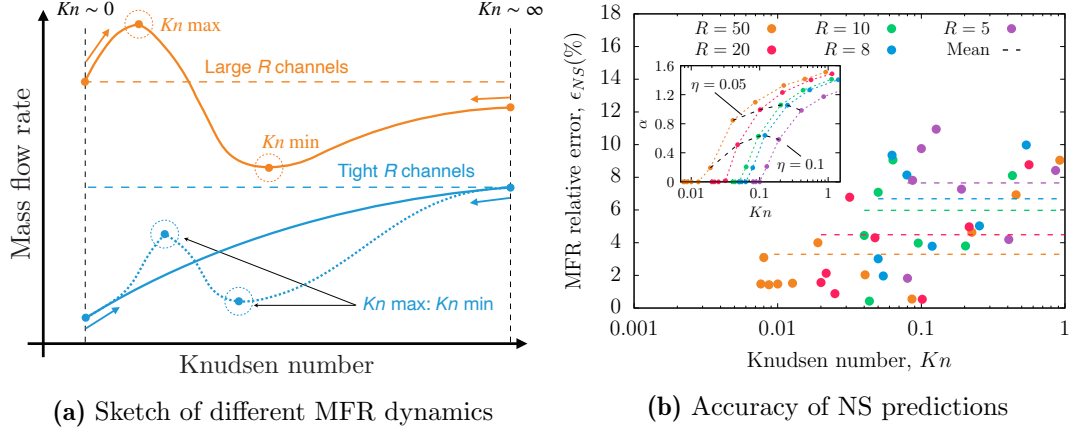


Figure 4.2: (a) Qualitative analysis of the dimensionless MFR curves against the Knudsen number. In sufficiently *large* channels (orange colour), where the continuum transport is larger than the free molecular one, the MFR curve develops two stationary points. In tighter confinements (blue colour), where the free molecular flow is larger than the continuum one, the MFR curve could either show the two stationary points or follow a monotonic increase instead, where the Knudsen minimum disappears. (b) Relative percentage error of the MFR predicted by the Navier-Stokes equations with slip, for different confinement ratios. Dashed horizontal lines are the average percentage error over the displayed range of Kn : the mean error is within 8% for the tighter $R = 5$, whereas it reduces to less than 4% for the largest $R = 50$ considered here. The inset shows the slip coefficients determined from EDMD simulations, for different R and η values, obtained by fitting the quadratic velocity profiles.

is driven by Knudsen diffusion in the free molecular regime. This means that, when moving back towards the continuum regime (i.e. increasing density values), the MFR decreases as the molecular MFP shortens, implying lower self-diffusivities as observed in Figure 4.1b.

Under a sufficiently loose confinement, the Knudsen minimum existence follows from these two limiting behaviours. As the MFR in the continuum limit is always larger than that in the free molecular one, the MFR curve must show two stationary points as depicted by the orange curve in Figure 4.2a, namely the Knudsen maximum and the Knudsen minimum. Therefore, a sufficient condition for the Knudsen minimum to show up easily follows from the condition that the MFR in the continuum limit, given by Eq. (4.9), is larger than that in the free molecular regime, given by Eq. (4.13), from where it turns out that $R \gtrsim 60$. On the other hand, if the confinement is tighter, the continuum MFR is lower than the free molecular one. Accordingly, the flow transport curve may either form two stationary points, given by the blue dotted line, or else could show a monotonic increase throughout the entire range of Knudsen numbers, as represented by the blue solid line.

It is then clear that, for the confined case, a necessary and sufficient condition for the Knudsen minimum to appear is that the Knudsen maximum shows up as well. Indeed, the first derivative is positive in the continuum regime but, by definition, it is negative in the left neighbourhood of the local minimum. Therefore, before this local minimum, there must necessarily be a point at which the first derivative changes from positive to negative, which corresponds to a local maximum. Consequently, proving the disappearance of the Knudsen minimum is equivalent to demonstrating the Knudsen maximum vanishing. The latter question is easier to address as this local maximum falls in the continuum/slip regime ($Kn \lesssim 0.1$), see [Figure 2.3](#), where it can be tackled analytically using the Navier-Stokes equations with the first-order velocity slip boundary condition, which in its dimensionless form reads (its derivation has been carried out in [Section 4.2.2](#))

$$\dot{m} = \frac{\dot{m}_h}{\dot{m}_n} = \frac{3R\eta}{5\sqrt{\pi}\mu_f} (1 + 8\alpha Kn). \quad (4.14)$$

Note that the velocity slip boundary condition at the wall used to derive [Eq. \(4.14\)](#) is based on the strain rate and not on the stress tensor, leading to less accurate results if the wall is not at rest ([Lockerby et al., 2004](#)). The validity of [Eq. \(4.14\)](#) in the considered range of Kn is tested in [Figure 4.2b](#), where we show the relative error with respect to the EDMD results presented in [Figure 4.1a](#). It is clear that, despite the tight confinements, the evaluation of the Navier-Stokes equations with the numerical slip coefficients α presented in the inset of [Figure 4.2b](#) predict the MFR very accurately. In the following analysis, the slip coefficient α is assumed to be constant and equal to that of a rarefied gas, albeit the slip phenomenon is known to be more complicated when dealing with liquid-like densities, and the standard kinetic theory treatment is no longer applicable ([Hadjiconstantinou, 2021](#); [Martini et al., 2008](#); [Shan et al., 2022](#)). This fact is also reflected in the inset of [Figure 4.2b](#), where the non-trivial dependence of α on both the confinement ratio R and the reduced density η can be observed. The validity of this assumption will be discussed later in this chapter.

[Eq. \(4.14\)](#) clearly shows that, at constant R , there are three physical terms contributing to the MFR, namely the viscosity (i.e. via μ_f), the density (i.e. via η), and the slip (i.e. via $1 + 8\alpha Kn$). These terms vary with the reduced density but, for the following analysis, we find it more convenient to study the MFR with respect to the reduced specific volume $\nu = 1/\eta$, as in this way there is a one-to-one direct correspondence between ν and Kn . It should be stressed that this choice does not limit the generality of the conclusions. The relative importance of these terms can be singled out by evaluating their corresponding partial rates of change

$$\frac{d\dot{m}}{d\nu} = \frac{d\eta}{d\nu} \left(\frac{\partial \dot{m}}{\partial \mu_f} \frac{d\mu_f}{d\eta} + \frac{\partial \dot{m}}{\partial \eta} + \frac{\partial \dot{m}}{\partial Kn} \frac{dKn}{d\eta} \right) = \frac{1}{\nu^2} (Q_\mu + Q_\eta + Q_\alpha), \quad (4.15)$$

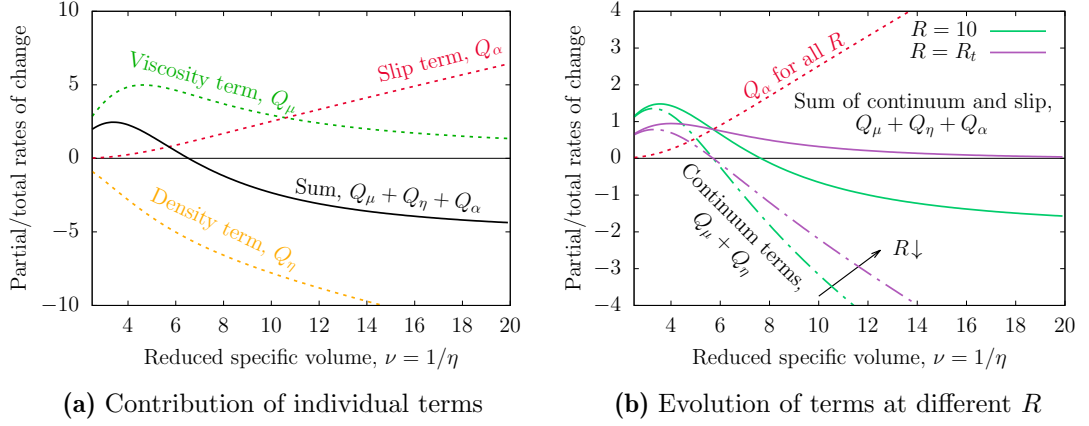


Figure 4.3: (a) Partial rates of change against the reduced specific volume, for $R = 20$, under the continuum framework of fluid modelling, which capture how flow transport is affected by a change of each of the underlying contributions. (b) Interplay between the continuum (dash-dotted) and the slip (dotted) contributions for different R . For sufficiently large R values, the continuum contribution dominates and the sum of all rates of change (solid) cross the x -axis, i.e. the Knudsen maximum appears. However, for tight channels, the continuum contribution is less relevant whereas slip remains the same, driving the overall rate of change to be positive throughout the entire range of ν values, with the Knudsen maximum disappearing as a consequence.

where

$$Q_\mu = \frac{3R\eta(1 + 8\alpha Kn)}{5\sqrt{\pi}\mu_f^2} \frac{d\mu_f}{d\eta}, \quad (4.16)$$

$$Q_\eta = -\frac{3R(1 + 8\alpha Kn)}{5\sqrt{\pi}\mu_f}, \quad (4.17)$$

$$Q_\alpha = \frac{24R\eta\alpha}{5\sqrt{\pi}\mu_f} \frac{dKn}{d\eta}. \quad (4.18)$$

These individual contributions are presented in Figure 4.3a for $R = 20$, in a range of ν values corresponding to $Kn \lesssim 0.1$, namely the slip regime. Here, the plot of Eq. (4.16) shows that the partial derivative of the MFR with respect to the viscosity, Q_μ , is always positive with increasing reduced specific volume. In particular, the rate of change is higher for low ν values, whereas its value decreases for large reduced specific volumes — showing that the viscous contribution to the overall flow is no longer the preferential one when non-equilibrium effects kick in. Eq. (4.17) shows that the MFR partial derivative with respect to the density, Q_η , is always negative with increasing reduced specific volume. If the slip contribution is temporarily disregarded, the density is seen to become relevant over the viscosity at $\nu \approx 6$, and drives the MFR to decrease monotonically with further increase in the reduced specific volume. Eq. (4.18) shows that the MFR

partial derivative with respect to the slip, Q_α , is always positive with increasing specific volume. In particular, the rate of change is almost negligible in the continuum regime while it becomes larger in the slip regime ($\nu \gtrsim 3.33$), where rarefaction effects become more prominent and the fluid slippage at the wall increasingly contributes to the overall MFR.

Three important observations are in order and presented in Figure 4.3b, that helped us to understand why the Knudsen minimum disappears only when confinements are tight. The first remark is that the viscosity and density contributions exactly counterbalance at the same ν regardless of R . This can be easily proved using Eq. (4.16) and Eq. (4.17), and it is clearly shown by dashed lines, representing the sum of viscosity and density rates of change (dubbed the *continuum contribution* from here onwards), which always crosses the x -axis at $\nu = 5.711$. A second remark is that the magnitude of the rate of change of the continuum contribution reduces with tighter channels and so its absolute value decreases with lower R for a given ν value, as could also be deduced from Eq. (4.16) and Eq. (4.17). The third remark is that the slip contribution (dotted line) is independent of R , as it is seen in Eq. (4.18), and so its relative importance grows when the confinement ratio reduces.

The interplay between the three aforementioned contributions (denoted by solid lines in Figure 4.3b, representing the sum of continuum and slip terms) significantly depends on the size of the channel, and we can mainly distinguish between two types of flow behaviours. For *large* channel sizes and starting from the continuum regime (low ν), the viscosity contribution initially dominates and leads the MFR to increase with ν . The region corresponding to low ν values can then be referred to as viscosity dominated since this contribution overcomes that of density, and here the slip term is negligible. Unlike the viscosity term that gets weaker as the fluid rarefaction increases, the density term becomes progressively more important and causes the Knudsen maximum to form by eventually driving the MFR to decrease.

For tight confinements, viscosity is initially dominant and drives the MFR increase as in the previous case. However, now there is an interplay between density and slip in the region where the transport was previously density dominated, as the relative contribution of slip becomes more and more important for decreasing R . Indeed, as emphasised by the magnitude of the continuum and slip contributions in Figure 4.3b, there might be a threshold confinement ratio R at which the latter overcomes the former, preventing the formation of the expected Knudsen maximum. Therefore, the velocity slip at the boundary impels the MFR curve to monotonically increase throughout the entire range of flow regimes, with the Knudsen maximum (and so, the Knudsen minimum) disappearing as a consequence.

It is worth noticing that, within the simplified solution represented by Eq. (4.15), the Knudsen minimum disappearance can be determined by a simple argument. As the rate of change of the MFR is a continuous function that takes positive values in the continuum limit, a sufficient condition for the MFR to cross the x -axis could be defined by the Bolzano theorem

$$\lim_{\nu \rightarrow \infty} (Q_\mu + Q_\eta + Q_\alpha) = \frac{8\sqrt{2}\alpha - 3R}{5\sqrt{\pi}} \leq 0, \quad (4.19)$$

from where the threshold value of the confinement ratio for the Knudsen minimum disappearance is $R_t < 8\sqrt{2}\alpha/3 \approx 4.3$. The numerical results presented in Figure 4.1a show that the MFR monotonically increases with rarefaction up to about $R \approx 8$, and so the theoretical estimate from Eq. (4.19) only provides a sufficient condition, but not necessary, for the Knudsen minimum disappearance.

As a concluding remark, it is worth to be noticed that the analysis carried out in this section is based on two main simplifying considerations. The first assumption consists on using nominal values for density and viscosity in the Navier-Stokes equations to predict the MFR values, despite it is well-known that, under tight confinement, density is non-uniform across the channel and viscosity is no longer a local property of the position along the channel (Travis et al., 1997). However, there is a large body of evidence demonstrating that the hydrodynamic framework is valid down to nanoscale confinements (Bocquet & Charlaix, 2010), and indeed our numerical simulations in tight geometries also showed an agreement with the theoretical prediction provided by the Hagen-Poiseuille solution with slip, Eq. (4.14), using nominal values of the fluid properties — as it is presented in Figure 4.2b.

The second assumption involves the use of a constant slip coefficient although, unlike the rarefied case, numerical evidence shows that it depends on the channel size and on the fluid density — see the inset within Figure 4.2b. However, the validity of the presented analysis can be straightforwardly extended when a more accurate expression of the slip coefficient is used. As an example, a universal scaling law is derived for the slip coefficient in a planar geometry by Shan et al. (2022), and it is shown that α varies significantly with η , whereas the dependence on R can be neglected. Accordingly, the slip contribution is still independent of R and the continuum contributions remain linear functions of R , counterbalancing each other at a specific η value regardless of the confinement ratio. Therefore, although the curves corresponding to these contributions are different from the ones depicted in Figure 4.3b, there still must exist a threshold confinement ratio for which the Knudsen minimum disappears as, when R is small enough, the decay of the mass flow rate due to the density decreasing is overcome by the enhancing contribution of the slip.

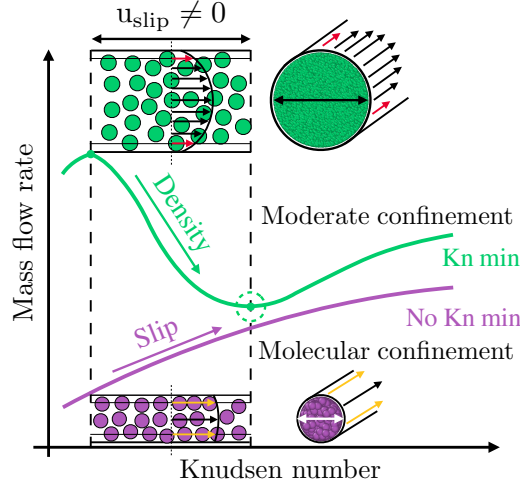


Figure 4.4: Graphical abstract showing the main findings of this piece of work.

4.4 Conclusions

We have studied the Knudsen minimum disappearance that occurs for Poiseuille flows in tight cylindrical geometries. High-fidelity EDMD simulations have been carried out in a wide range of reduced fluid densities η and channel confinement ratios R , in both equilibrium (to obtain the self-diffusivities needed in the Fickian framework) and non-equilibrium (directly evaluating the mass flow rate) setups. Although diffusion is supposed to be the main transport mechanism at the nanoscale, we found that the convective contribution to the mass flow rate cannot be disregarded — even under confinements of molecular dimensions. This convection-dominated transport, which is analytically studied using the Hagen-Poiseuille solution with first-order slip, is decoupled into its three fundamental contributions, namely viscosity, density, and slip.

The individual influence of each of them on transport is assessed for different fluid rarefaction states and confinement ratios, which revealed that the disappearance of the Knudsen minimum is a consequence of the interplay between these contributions. More specifically, the combined contribution of viscosity and density weakens in tight geometries, whereas the slip term remains the same when R decreases, and so its relative importance increases in this context. Therefore, the Knudsen minimum vanishing under tight confinement can be explained by the more accentuated importance of the fluid slippage at the wall. These results are graphically summarised in Figure 4.4. The relevance of this work underpins in its qualitative explanation of dense flow mechanisms at the molecular scale, which may help to better understand how slip, from a fundamental standpoint, affects the flow of dense gases/liquids confined within tight geometries, such as the high-pressure methane transport in unconventional shale rocks (Zhang et al., 2019) or water transport in nano-structured filtration membranes (Falk et al., 2010).

Fluid Velocity Slip at the Nanoscale

N.B. This chapter has been submitted in a manuscript to *Physical Review Fluids*, where is currently under review: Corral-Casas, C., Chen, Y., Borg, M.K., Gibelli, L. “Density and Confinement Effects on Fluid Velocity Slip”.

Understanding the velocity slip of fluids in channels of molecular length-scales is essential for accurately manipulating their flow in engineering applications, such as in water desalination or, by reversing the process, osmotic power generation. This study addresses two major open questions, namely (a) the range of validity of the Navier-Stokes equations with slip boundary conditions in describing fluid flows within channels of molecular confinement, and (b) the effect of fluid density and confinement, as well as surface properties, such as microscopic roughness and curvature, on fluid slippage along walls. The results show that the well-known criterion for the slip solution, which is valid in rarefied conditions, also holds for a dense gas, i.e., for Knudsen numbers $Kn \lesssim 0.1$. We also find that the key quantity influencing the friction coefficient of a fluid is the peak density at the walls, rather than the nominal density, the fluid confinement or the channel curvature, as found in previous studies. In particular, higher nominal densities lead to higher density peaks, and therefore a decrease in slip, while tighter confinements lead to lower density peaks, and therefore an increase in slip, regardless of channel geometry. Furthermore, the velocity slip depends on the microscopic roughness via the Smoluchowski factor.

5.1 Literature Survey

The study of isothermal gas flows in small channels has been instrumental in the development of micro-electro-mechanical devices (MEMS) ([Gad-el Hak, 1999](#)). In these systems, gases flow through channels that are only a few micrometres wide, so that the mean free path λ , or the average distance between collisions for gas molecules, approaches the same order of the flow characteristic length of the channel, L . As a result, gas particles tend to collide with the walls of the system rather than with other particles, which means that they deviate from the quasi-local thermodynamic

equilibrium assumption of continuum fluid dynamics (Kremer, 2010) — the degree of non-equilibrium being quantified by the Knudsen number, $Kn = \lambda/L$. The Boltzmann equation provides an accurate description of these dilute gas flows over the whole range of Kn , but for slight non-equilibrium conditions, where $Kn \lesssim 0.1$, its asymptotic solution shows that the Navier-Stokes equations can also be applied (Hadjiconstantinou, 2006), provided that the gas is allowed to slip along the surface. The velocity slip at the wall is typically expressed as the product of the slip length times the velocity gradient normal to the wall, where the former is simply proportional to the mean free path by a constant factor known as the slip coefficient (Kennard, 1938), see e.g. Eq. (4.6).

Recent advances in technology have led to a shift in focus from the microscale to the nanoscale (Kavokine et al., 2021; Sparreboom et al., 2010). In nanoscale engineering applications, the flow characteristic length becomes similar to the diameter of the fluid particles σ , which has significant implications, such as the fact that the quasi-local thermodynamic equilibrium assumption may not hold even at relatively high fluid densities. Under these conditions, the behaviour of the fluid becomes dependent on the complex interplay between dense effects ($\lambda \sim \sigma$) and tight geometries ($L \sim \sigma$), which leads to spatial inhomogeneities with preferential ordering in the density profile near the boundaries (Israelachvili, 2011), as well as a material depletion in the central homogeneous region when compared to the nominal density (G. J. Wang & Hadjiconstantinou, 2015). A notable example of the unexpected fluid behaviour that occurs within channels of molecular confinement is that the pressure-driven mass flow rate is found to increase monotonically with decreasing fluid density (Corral-Casas et al., 2022; L. Wu et al., 2016), rather than forming a minimum as it does for dilute gas flows (Cercignani & Daneri, 1963; Pollard & Present, 1948).

While molecular-based approaches, such as the Enskog equation and Molecular Dynamics (MD) simulations, have the potential to capture the physics of fluids at the nanoscale (Sheng et al., 2020), their computational requirements are significant due to the complexity of the collision integral of the former and the high cost of multi-body force calculations of the latter. Therefore, extensive experimental (Holt et al., 2006; Majumder et al., 2005; Whitby et al., 2008) and numerical (Hummer et al., 2001; Skoulidas et al., 2002; Thomas & McGaughey, 2008b) studies have been carried out to investigate whether the framework of continuum fluid dynamics can be extended down to the nanoscale. It has been found that, when the fluid confinement is very tight ($L/\sigma \lesssim 10$), the fluid structuring extends throughout the entire channel, making the continuum approximation inapplicable. In such extreme conditions, a hydrodynamic-like approach is still possible, but requires the transport coefficients to be spatially dependent and even non-local if the channel is only a few molecular diameters in size (Bitsanis et al., 1988; Travis et al., 1997). On the other hand, if the fluid confinement is relatively moderate

($L/\sigma \gtrsim 10$), the conventional Navier-Stokes equations with slip boundary conditions may be valid for some fluid densities. However, the bulk viscosity must be used (Din & Michaelides, 1997) and the slip length turns out to depend in a highly non-trivial way on both the fluid state and the wall. For example, the slip length is affected by the fluid structure induced in the directions parallel to the walls (Thompson & Robbins, 1990) and, beyond a threshold, becomes a non-linear function of the strain rate at the wall (Thompson & Troian, 1997). Wetting phenomena (Barrat & Bocquet, 1999), the hydrophobic and hydrophilic nature of walls (Sendner et al., 2009), and surface macroscopic roughness (Priezjev & Troian, 2006) have also been found to play a role. Over the years, several models have been developed to describe the slip length from a molecular perspective, including the variable density Frenkel-Kontorova model (Lichter et al., 2004; Martini et al., 2008) and expressions based on the so-called molecular kinetic theory (F. C. Wang & Zhao, 2011; G. J. Wang & Hadjiconstantinou, 2019), among a myriad of other derivations (Hadjiconstantinou, 2021; Hadjiconstantinou & Swisher, 2022; Priezjev, 2007).

In this work we aim to address two fundamental questions about molecular-confined fluids that remain elusive despite extensive research: (a) to formulate a quantitative validity criterion for the solution of the Navier-Stokes equations with slip boundary conditions, and (b) to determine the dependence of the fluid slippage on the density and confinement of the fluid, as well as on the surface curvature and microscopic roughness. The first question has not been examined in the literature and it is uncertain whether the criterion established for dilute gases at the microscale, based on the Knudsen number, is applicable to dense, nanoscale-confined fluids. The second question is crucial for resolving the existing confusion, as results from studies on planar and cylindrical geometries are inconsistent, with some suggesting that curvature is the primary factor controlling slip length (Falk et al., 2010; Kannam et al., 2012), while others show different results (Shan et al., 2022).

To address the above questions, we have considered a fluid composed of hard-spheres interacting with walls through the Maxwell scattering kernel. Although this modelling approach does not capture all the details of realistic fluid-wall interactions, it can provide valuable insights into the velocity slip by unravelling the essential features with the most relevant impact. An extensive simulation campaign was then carried out using event-driven molecular dynamics (EDMD), in two geometries (e.g., planar and cylindrical channels) with varying microscopic roughness (as described by the tangential

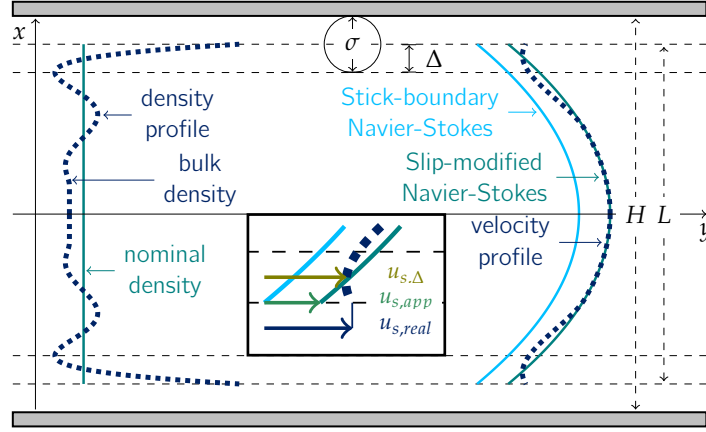


Figure 5.1: Depiction of a planar channel with nominal height H and characteristic length $L = H - \sigma$, with typical density (left) and velocity (right) profiles. The density profile shows the fluid structuring close to the walls, with the first dip marking the boundary of the Δ -layer. As highlighted in the inset, three different velocity slips can be defined: the mean velocity in the Δ -layer, assuming that the density there is constant ($u_{s,\Delta}$), the apparent velocity at the boundary, which gives the Navier-Stokes velocity profile in the fluid bulk ($u_{s,app}$), or the real fluid velocity at the boundary ($u_{s,real}$).

momentum accommodation), and a wide range of fluid rarefaction and confinement conditions. Complementary molecular dynamics (MD) simulations for argon confined between platinum surfaces were performed to show that the main results hold for more realistic systems¹.

The remainder of the paper is organised as follows. In [Section 5.2](#) we outline the theoretical treatment and the different computational methods used to numerically evaluate the fluid velocity slip. In [Section 5.3](#) we present the key findings of our research, which are validated with MD simulations in [Section 5.4](#). Finally, in [Section 5.5](#) we provide an overview of the significance of our work and future directions for research.

5.2 Methodology

5.2.1 Theory for the Slip Boundary Conditions

The streamwise component of the velocity u_y of a fluid flowing in a planar channel can be described by the Stokes equation, see [Eq. \(1.10\)](#)

$$\frac{\partial^2 u_y}{\partial x^2} = -\frac{nF_0}{\mu}, \quad (5.1)$$

1. Mr Yichong Chen carried out the MD simulations, following a close collaboration with the author, and likewise performed the postprocessing of results using scripts written by him.

where x is the coordinate normal to the wall, n and μ are the bulk fluid number density and shear viscosity, respectively, and F_0 is the external force per molecule, which can be interpreted as the pressure gradient $-dP/dy$ acting on the fluid, normalised by the nominal number density.

The governing expression, Eq. (5.1), must be supplemented with a boundary condition. A first possibility, which seems very natural for a fluid under molecular confinement, is that presented in Hansen et al. (2011). This is an integral boundary condition that defines the velocity slip u_s as the centre of mass velocity of a thin layer of fluid of constant density and finite width Δ near the wall, which we will call the Δ -layer. The width of the Δ -layer is defined as the distance from the wall where the first density oscillation dip occurs, which varies approximately in the range $[\sigma/2, \sigma]$ as the density of the fluid decreases (see Figure 5.1).

The corresponding integral boundary conditions are

$$u_{s,\Delta}^- = \frac{1}{\Delta} \int_{-L/2}^{-L/2+\Delta} u_y dx, \quad \text{at the lower wall,} \quad (5.2a)$$

$$u_{s,\Delta}^+ = \frac{1}{\Delta} \int_{L/2-\Delta}^{L/2} u_y dx, \quad \text{at the upper wall,} \quad (5.2b)$$

where, by symmetry, $u_{s,\Delta}^- = u_{s,\Delta}^+ = u_{s,\Delta}$. Alternatively, one can adopt the Neumann boundary condition for partial slip as derived by Navier (Navier, 1823), commonly used for dilute gases, which linearly relates the tangential component of the velocity field to the strain rate normal to the wall (rearranging terms in Eq. (1.11))

$$u_{s,\Delta}^\mp = \pm L_s \left. \frac{\partial u_y}{\partial x} \right|_{x=\mp L/2}, \quad (5.3)$$

where L_s is the slip length. The solution to the boundary value problems, Eq. (5.1) and Eq. (5.2) or Eq. (5.1) and Eq. (5.3), produces the slip-modified Poiseuille equation for fluid flows in planar channels

$$u_y(x) = \frac{nF_0}{2\mu} \left(-x^2 + \frac{L^2}{4} - \frac{L\Delta}{2} + \frac{\Delta^2}{3} \right) + u_{s,\Delta} = \frac{nF_0}{2\mu} \left(-x^2 + \frac{L^2}{4} \right) + u_{s,app}, \quad (5.4)$$

and the following one-to-one correspondence can thus be found between the two different velocity slips (see also the inset in Figure 5.1, which illustrates the relationship between $u_{s,\Delta}$ and $u_{s,app}$, both of which differ from the actual velocity slip at the wall, $u_{s,real}$)

$$u_{s,\Delta} = u_{s,app} + \frac{nF_0}{2\mu} \left(\frac{L\Delta}{2} - \frac{\Delta^2}{3} \right). \quad (5.5)$$

A model for $u_{s,\Delta}$ can be derived by considering the balance of forces acting on the Δ -layer (Hansen et al., 2011). These forces include the damping force exerted by the wall, the shearing force from the overlying fluid, and the total external force driving the flow. Accordingly, the balance of forces on, for instance, the lower Δ -layer reads

$$m_s \frac{du_{s,\Delta}^-}{dt} = -\zeta_{0,\Delta} u_{s,\Delta}^- + A\mu \left. \frac{\partial u_y}{\partial x} \right|_{-L/2+\Delta} + m_s F_0, \quad (5.6)$$

where m_s accounts for the total mass of the Δ -layer, $\zeta_{0,\Delta}$ is the so-called zero-frequency friction coefficient, and $A = \ell_y \ell_z$ is the surface area of the interface located between the Δ -layer and the fluid, where the strain rate should be evaluated. In steady conditions, using the velocity profile given by Eq. (5.4), the velocity slip can be derived as

$$u_{s,\Delta} = \frac{nF_0}{2\xi_{0,\Delta}} L, \quad (5.7)$$

where $\xi_{0,\Delta} = \zeta_{0,\Delta}/A$ is referred to as the interfacial friction coefficient, which relates the transfer of momentum at the boundary with the velocity slip (Bocquet & Barrat, 2007). As shown in Eq. (5.7), the velocity slip and the friction coefficient are linearly related and can therefore be used interchangeably. Note that a relationship similar to Eq. (5.7) also relates $u_{s,app}$ and $\xi_{0,app}$, as can be inferred by letting Δ go to zero. The analytical determination of the interfacial friction coefficient is still an open problem, so numerical methods are commonly used. Once the friction coefficient has been found, the velocity slip follows from Eq. (5.7) and the overall velocity field from Eq. (5.4).

This section presented the slip solution for fluid flow in a planar channel, but a similar solution can be worked out for the fluid flow in a tubular geometry. The equation for fluid flow in a cylindrical pipe with axis z using the Stokes equation in cylindrical coordinates is written as

$$\frac{1}{r} \frac{\partial}{\partial r} \left(r \frac{\partial u_z}{\partial r} \right) = -\frac{nF_0}{\mu}, \quad (5.8)$$

where u_z is the axial velocity component and r is the radial distance from the central streamline axis of the cylindrical channel. The integral boundary condition complementing the governing equation is

$$u_{s,\Delta} = \frac{2}{\Delta(L-\Delta)} \int_{L/2-\Delta}^{L/2} r u_z dr, \quad (5.9)$$

which is equal to the mean velocity of the fluid in the thin shell adjacent to the wall under the assumption of constant density in the Δ -layer, while the Navier slip boundary condition reads

$$u_{s,app} = -L_s \left. \frac{\partial u_z}{\partial r} \right|_{r=L/2}. \quad (5.10)$$

The solution to the boundary value problem, either Eq. (5.8) and Eq. (5.9) or Eq. (5.8) and Eq. (5.10), is referred to as the slip-modified Hagen-Poiseuille solution

$$u_z(r) = \frac{nF_0}{4\mu} \left(-r^2 + \frac{L^2}{4} - \frac{L\Delta}{2} + \frac{\Delta^2}{2} \right) + u_{s,\Delta} = \frac{nF_0}{4\mu} \left(-r^2 + \frac{L^2}{4} \right) + u_{s,app}, \quad (5.11)$$

and the following one-to-one correspondence can thus be found between the two different velocity slips

$$u_{s,\Delta} = u_{s,app} + \frac{nF_0}{4\mu} \left(\frac{L\Delta}{2} - \frac{\Delta^2}{2} \right). \quad (5.12)$$

As for the planar geometry, a momentum balance similar to Eq. (5.6) can be evaluated for the fluid in the annular Δ -layer

$$m_s \frac{du_{s,\Delta}}{dt} = -\zeta_{0,\Delta} u_{s,\Delta} + A\mu \frac{\partial u_z}{\partial r} \Big|_{L/2-\Delta} + m_s F_0 = 0, \quad (5.13)$$

where now the surface area in the delta shell-fluid interface depends on the width of the annular region, $A = \pi (L - \Delta) \ell_z$, being ℓ_z the length of the tube. Accordingly, a linear relationship between the velocity slip and the friction coefficient can be found as

$$u_{s,\Delta} = \frac{nF_0}{2\xi_0} \frac{L}{2}. \quad (5.14)$$

5.2.2 Fluid and Geometry Characterisation

In this work, we consider the steady flow of a fluid composed of N hard spherical particles with diameter σ and molecular mass m confined in two different geometries: a planar channel defined by two parallel plates separated by a distance $H = h + \sigma$, and a cylindrical channel with diameter $D = d + \sigma$. The relevant flow characteristic length L is defined as the effective height h and diameter d of the planar and cylindrical channels, respectively, to account for the finite size σ of the hard spheres (Herrero et al., 2019), see Figure 5.1.

The fluid-wall interactions are described by the Maxwell scattering kernel. Accordingly, a fraction α of the molecules hitting the wall is assumed to be diffusely re-emitted into the fluid after thermalisation with the wall, while the remaining $1 - \alpha$ is specularly reflected. The coefficient α can thus be identified with the tangential momentum accommodation coefficient (TMAC) (Kremer, 2010).

The fluid behaviour is mainly characterised by two dimensionless groups, namely the nominal reduced density $\eta_0 = n_0 \pi \sigma^3 / 6$, where n_0 is the nominal number density, and the confinement ratio $R = L / \sigma$. The reduced density indicates the number of fluid particles in the theoretical volume occupied by one molecule, and is used to measure the packing fraction, thus distinguishing between dense (high η) and dilute (low η) fluid

flows. On the other hand, the confinement ratio is a measure of the channel size which, in turn, determines the extent of fluid inhomogeneities. As discussed in more detail in [Section 5.3.3](#), larger values of R correspond to stronger ordering in the fluid near the surface and therefore a more pronounced density peak, whereas lower values of R are associated with a greater density depletion compared to the nominal density in the central region of the channel. The Knudsen number can be expressed in terms of the two dimensionless groups above

$$Kn(\eta, R) = \frac{\lambda}{L} = \frac{16}{5\pi} \frac{\mu}{P} \sqrt{\frac{\pi kT}{2m}} \frac{1}{L} = \frac{\mu_f(\eta)}{6\sqrt{2}\eta Z(\eta)R}, \quad (5.15)$$

where η refers to the bulk reduced density, which is smaller than the nominal one in confined geometries, see the representation of the density profile in [Figure 5.1](#). The definition of the mean free path is based on the shear viscosity μ for a fluid of hard spheres, whose second order Enskog approximation reads ([Kremer, 2010](#))

$$\mu = \frac{5}{16\sigma^2} \sqrt{\frac{mkT}{\pi}} \mu_f = \frac{5}{16\sigma^2} \sqrt{\frac{mkT}{\pi}} \frac{1}{\chi} \left[1 + \frac{16}{5} \eta \chi + \frac{64}{25} \left(1 + \frac{12}{\pi} \right) \eta^2 \chi^2 \right]. \quad (5.16)$$

Note that μ_f represents the dense gas correction for the shear viscosity of a rarefied gas, and it depends on the contact value of the pair correlation function χ in uniform equilibrium, which comes from the equation of state for the hard-sphere fluid $P = nkTZ$ ([Carnahan & Starling, 1969](#))

$$\chi = \frac{1}{nb} (Z - 1) = \frac{1}{2} \frac{2 - \eta}{(1 - \eta)^3}, \quad (5.17)$$

where P is the fluid pressure, k is the Boltzmann constant, T the temperature of the system, Z the fluid compressibility factor in [Eq. \(2.2\)](#), and $b = 2\pi\sigma^3/3$ is the second virial coefficient ([Kremer, 2010](#)).

5.2.3 Simulation Setup

The exact time evolution of the hard-sphere system is calculated using EDMD ([Pöschel & Schwager, 2005](#)). In these simulations, the state of the system jumps from one time to another corresponding to the next collision event by iteratively repeating three basic steps: (a) evaluating the time of the earliest collision event, (b) moving all particles ballistically for that time interval, and (c) updating the velocities of the particles that have collided with another particle or the wall, according to the laws of elastic hard-sphere dynamics or the Maxwell scattering kernel, respectively. It is important to note that the time step is not constant throughout the simulation run, as it depends on the positions and velocities of all molecules in the system. An exhaustive overview of this

methodology is detailed in [Section 2.5](#). To simplify the notation and data analysis, all physical quantities are made dimensionless in the rest of the paper by considering the molecular diameter σ as the reference length, the particle mass m as the reference mass, and the thermal velocity $\sqrt{kT/m}$ as the reference velocity.

For the planar geometry, the computational domain was a parallelepiped box with dimensions $[H; \ell_y; \ell_z]$ and periodic boundary conditions in the y and z directions, whereas for the cylindrical geometry, the computational domain was a cylindrical box with dimensions $[R; \ell_z]$ and periodic boundary conditions in the z direction. For the planar and cylindrical geometry, the streamline lengths (ℓ_y and ℓ_z , respectively) were chosen to be long enough to avoid end effects, and, for the planar geometry, the spanwise dimension ℓ_z was set to match the desired reduced density η_0 . In the cylindrical case, the Maxwell scattering kernel was implemented as described in [Verbeek \(2010\)](#) to properly account for the surface curvature, see also [Appendix A](#).

The typical simulation was run with over 2.5×10^4 particles to reduce the size dependence of the system and improve the statistical significance of the computed quantities. The particles were initially placed randomly, with the velocity sampled from the Maxwell-Boltzmann distribution using the Box-Muller algorithm. The reduced density was varied in the range $\eta_0 = [0.01, 0.30]$ and the confinement ratios in $R = [10, 50]$, resulting in Knudsen numbers spanning a wide range of values, i.e. $Kn = [0.008, 1]$. In the Poiseuille (planar channel) and Hagen-Poiseuille (cylindrical channel) fluid flows, a constant external force is applied to the particles. The force was chosen in the range $[0.003, 0.05]$ so that the flow is in the linear flow regime. This ensured proper dissipation of the added heat through the wall and prevented the temperature profile from being affected by the external force.

5.3 Results and Discussion

5.3.1 Numerical Evaluation of the Friction Coefficient

Before addressing the two key questions posed in [Section 5.1](#), we first calculate the friction coefficient for both planar and cylindrical geometries, over a wide range of nominal reduced densities η_0 and confinement ratios R , for rough surfaces represented using a fully diffuse setting ($\alpha = 1$). We have chosen to compute the friction coefficient, rather than the velocity slip or the slip length, because it only encapsulates information about fluid-wall interactions and is independent of the channel size, the bulk fluid properties such as its density or shear viscosity and, in our simulation setup, the external force. This allows for a more direct comparison of the fluid behaviour next to the wall across different systems and setups.

Table 5.1: Planar channels. Comparison of interfacial friction coefficients $\xi_{0,\Delta}$ for nominal reduced densities η_0 and confinement ratios R of interest, using non-equilibrium (left column) and equilibrium (right column) approaches. Walls are fully diffuse ($\alpha = 1$).

η_0	$R = 50$		$R = 40$		$R = 30$		$R = 20$		$R = 15$		$R = 10$	
0.30	1.060	0.999	1.047	1.002	1.024	0.994	0.973	0.943	0.961	0.915	0.908	0.883
0.25	0.746	0.772	0.721	0.737	0.704	0.699	0.678	0.687	0.664	0.654	0.633	0.641
0.20	0.496	0.474	0.480	0.467	0.467	0.454	0.468	0.459	0.448	0.431	0.445	0.425
0.15	0.326	0.303	0.321	0.296	0.309	0.299	0.309	0.289	0.301	0.284	0.295	0.296
0.10	0.193	0.186	0.191	0.193	0.189	0.183	0.190	0.179	0.187	0.170	0.184	0.176
0.075	0.143	0.107	0.144	0.107	0.144	0.095	0.141	0.096	0.138	0.095	0.117	0.092
0.05	0.096	0.062	0.097	0.054	0.096	0.058	0.094	0.048	0.071	0.057	0.070	0.057
0.025	0.051	0.024	0.051	0.024	0.035	0.022	0.034	0.027	0.033	0.024	0.032	0.024
0.01	0.014	0.008	0.014	0.008	0.013	0.009	0.013	0.009	0.012	0.008	0.011	0.007

The friction coefficient was calculated using two independent approaches. In the first approach, which involves non-equilibrium EDMD simulations, $\xi_{0,\Delta}$ is calculated using Eq. (5.7), where $u_{s,\Delta}$ is evaluated directly from the velocity field as the mean velocity of the fluid in the Δ -layer according to Eq. (5.2). In the second approach, $\xi_{0,\Delta}$ is calculated as the Laplace transform of the ratio between the force-velocity correlation function (being the force that is exerted by the fluid on the wall, or viceversa) and the velocity-velocity autocorrelation function of the fluid in the Δ -layer. These correlation functions are obtained from equilibrium EDMD simulations in the zero external force limit. It is important to note that in our simulations, the fluid-wall interaction is modelled using a step function rather than a continuous potential, such as the Lennard-Jones potential. Consequently, the force exerted by the surface on the fluid in the Δ -layer was determined by evaluating the average momentum change of particles colliding with the wall, which differs from the approach described in the original work (Hansen et al., 2011). A more detailed description of this procedure is presented in Appendix C.

The results of the different calculations are shown in Table 5.1 for the planar geometry and in Table 5.2 for the cylindrical geometry. The relative error of the equilibrium and non-equilibrium predictions with respect to their mean is within 4% for $\eta_0 \geq 0.1$, but diverges rapidly for smaller values, which is not unexpected since for more dilute fluids the density fluctuations do not allow the correlation functions to be evaluated accurately enough (Hansen et al., 2011).

It is worth noting that, for the largest channels (i.e., small curvature effect) and smallest reduced densities (i.e., spatially homogeneous density with a bulk density close to the nominal value), the coefficients of friction of the planar and cylindrical geometries evaluated using the non-equilibrium approach agree with each other and approach the

Table 5.2: Cylindrical channels. Comparison of interfacial friction coefficients $\xi_{0,\Delta}$ for nominal reduced densities η_0 and confinement ratios R of interest, using non-equilibrium (left column) and equilibrium (right column) approaches. Walls are fully diffuse ($\alpha = 1$).

η_0	$R = 50$		$R = 40$		$R = 30$		$R = 20$		$R = 15$		$R = 10$	
0.30	0.913	0.907	0.896	0.931	0.896	0.919	0.878	0.861	0.863	0.872	0.794	0.771
0.25	0.623	0.626	0.601	0.595	0.601	0.629	0.613	0.633	0.587	0.610	0.555	0.568
0.20	0.414	0.433	0.427	0.439	0.411	0.447	0.399	0.395	0.393	0.401	0.378	0.391
0.15	0.266	0.268	0.267	0.265	0.257	0.262	0.260	0.253	0.257	0.269	0.247	0.236
0.10	0.152	0.148	0.157	0.146	0.158	0.152	0.157	0.157	0.152	0.141	0.148	0.161
0.075	0.114	0.105	0.114	0.103	0.108	0.102	0.109	0.110	0.108	0.111	0.105	0.105
0.05	0.069	0.056	0.070	0.059	0.069	0.065	0.069	0.056	0.069	0.062	0.066	0.057
0.025	0.034	0.025	0.034	0.026	0.034	0.026	0.033	0.026	0.033	0.027	0.031	0.029
0.01	0.014	0.009	0.014	0.009	0.013	0.009	0.013	0.010	0.012	0.010	0.012	0.010

value predicted by the Boltzmann equation (Kennard, 1938)

$$\xi_{0,B} = \frac{15}{8\sigma^3\bar{c}_1} \sqrt{\frac{2mkT}{\pi}} \eta, \quad (5.18)$$

where $\bar{c}_1 = 1.1144$ is the (constant) first-order slip coefficient for the hard-sphere Boltzmann equation (Gibelli, 2012).

5.3.2 Quantitative Criterion for the Validity of the Slip Solutions

The purpose of this section is to address the first key question posed in Section 5.1, namely to establish a criterion for the applicability of the slip solution to the description of force-driven fluid flows within molecular confinement. The accuracy of the slip solution was theoretically evaluated by using the velocity field from Eq. (5.4) and Eq. (5.11) for planar and cylindrical channels, respectively, with the velocity slip estimated from non-equilibrium simulations as described in Section 5.3.1, for fully diffuse walls ($\alpha = 1$). In these expressions, the curvature of the velocity profile (i.e., the coefficient of the quadratic term) was obtained by fitting the numerical velocity profile provided by non-equilibrium EDMD simulations, rather than being calculated directly from the bulk properties of the fluid. This was necessary because the direct numerical evaluation of the velocity's curvature, using bulk values of density and viscosity, is prone to numerical inaccuracies, which have been found to be up to 15% in the worst case. In fact, as shown in Eq. (5.4), the velocity curvature depends on the viscosity, which is a highly non-linear function of the density, as shown by Eq. (5.16), but the accurate estimation of the density is challenging, especially for large channels where a small force must be applied to keep the flow in the linear regime.

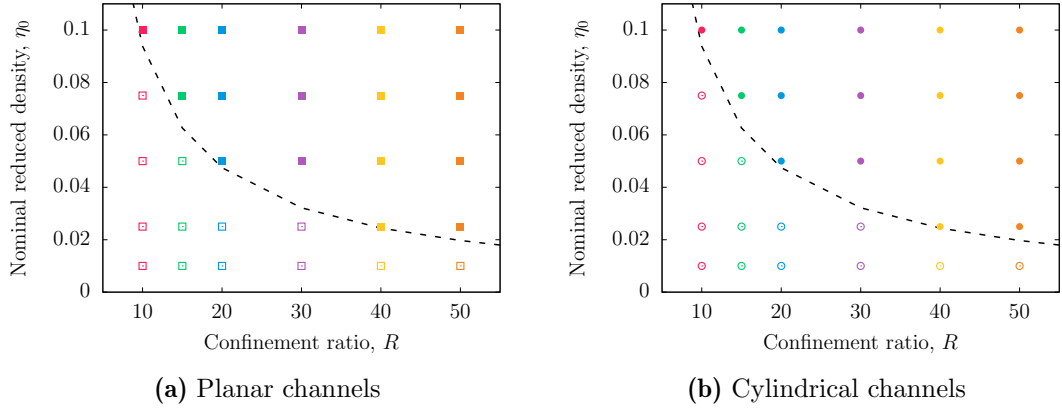


Figure 5.2: Range of validity of the slip solution for both planar and cylindrical geometries, for fully diffuse walls ($\alpha = 1$). The solid symbols represent flow conditions for which the slip solution provides an accurate representation of the flow, while the empty symbols indicate flow conditions for which it does not, i.e. the linear stress-strain relationship no longer holds. The dashed lines represents the fluid conditions corresponding to $Kn = 0.1$.

The results of this investigation are shown in [Figure 5.2a](#) and [Figure 5.2b](#) for planar and cylindrical channels, respectively. The solid symbols refer to fluid conditions and setups where the slip solution allows accurate retrieval of the true velocity field. It can be seen that the criterion for using the slip approach under dilute conditions also applies to dense fluids, namely that the Knudsen number must be less than about 0.1. This means that, although the friction coefficient can be calculated for fluids of any density and confinement ratio, it can be used within the Navier-Stokes framework (with slip boundary conditions) to predict the velocity profiles only if $Kn \lesssim 0.1$.

5.3.3 Rationalisation of the Interfacial Friction Coefficient Results

The purpose of this section is to address the second key question posed in [Section 5.1](#), namely how the density and confinement of the fluid, alongside the curvature of the channel and roughness of the walls, affect the friction coefficient. The main point to note is that the friction coefficient represents the transfer of tangential momentum between the fluid and the wall, and in our simple simulation setup this transfer can only occur when particles hit the surface. As we have verified in our simulations, the frequency of fluid-wall collisions is directly proportional to the density peak at the wall, and therefore a linear relationship between the friction coefficient and the density peak would be expected. In the literature, such a relationship has been derived under certain assumptions and supported by MD simulations for a Lennard-Jones fluid with realistic walls ([Barrat & Bocquet, 1999](#); [Priezjev, 2007](#); [G. J. Wang & Hadjiconstantinou, 2019](#)). However, the average density in the Δ -layer was used rather than the peak density, which

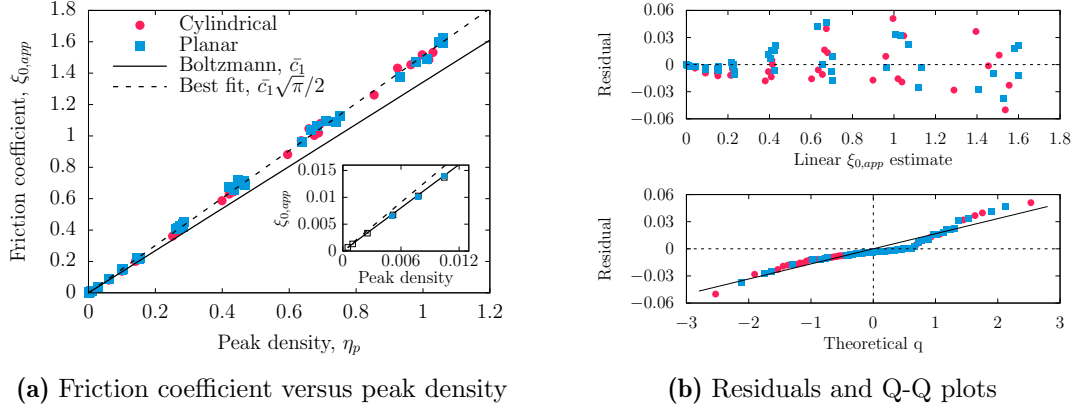


Figure 5.3: Friction coefficient versus the fluid peak density for the confinement ratios and nominal densities, corresponding to the solid symbols in Figure 5.2 in cylindrical (red solid circles) and planar (blue solid squares) channels. The dashed black line represents the best linear fit of the results, and the solid black line represents the kinetic prediction for rarefied gases, Eq. (5.18). The inset zooms in this regime at the bottom left-hand side. Walls are fully diffuse ($\alpha = 1$).

we believe to be more relevant, as discussed below. More importantly, conflicting results have been reported, with some suggesting a linear correlation (Barrat & Bocquet, 1999; G. J. Wang & Hadjiconstantinou, 2019) and others suggesting a power-law relationship with an exponent other than unity (Priezjev, 2007).

Figure 5.3a clearly shows that in the case of full accommodation, the friction coefficient scales linearly with the density peak in both planar and cylindrical channels, regardless of the nominal fluid density, confinement ratio and wall curvature. Two remarks are in order. First, using the Δ -layer density instead of the peak density would result in a non-linear relationship — showing that the peak density is more closely related to the friction coefficient. Second, the observation that the density peak is linearly proportional with the friction coefficient independent of confinement is not restricted to the hard-sphere model used in this study, as confirmed by complementary MD simulations (see Section 5.4) performed on argon gas confined between platinum walls in a planar geometry. The goodness of the linear fit shown in Figure 5.3a is indicated by the low value of the chi squared $\chi^2 \approx 0.0391$ statistic and the high value of the $\mathcal{R}^2 \approx 0.999$ index, and is further supported by the analysis of the residuals and the Q-Q scatter plot shown in Figure 5.3b. The lack of a clear pattern in the residuals (top) and the fairly good alignment along the bisector of the first quadrant of the Q-Q scatter plot (bottom) indicate that the residuals are approximately normally distributed, as they should be for an ideal linear fit. As can be seen more clearly in the inset of

Figure 5.3a, the proposed linear fit of the results is not entirely accurate in the limit of low density. In fact, its slope does not match the slope predicted by the Boltzmann equation, Eq. (5.18), as it should for these small reduced densities (note that under these conditions the peak density coincides with the nominal density).

EDMD simulations in dilute conditions are computationally intensive, so we further support this conclusion by solving the Enskog equation, which gives equivalent results to EDMD in the low density limit (see empty squares in the inset of Figure 5.3a). The Enskog equation was solved with an independent code that implements a particle method (Frezzotti, 1997). Even Enskog solutions fit perfectly the linear relationship predicted by the Boltzmann equation and deviate from the proposed linear fit (dashed line). This clearly shows that the discrepancy is due to the proposed fit and not, as one might have thought, to non-local effects which, unlike the Boltzmann equation, are included in the Enskog equation even in the low density regime. Note, however, that these deviations are minimal, so the proposed linear fit is still a good engineering approximation in the entire range of nominal fluid densities.

The results presented in Figure 5.3a help to resolve some inconsistencies reported in previous studies. First, our results clarify that the key quantity influencing the friction coefficient of a fluid is the peak density, rather than the nominal density (Shan et al., 2022), the fluid confinement (Thomas & McGaughey, 2008b) or the channel curvature (Falk et al., 2010; Kannam et al., 2012). Furthermore, in Shan et al. (2022) it was found that, at constant density, the friction coefficient in planar channels decreases as the confinement becomes tighter, in contrast to the results in Falk et al. (2010) and Hansen et al. (2011) where it was found to remain unchanged. According to our results, the friction coefficient decreases because (for a given nominal density) the tighter the confinement, the lower the density peak (Thomas & McGaughey, 2008a), regardless of the channel curvature.

This conclusion is clearly shown in Figure 5.4, where the density peak is plotted against the nominal density. For both planar and cylindrical channels, it is observed that at constant confinement the peak density increases quadratically with the nominal density, whereas at constant density, higher degrees of confinement (i.e., lower R values) result in smaller density peaks (in the fittings $\mathcal{X}^2 \gtrsim 0.057$ and $\mathcal{R}^2 \gtrsim 0.997$). This can be explained by the fact that the bulk density becomes increasingly smaller than the nominal density when the degree of confinement increases (G. J. Wang & Hadjiconstantinou, 2015), as it can be seen in the two insets of Figure 5.4. As a result, the net force pushing the atoms towards the walls (Frezzotti, 1997), which is proportional to the bulk density, decreases and so does the peak density. It is found that the relationship between the nominal density and the peak density is well approximated by a polynomial fit, which,

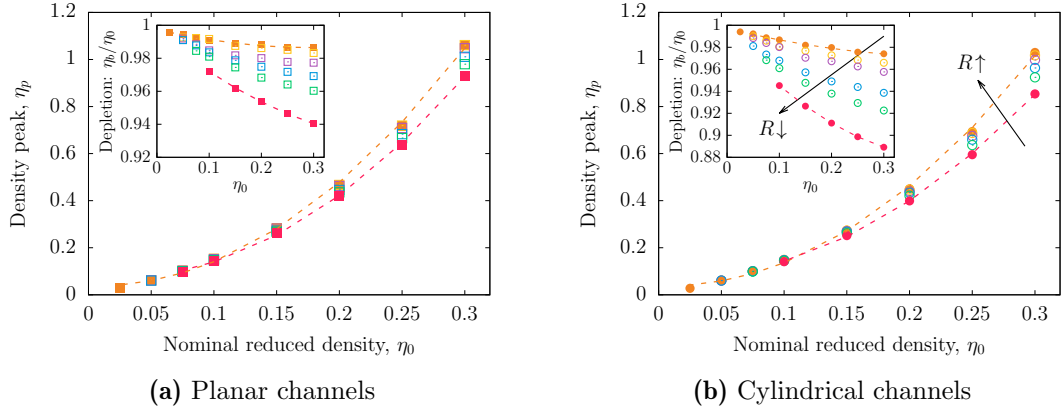


Figure 5.4: Comparison of peak density at the wall and nominal reduced density for different confinement ratios, with insets showing the effect of fluid layering on bulk density reduction, i.e. depletion, at different levels of confinement. Walls are fully diffuse ($\alpha = 1$). The same colour scheme as in Figure 5.2 was used for the confinement.

for instance, in the cylindrical geometry reads

$$\eta_p = (0.0515R + 7.7012)\eta_0^2 + (-0.0033R + 0.5228)\eta_0, \quad (5.19)$$

with a relative error of less than 10% for $\eta_0 \gtrsim 0.1$.

Finally, we consider the case of walls with a smaller microscopic roughness, or equivalently a smaller α . Figure 5.5 shows that the friction coefficient remains a linear function of the peak density, with the results for planar and cylindrical channels superimposed. The peak density does not depend on α , but the friction coefficient is found to decrease with it according to the inverse Smoluchowski prefactor $\alpha/(2 - \alpha)$, as is the case under dilute conditions. Note that the dependence of the friction coefficient on α is not unexpected, since for the same collision frequency of particles with walls, the transfer of tangential momentum between fluid and wall becomes less efficient as the accommodation coefficient decreases. However, this finding further validates our results. Indeed, the scaling based on the Smoluchowski factor was mathematically derived in rarefied conditions, but if a linear relationship between the friction coefficient and peak density holds, the same factor should also allow the results to be rescaled in the dense regime.

The results shown in Figure 5.3, Figure 5.4, and Figure 5.5 together allow us to answer the question posed at the beginning of this Section. For a given confinement ratio, the peak density increases significantly as the nominal density increases, especially for looser confinement of the fluid (Figure 5.4). Accordingly, the interfacial friction coefficient increases (Figure 5.3a) and the velocity slip decreases. Conversely, for a given density, the peak density decreases as the confinement ratio increases, especially at higher densities (insets of Figure 5.4 showing the depletion in the middle region of the

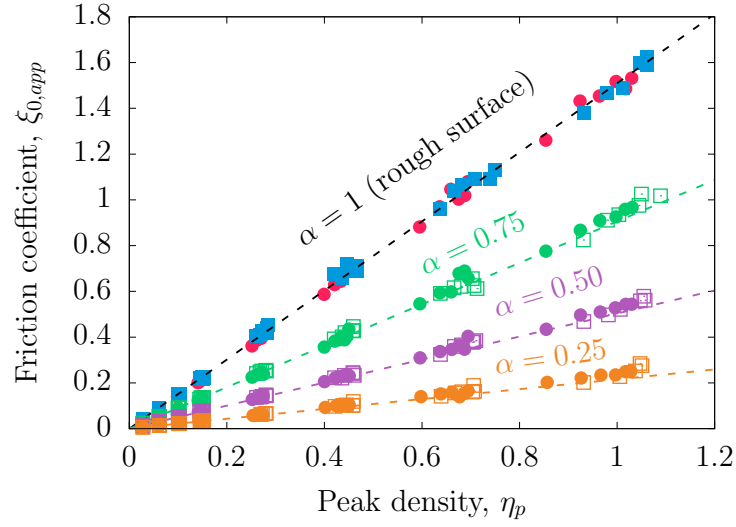


Figure 5.5: Friction coefficient versus the accommodation coefficient of the wall. As in the fully diffuse case, results do not depend on the channel geometry for partial TMAC (planar geometries are represented with empty symbols as a guide to the eye). Coloured dashed lines represent the Smoluchowski scaling for the black dashed line.

channel), resulting in a decrease in the friction coefficient and an increase in the velocity slip. Finally, the friction coefficient is independent of wall curvature and decreases with the Smoluchowski factor as one moves from rough to smooth surfaces, decreasing the TMAC value (Figure 5.5). Note that in realistic systems, it may be the case that a change in wall curvature leads to a smoother energy landscape of fluid-wall interactions, and therefore a decrease in TMAC and a decrease in the friction coefficient (Falk et al., 2010).

It should be emphasised that the slip phenomenon is often treated on the basis of transition state theory. In particular, molecules adjacent to walls must overcome an energy barrier due to fluid-wall interactions and jump between free sites with a preferred direction for velocity slip to occur. According to this framework, under tight confinement, velocity slip increases because the energy barrier decreases and molecules jump with higher frequency along the wall sites (Falk et al., 2010; Martini et al., 2008; Shan et al., 2022; Thomas & McGaughey, 2008b). In our simulation setup, confinement (governed by R) and microscopic roughness (governed by α) are decoupled, and the effect of fluid-wall interactions is primarily controlled by microscopic roughness. However, even when the roughness remains constant, variations in velocity slip can occur due to changes in fluid density or confinement. This observation highlights the importance of fluid-fluid

Table 5.3: Interatomic Lennard-Jones potential parameters ($\sigma_{\text{LJ}}, \epsilon_{\text{LJ}}$) used in the MD simulations. Molecular masses m [u]: Ar = 39.948, Pt = 195.084.

Atom pairs	σ_{LJ} [Å]	ϵ_{LJ}/k [K]
Ar – Ar	3.405	119.80
Pt – Pt	2.471	8053.6
Ar – Pt	2.940	79.139

interactions, which determine density peaks by generating a net force that pushes particles towards the walls. Therefore, we now know that fluid-fluid interactions also contribute to the friction coefficient (via the density peaks), and such a finding highlights the unique insights provided by our simple approach.

5.4 Molecular Dynamics Simulations

The observed linear relationship between friction coefficient and density peak shown in [Figure 5.3a](#) is not just an artefact of the hard-sphere model used in EDMD, but it persists when more realistic intermolecular interactions are considered. To support this claim, non-equilibrium MD simulations were performed using the open-source LAMMPS software ([Plimpton, 1995](#)). The simulation setup consisted of monatomic argon (Ar) molecules confined within planar physical walls, defined by platinum (Pt) atoms following a face-centred cubic array with a lattice parameter of 3.92 Å. The distance between the walls was assumed to be H , and periodic boundary conditions were applied in the non-constraining directions where $L_y = L_z = 400$ Å. The interactions were modelled using the 12-6 Lennard-Jones potential with a cut-off of 15 Å, and the velocity Verlet algorithm with a time step of 1 fs was used to integrate the molecular trajectories. The parameterised length σ_{LJ} and energy ϵ_{LJ} scales for the different atom pairs, including Ar–Ar, Pt–Pt and Ar–Pt ([Spijker et al., 2010](#)), are listed in [Table 5.3](#). An external force of $F_0 \leq 5.5 \times 10^{-14}$ N/atom was applied in the streamwise direction, ensuring that its magnitude was sufficiently small to keep the flow in the linear regime.

Each MD simulation consisted of two steps: equilibration and production. During the equilibration step, the temperature of both the gas and wall atoms was maintained at 300 K using a Nosé-Hoover thermostat with a time constant of 100 fs. After equilibration, the thermostat was turned off on the gas molecules to avoid biasing their slipping behaviour. Similar to EDMD, the quantities in MD simulations were made dimensionless using the reference values $\sigma = 3.35$ Å and $m = 6.63 \times 10^{-26}$ kg, and the friction coefficient was calculated using the procedure described in [Section 5.3](#). The TMAC value for the gas-surface interaction was found to be $\alpha = 0.49$, independent of the confinement ratio.

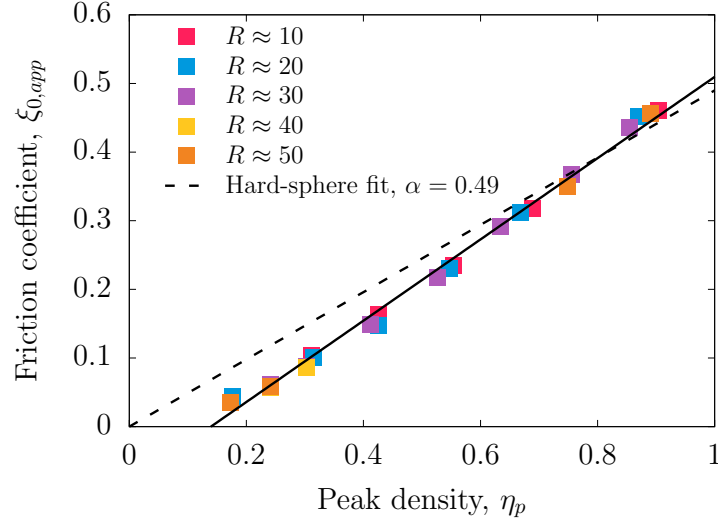


Figure 5.6: Friction coefficient versus fluid peak density for MD, in the same range of confinement ratios and nominal densities to those of the EDMD simulations. The solid line corresponds to the best linear fit of the MD results, whereas the dashed line represents the EDMD fit with the TMAC value from MD simulations (i.e., $\alpha = 0.49$).

Although the MD simulations refer to a more realistic fluid than EDMD, [Figure 5.6](#) shows that a linear relationship between the interfacial friction coefficient and the density peak is still observed. The discrepancies between the results of the two simulation setups are not unexpected and are due to the different intermolecular interactions (Lennard-Jones in MD versus hard-sphere in EDMD) and the different scattering of molecules at the walls (real versus stochastic). However, these discrepancies do not detract from the remarkable qualitative similarity of the results, which clearly demonstrate the ability of the simpler modelling approach used in this study to provide qualitatively valid results for real-world scenarios.

5.5 Conclusions

The aim of this study was to investigate the velocity slip of fluids in molecular-scale channels, in particular the validity of the Navier-Stokes equation with slip boundary conditions. This study used a hard-sphere fluid model and performed an event-driven molecular dynamics simulation study, varying fluid properties, confinement degree, geometry, and surface microscopic roughness.

The results for both planar and cylindrical channels clearly showed that the effect of surface curvature alone is negligible and that the friction coefficient (or, equivalently, the velocity slip) depends on two mechanisms. First, the collision frequency of the molecules with the wall, which determines the “gross” momentum transfer, i.e., the

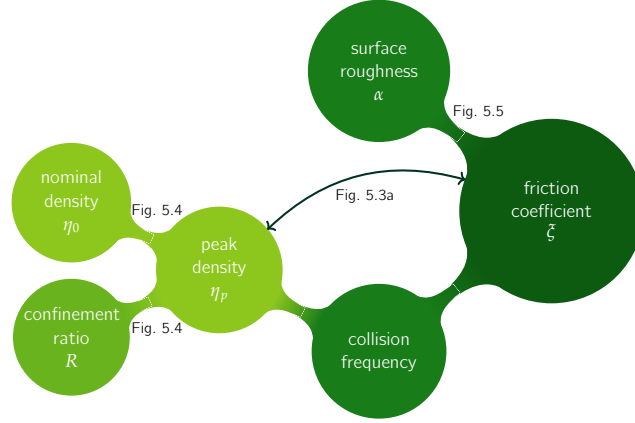


Figure 5.7: Summary of the main results. When a fluid of nominal density η_0 is confined in a channel of confinement ratio R , oscillations in the density profile form in the region adjacent to the walls. The corresponding peak density η_p is a proxy for the collision frequency of the fluid molecules with the walls. The collision frequency, together with the accommodation coefficient, determines the amount of tangential momentum transferred from the fluid to the wall, which is ultimately related to the friction coefficient.

amount of momentum potentially transferable to the walls. Second, the microscopic roughness of the walls, which determines the “net” momentum transfer, i.e., the amount of momentum actually transferred to the walls. Specifically, we found that the fluid-wall collision frequency depends linearly on the density peak that occurs adjacent to the boundary, rather than on the nominal fluid density or the confinement ratio individually. Note that this linear relationship is not an artefact of the hard-sphere model used in our study, as it is confirmed by complementary MD simulations of argon gas on platinum walls. On the other hand, in our simulation setup, the microscopic roughness is simply modulated by the accommodation coefficient.

Our study found that the criterion for the slip solution, which is valid in dilute conditions, also holds for dense gases. That is, the Knudsen number must be less than $Kn \lesssim 0.1$ for the Navier Stokes with slip boundary conditions to provide an accurate description of the fluid flow. We also show that:

- For a fixed confinement ratio, the friction coefficient (velocity slip) increases (decreases) with increasing nominal density. This is because a higher density results in a larger fluid layering on the walls and therefore a higher fluid-wall collision frequency, which hinders fluid slippage.
- For a fixed density, the friction coefficient (velocity slip) increases (decreases) with larger confinement ratios. This is because a tighter confinement leads to a smaller fluid layering on the walls and therefore a lower fluid-wall collision frequency, which promotes fluid slippage.

- The friction coefficient (velocity slip) is independent of the wall curvature and decreases according to the inverse Smoluchowski prefactor as one moves from rough to smooth surfaces.

These results, which are visually summarised in [Figure 5.7](#), provide valuable insights into the physics of confined fluids and represent an important step towards understanding the molecular mechanisms behind fluid velocity slip in molecular-sized channels. Future research directions could include a more systematic probe of how the complexity of the fluid model, such as molecules interacting through continuous potentials, as well as more realistic fluid-wall interactions, affect fluid slippage at walls. This would help to resolve the current inconsistencies in the velocity slip literature.

Concluding Remarks

6.1 Executive Summary

This thesis sheds light on some of the fundamental transport mechanisms that occur at the nanoscale, where molecular effects dominate the physical landscape. To accurately capture the anomalous fluid behaviour, new perspectives and computational simulations are needed, as the conventional approximations underpinning the classical theories are no longer valid. In general, these discrepancies are attributed to phenomena that become increasingly important in systems with high surface-to-volume ratios, such as the layering that occurs next to the boundaries. Our research is based on a fluid of hard spheres confined between stochastic walls, because the essence of a property of interest is best revealed in the simplest of configurations in which it occurs. Moreover, the study of such models provides results that, under certain conditions, can be directly compared with predictions coming from kinetic theory. The latter provides invaluable analytical insights by bridging the gap between continuum-based hydrodynamics and the numerical results obtained from high-fidelity molecular dynamics simulations.

The lack of understanding was not limited to studies of fluids in motion, where external driving forces are present, but also to equilibrium processes — such as the self-diffusion process in molecular-like confinements. The first result of this study is that the Einstein relation, originally derived for the bulk fluid scenario, can still be used to describe Fickian diffusion under tight confinement. In addition, a semi-analytical treatment, based on the Bosanquet formula, is proposed to predict the self-diffusivity values over the entire range of Knudsen numbers, regardless of the governing diffusive mechanism, for different channel sizes and wall microscopic features. These observations on confined diffusion mechanisms lay the groundwork for investigating more complicated phenomena, such as the Knudsen minimum disappearance in straight channels.

The flow of fluids within molecular confinements has been extensively studied for porous media, since there are practical applications, such as the shale gas seepage, that immediately benefit from a closer look. In this case, it has generally been found that the pressure-driven transport becomes diffusive because the fluid is in constant interaction with the confining solid matrix, which restricts its motion. However, this

problem has been overlooked in simpler geometries until very recently, when the puzzling disappearance of the Knudsen minimum was first reported. Although the Fick's law predicts a monotonic increase in mass flow with decreasing density, we find that its accuracy is poor whenever Knudsen diffusion does not control the diffusive dynamics. The second key outcome of this work is that the vanishing of the Knudsen minimum is due to the evolution of convective mechanisms within tighter confinements. In particular, the influence of the velocity slip overcomes the relevance of the remaining flow mechanisms.

This finding opens another avenue for further investigation, as the knowledge on fluid slippage at the nanoscale is not as well developed as for the classical rarefied conditions, given the complex interplay between dense and confinement effects. To tackle this open problem, for which contradictory results are stated in the literature, a comprehensive numerical study of the velocity slip process is carried out. First, the range of validity of the hydrodynamic framework is established, concluding that the criterion for dilute conditions ($Kn \leq 0.1$) also holds for dense gases. Our simple but robust fluid-wall system allows to unravel the complicated slip process through the fluid-wall friction, by decoupling its different contributions, e.g. fluid density, channel size, and energy landscape exerted by the wall. The key result is a strong dependence on the fluid peak density, where the transfer of tangential momentum depends on both the fluid-wall collision frequency and the wall accommodation coefficient. Interestingly, this relationship is also found to hold for more realistic systems, as similar conclusions are found in preliminary molecular dynamics simulations of fluids confined within physical walls.

Therefore, these findings will not only help to advance the fundamental understanding of transport phenomena in nanofluidics, which is crucial for accurate predictions, but also constitute a promising route for developing effective engineering tools. In the following, some future research directions are envisaged for the current simulation setup, as well as more involved numerical studies that contribute to the ongoing progress of the field.

6.2 Future Work

6.2.1 Additional Studies with the Existing Modelling Approach

Although all the transport results presented in this thesis refer to pressure-driven flows in straight channels, our simple simulation setup can be easily extended to other problems, such as thermal-driven flows. In analogy to the Knudsen paradox found in pressure-driven flows, anomalous phenomena are also found in non-equilibrium conditions for temperature-driven flows. One example is the so-called inverted temperature profile, that can occur for a fluid between two walls maintained at different temperatures, where condensation and evaporation processes occur at the boundaries (Frezzotti et al., 2003;

[Koffman et al., 1984](#)). Specifically, under certain conditions, a temperature profile can be found that is opposite of what thermodynamics predict. Moreover, it would not be surprising if, as in the pressure-driven case, a different behaviour is found by decreasing the separation between the confining plates.

A different kind of temperature-driven flow, with a more direct impact on practical applications, is the thermal creep flow ([Akhlaghi et al., 2023](#)), which underlies the working principle of the so-called Knudsen pump. There is a great interest in the development of these devices, as they do not contain mechanical elements subject to wear and tear. This type of flow arises when a fluid comes into contact with a non-isothermal boundary, characterised by a temperature gradient parallel to the flow direction. Momentum is transferred to the fluid in the opposite direction to that of the temperature gradient, resulting in a flow from the cold to the hot region. The thermal transpiration effect is accentuated under non-equilibrium conditions, i.e. $\lambda \sim L$, and is usually limited by the temperature that the materials of construction can withstand. Therefore, it is sensible to wonder whether, by decreasing the channel size, the theoretical efficiency can be increased by applying smaller driving forces, and/or not having to create an energy-intensive vacuum to drive the fluid out of thermodynamic equilibrium.

Another interesting transport mechanism that is expected to become important in confined geometries is surface diffusion. This conjecture is supported by the trajectories of particles inside such channels, which show that once a molecule gets close to the wall, it has a long residence time and wanders along the region adjacent to the boundary. Currently, the understanding of this mechanism is mainly based on phenomenological relations with little theoretical underpinning. Our simple fluid-wall configuration provides a robust framework for numerical studies, where, for instance, it would be interesting to study if the two “independent” surface diffusion processes next to each boundary linearly superimpose or behave according to some other kind of elementary relationship.

Furthermore, based on the results presented in this thesis, the following questions are posed: i) does surface diffusion transport allow to accurately predict the mass flow rate in ultra-tight geometries, namely $R \lesssim 5$?, and ii) what is the actual relationship between “microscopic” surface diffusion and “macroscopic” velocity slip phenomena? Regarding question i), this is an interesting gap to fill given that in such confinements the transport is not governed by regular diffusion and, at the same time, convective effects cannot be developed given the number of fluid layers that the channel can allocate. Regarding question ii), theoretical models for slip ([Martini et al., 2008](#); [G. J. Wang & Hadjiconstantinou, 2019](#)) assume a molecular motion similar to surface diffusion, following the principles of transition state theory, but a possible relationship between surface diffusion and the velocity jump in the Navier-Stokes framework (or the scattering dynamics in kinetic theory) has not been established yet.

6.2.2 Extensions to Different Fluid and Wall Systems

The use of the hard-sphere fluid model with ideal stochastic walls is advantageous for approximating the behaviour of simple fluids under confinement. However, the closer a model reflects the essential elements of natural phenomena, the better will be its usefulness. Thus, the extension of fluid and wall models can provide further insights, and bridge the gap between elementary understanding and more realistic systems. First of all, this would imply to investigate the impact that the surface model has on transport phenomena, acknowledging the importance of the boundary-induced physics in nanofluidics. The stochastic walls used in this thesis represent a convenient theoretical construct for the study of confined fluids. Indeed, the assumptions underlying the introduction of phenomenological scattering kernels are meaningful in the rarefied gas description. However, this constitutes an oversimplification in the study of dense fluids, where the time scale of fluid-wall interactions is not much shorter than the time scale of fluid-fluid interactions. A more comprehensive alternative, which remains in the framework of kinetic theory, is to include these interactions in the form of a collision integral (Frezzotti & Gibelli, 2008) when solving the governing kinetic equation.

However, the true fluid-wall interactions can only be modelled using deterministic molecular dynamics simulations, where walls are no longer mathematically defined, but represent a physical boundary instead. The influence of the different length and energy-scale parameters in the Lennard-Jones potential plays an important role, as does the distribution of the wall atoms on different cristalline lattices. As might be expected, this is a very complicated problem that needs to decouple the different contributions, in order to disentangle the actual effect of each parameter. For instance, concerning the work presented in Chapter 3, more involved self-diffusion studies were performed using MD simulations for realistic kerogen structures (Alafnan, 2022). The quantitative similarities in the self-diffusivity results highlight the potential of our simpler setup to predict results in confined geometries, where interactions with the boundaries are predominant.

Another interesting avenue for further investigation is a more complete definition of fluid-fluid interactions, which would also help to describe systems more realistically. For instance, the hard-sphere model does not allow to reproduce the real temperature dependence of the viscosity of real gases because of its constant cross-section for collisions. The variable hard-sphere description (Bird, 1994), in which the collisional cross-section is a function of the relative velocity of the colliding molecules, captures the right dependence while keeping the simplicity of the same scattering dynamics, subjected to standard kinetic equations.

Further extensions would imply the inclusion of intermolecular Van der Waals forces in the analysis, which can be done in a first approximation by superimposing an attractive soft potential tail to the purely repulsive hard-sphere fluid potential. The fluid would then interact according to the Sutherland potential, which can be solved using the Enskog-Vlasov equation (Frezzotti et al., 2005) after appropriate simplifying assumptions. The collision integral remains the same as in the Enskog equation, but the streaming part is modified to account for the attractive intermolecular forces between particles, with a Vlasov-like self-consistent force field. By adding this kind of forces, the Enskog-Vlasov equation has been used to capture the behaviour in more complex systems, e.g. involving several phases such as liquid-vapour interfaces, from the kinetic theory point of view.

We anticipate that this additional physics can be applied to better study velocity slip processes, where condensation-like processes (as already observed by Maxwell (1879) and Knudsen (1909) in their seminal contributions) occur next to the walls. This approach might also help to build physics-oriented models, as for instance the density layering in tight geometries, see Figure 5.4, resemble the behaviour predicted by the Brunauer-Emmett-Teller (BET) theory for multi-layer physical adsorption, in particular type III isotherms (Brunauer et al., 1940). However, as for fluid-surface interactions, a more complete picture is provided by the Lennard-Jones potential, which is studied through MD simulations. Some preliminary results are presented in Chapter 5, which validate the remarks drawn from EDMD simulations. This was at some point expected, considering that the main aspects of the fluid structuring (which acts as a gateway to slip, amongst many other nanofluidic transport phenomena) are determined by the hard-sphere term.

Last but not least, the study of more complicated geometries, such as porous media, can likewise be devised by distributing frozen spheres (of the same or different sizes) in the space available for the fluid flow within the channel. This is similar to the basic assumption considered in the development of the dusty gas model (Mason et al., 1967), which is an extension of the kinetic theory principles to study gas transport in porous media. By using this approach, one can ascertain the influence of porosity by completely decoupling it from tortuosity (channels are still straight), which are often used vaguely in the context of porous media studies.

The most obvious impact of both of them is to increase the fluid-wall collision frequency, but it is not clear their individual contribution on the porous media permeability. For instance, we expect that this methodology would allow to identify the predominance of diffusive mechanisms within tight confinements, which was not found in studies of straight channels, see Chapter 4. Moreover, given the simplicity of the hard-sphere model, it would be possible to decouple the true dependence of transport phenomena on fluid and wall properties. These are usually intertwined in more realistic configurations, thus hindering a first-principles understanding in the commonly performed MD studies.

Maxwell Scattering Kernel in Cylindrical Geometry

The extension of the Maxwell scattering kernel to cylindrical walls is performed following the approach presented in Verbeek (2010). Contrary to what happens in the planar wall case, where $\mathbf{u} = (u_x, u_y, u_z)$ is sampled from the Maxwell scattering kernel in Cartesian coordinates, in the cylindrical geometry one should sample $\mathbf{u} = (u_r, u_t, u_z)$ for convenience, where u_r and u_t are the radial (normal) and tangential components of the velocity, respectively. The decomposition of these radial and tangential velocities into their x, y -components involves easy trigonometrics, as one can see in Figure A.1

$$u_r = \begin{cases} u_r \cos \theta = u_r \frac{x}{r}, & \text{for the } x\text{-component,} \\ u_r \sin \theta = u_r \frac{y}{r}, & \text{for the } y\text{-component,} \end{cases} \quad \text{A.1}$$

$$u_t = \begin{cases} -u_t \sin \theta = -u_t \frac{y}{r}, & \text{for the } x\text{-component,} \\ u_t \cos \theta = u_t \frac{x}{r}, & \text{for the } y\text{-component,} \end{cases} \quad \text{A.2}$$

where $r = \sqrt{x^2 + y^2}$ and $\theta = \arctan(y/x)$, being the 2-argument arctangent, denote the polar coordinates. In order to ensure that particles are contained within the cylinder and are not lost after reflection, i.e. $\mathbf{u} \cdot \tilde{\mathbf{n}} > 0$ where $\tilde{\mathbf{n}}$ is the inward normal unit vector, the radial component u_r must switch its sign. Hence, the geometric argument that ensures the appropriate calculation of the velocities upon diffuse scattering ($\alpha = 1$) can be expressed concisely in matrix form

$$\begin{pmatrix} u_x \\ u_y \\ u_z \end{pmatrix} = \frac{1}{r} \begin{pmatrix} -x & -y & 0 \\ -y & x & 0 \\ 0 & 0 & r \end{pmatrix} \begin{pmatrix} u_r \\ u_t \\ u_z \end{pmatrix}. \quad \text{A.3}$$

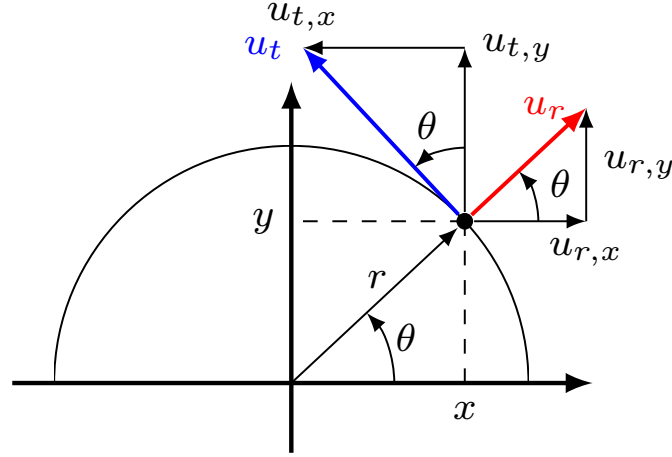


Figure A.1: Decomposition of the circular-based radial (red) and tangential (blue) velocity components into their linear homologues.

On the other hand, the specular reflection ($\alpha = 0$) simply changes the sign of the radial component of the impinging particle, so that its momentum is conserved. The z -component is left unaltered, and the x and y -coordinates are updated according to the relationships that permit to switch between linear and circular velocities

$$u_x = \frac{u_r + u_t \tan \theta}{\cos \theta + \sin \theta \tan \theta}, \quad \text{A.4}$$

$$u_y = \frac{u_x \sin \theta - u_t}{\cos \theta}. \quad \text{A.5}$$

The validity of this procedure for computing the post-collisional velocities in cylindrical geometries is tested by studying the flow transport in the free molecular regime, which is solely determined by fluid-wall interactions. In this regime, the collisionless transport follows the Knudsen diffusion mechanism, whose expression for the Knudsen self-diffusivity can be obtained from kinetic theory as

$$D_k = \frac{2 - \alpha}{\alpha} \frac{(d - \sigma)}{3} \sqrt{\frac{8kT}{\pi m}}. \quad \text{A.6}$$

The agreement between numerical results (using the Einstein relation) and the theoretical prediction of the Knudsen self-diffusivity, for different accommodation coefficients α , confirms the correct implementation of the cylindrical argument.

Another issue that requires special attention concerning the Maxwell scattering kernel is the computational implementation of the diffuse term (Tehver et al., 1998). This technicality is not just related with the cylindrical geometry, and also should be considered in a planar wall geometry. The parallel components of the velocity

$\mathbf{u}_p = (u_t, u_z)$ for the re-emitted particles are chosen from the Maxwellian distribution function at the wall temperature, whereas the normal component of the velocity (u_r in polar coordinates, u_x in Cartesian) must be sampled from a different distribution function

$$f^N(u_r) = \frac{m}{kT_w} u_r e^{-\frac{mu_r^2}{2kT_w}}. \quad \text{A.7}$$

Otherwise, if sampling the normal component from the Maxwellian too, one would not properly take into account the velocity-dependent probability with which particles collide with the wall, and so the distribution function adjacent to the boundary will be different than in the bulk.

Computation of the Collision Time with Cylindrical Walls

In two dimensions, the problem of calculating the collision times of fluid particles with cylindrical walls can be reduced to the simple geometric problem of finding the intersection points between a line and a circle, denoted by blue and red colours respectively in [Figure B.1](#). Here, the wall is described by the equation of a circle with radius R centered in (p, q)

$$(x - p)^2 + (y - q)^2 = R^2, \quad \text{B.1}$$

and the particle i is located at $\mathbf{r}_i = (x_i, y_i)$, moving with velocity $\mathbf{u}_i = (u_{xi}, u_{yi})$ in a linear trajectory with slope $m_i = u_{yi}/u_{xi}$ and y -intercept $a_i = y_i - m_i x_i$. For simplicity, it is assumed that the centre of the circle is located in the origin of coordinates $(p, q) = (0, 0)$, so that the intersection points are trivially found by solving

$$(m_i^2 + 1) x_{int,i}^2 + (2m_i a_i) x_{int,i} + a_i^2 - \left(R - \frac{\sigma}{2}\right)^2 = 0, \quad \text{B.2}$$

which always have two solutions for $x_{int,i}$, as the line representing the trajectory of the particle i , by being inside the circle, will always intersect the wall twice. Once the two intersection points are found, the actual collision point is easy to determine based on the x -component of the velocity. That is, if u_{xi} is positive, then $x_{int,i}$ would be the larger value of the two of them, as sketched in [Figure B.1](#), whence $y_{int,i} = m x_{int,i} + a_i$ is obtained. The viceversa reasoning would apply otherwise.

This approach presents a singularity when $u_{xi} = 0$, as the slope m_i would be infinite. In that case, the x -coordinate of the collision $x_{int,i}$ would correspond to the x -location of the particle, whereas the y -coordinates easily follow from

$$y_{int,i} = \pm \sqrt{\left(R - \frac{\sigma}{2}\right)^2 - x_i^2}, \quad \text{B.3}$$

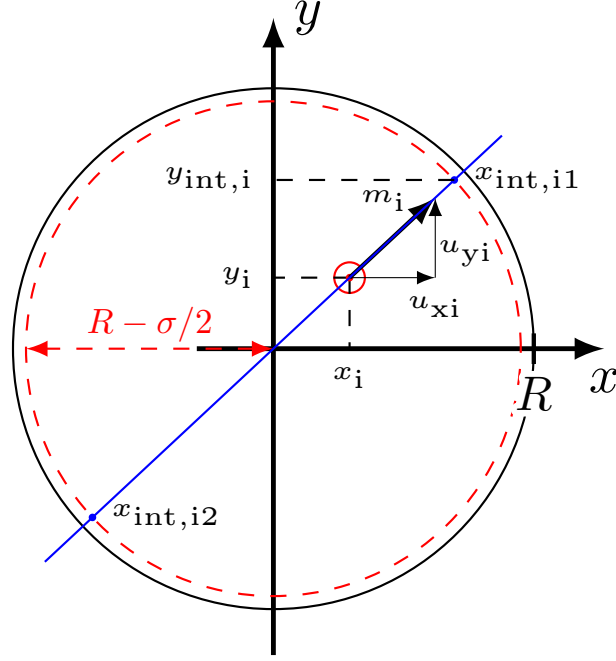


Figure B.1: Calculation of the collision point of a particle i , based on its velocity, with a cylindrical wall.

and the actual $y_{int,i}$ will depend on the sign of u_{yi} . By determining the Euclidean two-dimensional distance between the collision point $(x_{int,i}, y_{int,i})$ and the instantaneous location of the particle, the collision time with the wall t_{iw}^* can be obtained by knowing the particle velocity as

$$t_{iw}^* = t + \frac{\sqrt{(x_i - x_{int,i})^2 + (y_i - y_{int,i})^2}}{\sqrt{u_{xi}^2 + u_{yi}^2}}. \quad \text{B.4}$$

The wall collision time of each particle in the system is computed and compared with its current collision time in the information list. If the next event corresponds to this type of interaction, the post-collisional velocities are sampled from the Maxwell scattering kernel following the approach presented in [Appendix A](#). Based on this updated velocity, the next event for the colliding particle is sought so that the algorithm can continue.

Friction Coefficient from Equilibrium EDMD Simulations

The theoretical framework for the velocity slip is well defined, based on the Navier boundary condition (Navier, 1823). Its mathematical formulation, Eq. (1.11), contains two coefficients that need to be determined: the shear viscosity of the fluid and the fluid-wall friction coefficient. The shear viscosity can be easily computed from well-established experimental procedures, computer simulations, or theoretical correlations. On the other hand, the fluid-wall friction coefficient is not so well understood, as evidenced by the lack of first-principles theories for its analytical determination.

Furthermore, the experimental estimation of the interfacial friction coefficient is difficult, given the sub-nanometer scales at which the slip phenomena take place. Therefore, it has to be computed based on numerical studies, where molecular dynamics-like procedures in both non-equilibrium and equilibrium setups are a powerful tool. Non-equilibrium simulations imply the application of an external field to the system. However, one should be aware that, beyond the so-called linear regime, the slip processes heavily depend on the strength of the field. The caveat is that this threshold is not known on beforehand, and therefore one should run an extensive campaign to find a compromise for the external force value, namely large signal-to-noise ratio in the linear regime.

In order to overcome this challenge, simulations can be run in the external zero-force limit, i.e. in equilibrium conditions. In analogy to the better understood case of friction between solids, the hydrodynamic friction can be based on the shearing force between the the first fluid in layer in contact with the boundary of the system and the solid surface. In this Appendix, we present the approach introduced in Hansen et al. (2011), which consists on modelling the fluctuating dynamics of a fluid volume element adjacent to the wall, referred to as slab, of width Δ . For sufficiently small relative velocities between this slab (u_s) and the wall, essentially the velocity slip, the friction kernel ζ_Δ can be found from the generalised Langevin equation

$$F_w(t) = - \int_0^t \zeta_\Delta(t - \tau) u_s(\tau) d\tau + F_r(t), \quad \text{C.1}$$

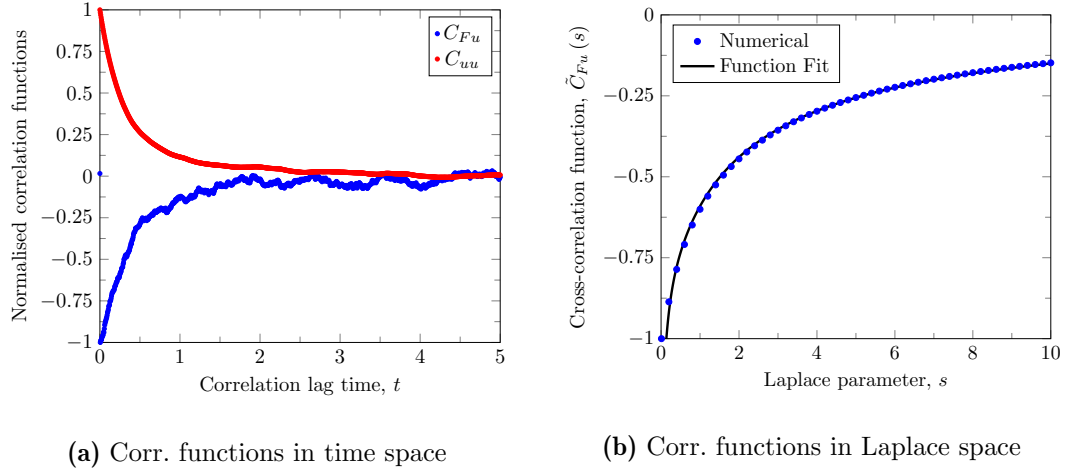


Figure C.1: The correlation functions are normalised with respect to their maximum absolute value. **(a)** Example of the two correlation functions, showing that decorrelation occurs for short times. **(b)** Numerical Laplace transformation of the force-velocity correlation function, together with the best fit of the memory function.

where F_w is the shear force exerted by the wall on the fluid (or viceversa) and F_r is a random force term with zero mean, that is uncorrelated with the slab velocity at earlier times. For steady flows, the time average of Eq. C.1 reads $\langle F_w \rangle = -\zeta_{0,\Delta} u_s$, namely, the first term in the right hand side of the force balance summarised in Eq. (5.6).

Now, if one takes the scalar product of Eq. C.1 with $u_s(0)$ and produces the ensemble average, an expression for the force-velocity cross-correlation function $C_{Fu}(t)$ is derived

$$\langle F_w(t) u_s(0) \rangle = C_{Fu}(t) = - \int_0^t \zeta_{\Delta}(t-\tau) \langle u_s(\tau) u_s(0) \rangle d\tau, \quad \text{C.2}$$

as a function of the slab velocity autocorrelation function $C_{uu}(t) = \langle u_s(t) u_s(0) \rangle$. These correlation functions are easy to quantify in equilibrium simulations, based on the construction of series for the fluid-wall tangential force and the velocity slip at different times. Some archetypical examples of these correlation functions are presented in Figure C.1a, where it is observed that the force and the velocity slip are anticorrelated as $C_{Fu}(t) < 0$ (the wall shear force acts in the opposite direction to the slab velocity), and that the autocorrelation function for the velocity slip quickly decays to zero.

This approach differs from the original conceptualisation of Navier, which considers the friction on a plane (the fluid-wall interface) rather than in a volume. Nevertheless, both approaches are equivalent as it is detailed in Section 5.2.1. As might be expected, the correlation functions depend in a non-trivial way on the width of the slab under consideration. For large Δ values, the force and velocity terms will include not just frictional forces from the fluid-wall interactions, but also hydrodynamic ones of viscous

nature arising from the bulk of the fluid. On the other hand, for small Δ values, the statistical accuracy will be affected owing to the small number of molecules in the region. Furthermore, the methodology presented in this Appendix is expected to work for cases where the density fluctuations are not significant. Thus, the slab-based methodology is invalid for dilute systems, where the flow description obeys kinetic theory precepts (Kennard, 1938), and an analytical expression for the friction coefficient can be obtained from the Maxwell studies on the boundary condition, see Eq. (5.18).

One can transform Eq. C.2, i.e. an integral in the time domain, into a more convenient algebraic expression by following the convolution theorem, which involves a numerical Laplace transformation into the s -domain

$$\tilde{C}_{Fu}(s) = -\tilde{\zeta}_{\Delta}(s) \tilde{C}_{uu}(s), \quad \text{C.3}$$

where s is the Laplace coordinate. Technically, one could produce the steady state-based $\tilde{\zeta}_{0,\Delta}$ directly from Eq. C.3, although this leads to poor statistics and an alternative approach has to be devised. In order to extract the friction coefficient, we follow here the methodology reported in Varghese et al. (2021). It assumes that the friction coefficient can be approximated by a one-term Maxwellian memory function $\zeta_{\Delta}(t) = b_1 e^{-a_1 t}$ with two fitting parameters b_1 and a_1 (see Figure C.1b), whose Laplace transform reads

$$\tilde{\zeta}_{\Delta}(s) = \frac{b_1}{s + a_1}. \quad \text{C.4}$$

If one integrates Eq. C.3 along the Laplacian domain, from an arbitrary minimum c_1 to an arbitrary maximum c_2 , then Eq. C.4 can be rearranged as

$$\int_{c_1}^{c_2} \frac{s + a_1}{b_1} ds = - \int_{c_1}^{c_2} \frac{\tilde{C}_{uu}(s)}{\tilde{C}_{Fu}(s)} ds = \frac{1}{b_1} \left[\frac{c_2^2 - c_1^2}{2} + a_1 (c_2 - c_1) \right], \quad \text{C.5}$$

where the ratio between the velocity autocorrelation and the force-velocity cross-correlation function can be numerically determined from equilibrium EDMD simulations. Since there are two fitting parameters, another equation is needed, which can be obtained by taking two different integral limits c_3 and c_4 . The interfacial fluid-solid friction coefficient is simply determined by taking into account the surface area of the wall A , as

$$\xi_{0,\Delta} = \frac{\zeta_{0,\Delta}}{A} = \frac{b_1}{a_1 A}. \quad \text{C.6}$$

The comparison between the friction coefficients obtained by this procedure and using non-equilibrium simulations is presented in Table 5.1 and Table 5.2. It can be observed that both procedures agree for large reduced densities η_0 , specifically when $\Delta > \lambda$ – that is, when the density fluctuations next to the walls are not important.

Bibliography

- Akhlaghi, H., Roohi, E., & Stefanov, S. (2023). A comprehensive review on micro- and nano-scale gas flow effects: Slip-jump phenomena, Knudsen paradox, thermally-driven flows, and Knudsen pumps. *Physics Reports*, 997, 1–60.
- Alafnan, S. F. (2022). The self-diffusivity of natural gas in the organic nanopores of source rocks. *Physics of Fluids*, 34(4).
- Alder, B. J., Gass, D. M., & Wainwright, T. E. (1970). Studies in molecular dynamics. VIII. The transport coefficients for a hard-sphere fluid. *The Journal of Chemical Physics*, 53(10), 3813–3826.
- Alder, B. J., & Wainwright, T. E. (1959). Studies in Molecular Dynamics. I. General Method. *The Journal of Chemical Physics*, 31(2), 459–466.
- Alder, B. J., & Wainwright, T. E. (1967). Velocity autocorrelations for hard spheres. *Physical Review Letters*, 18(23), 988–990.
- Allen, M. P., & Tildesley, D. J. (2017). *Computer Simulation of Liquids* (2nd ed.). Oxford University Press.
- Aoki, K., Giovangigli, V., & Kosuge, S. (2022). Boundary conditions for the Boltzmann equation from gas-surface interaction kinetic models. *Physical Review E*, 106(3), 1–25.
- Arkilic, E. B., Breuer, K. S., & Schmidt, M. A. (2001). Mass flow and tangential momentum accomodation in silicon micromachined channels. *Journal of Fluid Mechanics*, 437, 29–43.
- Arya, G., Chang, H. C., & Maginn, E. J. (2003). Knudsen diffusivity of a hard sphere in a rough slit pore. *Physical Review Letters*, 91(2), 026102/1–026102/4.
- Bahukudumbi, P., & Beskok, A. (2003). A phenomenological lubrication model for the entire Knudsen regime. *Journal of Micromechanics and Microengineering*, 13(6), 873–884.
- Bannerman, M. N., Sargant, R., & Lue, L. (2011). DynamO: A free O(N) general event-driven molecular dynamics simulator. *Journal of Computational Chemistry*, 32(15), 3329–3338.

- Barker, J. A., & Henderson, D. (1967). Perturbation theory and equation of state for fluids. II. A successful theory of liquids. *The Journal of Chemical Physics*, 47(11), 4714–4721.
- Barrat, J. L., & Bocquet, L. (1999). Influence of wetting properties on hydrodynamic boundary conditions at a fluid/solid interface. *Faraday Discussions*, 119–127.
- Bhatia, S. K., Bonilla, M. R., & Nicholson, D. (2011). Molecular transport in nanopores: A theoretical perspective. *Physical Chemistry Chemical Physics*, 13(34), 15350–15383.
- Bird, G. A. (1994). *Molecular Gas Dynamics and the Direct Simulation of Gas Flows* (2nd ed.). Oxford University Press.
- Bitsanis, I., Vanderlick, T. K., Tirrell, M., & Davis, H. T. (1988). A tractable molecular theory of flow in strongly inhomogeneous fluids. *The Journal of Chemical Physics*, 89(5), 3152–3162.
- Bocquet, L. (2020). Nanofluidics coming of age. *Nature Communications*, 19(3), 254–256.
- Bocquet, L., & Barrat, J. L. (1995). Diffusive motion in confined fluids: Mode-coupling results and molecular-dynamics calculations. *Europhysics Letters*, 31(8), 455–460.
- Bocquet, L., & Barrat, J. L. (2007). Flow boundary conditions from nano- to micro-scales. *Soft Matter*, 3(6), 685–693.
- Bocquet, L., & Charlaix, E. (2010). Nanofluidics, from bulk to interfaces. *Chemical Society Reviews*, 39(3), 1073–1095.
- Boltzmann, L. E. (1872). Further Studies on the Thermal Equilibrium of Gas Molecules. In S. G. Brush & N. S. Hall (Eds.), *The kinetic theory of gases. an anthology of classic papers with historical commentary* (pp. 262–349). Imperial College Press.
- Bonilla, M. R., & Bhatia, S. K. (2011). The low-density diffusion coefficient of soft-sphere fluids in nanopores: Accurate correlations from exact theory and criteria for applicability of the Knudsen model. *Journal of Membrane Science*, 382(1-2), 339–349.
- Box, G., & Muller, M. E. (1958). A Note on the Generation of Random Normal Deviates. *The Annals of Mathematical Statistics*, 29(2), 610–611.
- Brey, J. J., Maynar, P., & García De Soria, M. I. (2016). Kinetic equation and nonequilibrium entropy for a quasi-two-dimensional gas. *Physical Review E*, 94(4), 1–4.

- Broadwell, J. E. (1964). Study of rarefied shear flow by the discrete velocity method. *Journal of Fluid Mechanics*, 19, 401–414.
- Brown, R. (1828). A brief account of Microscopical Observations made in the Months of June, July, and August, 1827, on the Particles contained in the Pollen of Plants; and on the general Existence of active Molecules in Organic and Inorganic Bodies. *The Philosophical Magazine and Annals of Philosophy*, 4(21), 161–173.
- Brunauer, S., Deming, L. S., Deming, W. E., & Teller, E. (1940). On a Theory of the van der Waals Adsorption of Gases. *Journal of the American Chemical Society*, 62(7), 1723–1732.
- Cao, B. Y., Sun, J., Chen, M., & Guo, Z. Y. (2009). Molecular momentum transport at fluid-solid interfaces in MEMS/NEMS: A review. *International Journal of Molecular Sciences*, 10(11), 4638–4706.
- Carnahan, N. F., & Starling, K. E. (1969). Equation of state for nonattracting rigid spheres. *The Journal of Chemical Physics*, 51(2), 635–636.
- Casanova, S., Mistry, S., Mazinani, S., Borg, M. K., Chew, Y. M., & Mattia, D. (2020). Enhanced nanoparticle rejection in aligned boron nitride nanotube membranes. *Nanoscale*, 12(41), 21138–21145.
- Cathles, L. M., Brown, L., Taam, M., & Hunter, A. (2012). A commentary on "The greenhouse-gas footprint of natural gas in shale formations" by R.W. Howarth, R. Santoro, and Anthony Ingraffea. *Climatic Change*, 113(2), 525–535.
- Celebi, K., Buchheim, J., Wyss, R. M., Droudian, A., Gasser, P., Shorubalko, I., ... Park, H. G. (2014). Ultimate permeation across atomically thin porous graphene. *Science*, 344(6181), 289–292.
- Cercignani, C., & Daneri, A. (1963). Flow of a Rarefied Gas between Two Parallel Plates. *Journal of Applied Physics*, 34(Number 12), 3509–3513.
- Cercignani, C., & Sernagiotto, F. (1966). Cylindrical poiseuille flow of a rarefied gas. *The Physics Of Fluids*, 9(1), 40–44.
- Chapman, S., & Cowling, T. (1952). *The Mathematical Theory of Non-Uniform Gases* (2nd ed.). Cambridge University Press.
- Chen, J., Yu, H., Fan, J., Wang, F., Lu, D., Liu, H., & Wu, H. (2017). Channel-width dependent pressure-driven flow characteristics of shale gas in nanopores. *AIP Advances*, 7(4).

- Chen, Y., Li, J., Datta, S., Docherty, S. Y., Gibelli, L., & Borg, M. K. (2022). Methane scattering on porous kerogen surfaces and its impact on mesopore transport in shale. *Fuel*, 316, 123259.
- Coasne, B. (2016). Multiscale adsorption and transport in hierarchical porous materials. *New Journal of Chemistry*, 40(5), 4078–4094.
- Corral-Casas, C., Gibelli, L., Borg, M. K., Li, J., Al-Afnan, S., & Zhang, Y. (2021). Self-diffusivity of dense confined fluids. *Physics of Fluids*, 33(8).
- Corral-Casas, C., Li, J., Borg, M. K., & Gibelli, L. (2022). Knudsen minimum disappearance in molecular-confined flows. *Journal of Fluid Mechanics*, 945, 1–12.
- Cracknell, R. F., Nicholson, D., & Gubbins, K. E. (1995). Molecular dynamics study of the self-diffusion of supercritical methane in slit-shaped graphitic micropores. *Journal of the Chemical Society, Faraday Transactions*, 91(9), 1377–1383.
- Cui, S. T. (2005). Molecular self-diffusion in nanoscale cylindrical pores and classical Fick’s law predictions. *Journal of Chemical Physics*, 123(5).
- Cussler, E. L. (2009). Diffusion in dilute solutions. In *Diffusion: Mass transfer in fluid systems* (3rd ed., pp. 13–55). Cambridge University Press.
- Cutchis, P., van Beijeren, H., Dorfman, J. R., & Mason, E. A. (1977). Enskog and van der Waals play hockey. *American Journal of Physics*, 45(10), 970–977.
- de Haro, M. L., & Garzó, V. (1993). On the Burnett equations for a dense monatomic hard-sphere gas. *Physica A: Statistical Mechanics and its Applications*, 197(1-2), 98–112.
- Din, X. D., & Michaelides, E. E. (1997). Kinetic theory and molecular dynamics simulations of microscopic flows. *Physics of Fluids*, 9(12), 3915–3925.
- Dyre, J. C. (2016). Simple liquids’ quasiuniversality and the hard-sphere paradigm. *Journal of Physics Condensed Matter*, 28(32).
- Eijkel, J. C., & van den Berg, A. (2005). Nanofluidics: What is it and what can we expect from it? *Microfluidics and Nanofluidics*, 1(3), 249–267.
- Einstein, A. (1956). *Investigations on the Theory of the Brownian Movement* (R. Fürth & A. D. Cowper, Eds.). Dover Publications.
- Enskog, D. (1922). Kinetic Theory of Heat Conduction, Viscosity, and Self-Diffusion in Compressed Gases and Liquids. In S. G. Brush (Ed.), *Kinetic theory. the chapman-enskog solution of the transport equation for moderately dense gases* (pp. 226–259). Pergamon Press.

- Epstein, M. (1967). A model of the wall boundary condition in kinetic theory. *AIAA Journal*, 5(10), 1797–1800.
- Erpenbeck, J., & Wood, W. (1991). Self-diffusion coefficient for the hard-sphere fluid. *Physical Review A*, 43(8), 4254–4261.
- Ewart, T., Perrier, P., Graur, I. A., & Méolans, J. G. (2007). Mass flow rate measurements in a microchannel, from hydrodynamic to near free molecular regimes. *Journal of Fluid Mechanics*, 584, 337–356.
- Falk, K., Coasne, B., Pellenq, R., Ulm, F. J., & Bocquet, L. (2015). Subcontinuum mass transport of condensed hydrocarbons in nanoporous media. *Nature Communications*, 6, 1–7.
- Falk, K., Sedlmeier, F., Joly, L., Netz, R. R., & Bocquet, L. (2010). Molecular origin of fast water transport in carbon nanotube membranes: Superlubricity versus curvature dependent friction. *Nano Letters*, 10(10), 4067–4073.
- Fayon, P., & Sarkisov, L. (2019). Structure and dynamics of water in molecular models of hydrated polyvinylamine membranes. *Physical Chemistry Chemical Physics*, 21(48), 26453–26465.
- Fick, A. (1855). Ueber Diffusion. *Annalen der Physik*, 94(1), 59–86.
- Fihri, A., Bouhrara, M., Nekoueishahraki, B., Basset, J. M., & Polshettiwar, V. (2011). Nanocatalysts for Suzuki cross-coupling reactions. *Chemical Society Reviews*, 40(10), 5181–5203.
- Firouzi, M., & Wilcox, J. (2013). Slippage and viscosity predictions in carbon micropores and their influence on CO₂ and CH₄ transport. *Journal of Chemical Physics*, 138(6).
- Fischer, J., & Methfessel, M. (1980). Born-Green-Yvon approach to the local densities of a fluid at interfaces. *Physical Review A*, 22(6), 2836–2843.
- Fratantonio, D., Rojas-Cárdenas, M., Barrot, C., Baldas, L., & Colin, S. (2020). Velocity measurements in channel gas flows in the slip regime by means of molecular tagging velocimetry. *Micromachines*, 11(4).
- Frezzotti, A. (1997). A particle scheme for the numerical solution of the Enskog equation. *Physics of Fluids*, 9(5), 1329–1335.
- Frezzotti, A. (1999). Monte Carlo simulation of the heat flow in a dense hard sphere gas. *European Journal of Mechanics, B/Fluids*, 18(1), 103–119.

- Frezzotti, A., & Gibelli, L. (2008). A kinetic model for fluid-wall interaction. *Proceedings of the Institution of Mechanical Engineers, Part C: Journal of Mechanical Engineering Science*, 222(5), 787–795.
- Frezzotti, A., Gibelli, L., & Lorenzani, S. (2005). Mean field kinetic theory description of evaporation of a fluid into vacuum. *Physics of Fluids*, 17(1).
- Frezzotti, A., Grosfils, P., & Toxvaerd, S. (2003). Evidence of an inverted temperature gradient during evaporation/condensation of a Lennard-Jones fluid. *Physics of Fluids*, 15(10), 2837–2842.
- Frezzotti, A., & Sgarra, C. (1993). Numerical analysis of a shock-wave solution of the Enskog equation obtained via a Monte Carlo method. *Journal of Statistical Physics*, 73(1-2), 193–207.
- Gad-el Hak, M. (1999). The Fluid Mechanics of Microdevices — The Freeman Scholar Lecture. *Journal of Fluids Engineering*, 121(March 1999), 5–33.
- Germanou, L., Ho, M. T., Zhang, Y., & Wu, L. (2020). Shale gas permeability upscaling from the pore-scale. *Physics of Fluids*, 32(10), 102012.
- Ghiroldi, G. P., & Gibelli, L. (2014). A direct method for the Boltzmann equation based on a pseudo-spectral velocity space discretization. *Journal of Computational Physics*, 258, 568–584.
- Gibelli, L. (2012). Velocity slip coefficients based on the hard-sphere Boltzmann equation. *Physics of Fluids*, 24(2).
- Graham, T. (1833). On the law of the diffusion of gases. *Philosophical Magazine Series* 3, 2(9), 175–190.
- Gu, X. J., & Emerson, D. R. (2009). A high-order moment approach for capturing non-equilibrium phenomena in the transition regime. *Journal of Fluid Mechanics*, 636, 177–216.
- Guo, Y., He, X., Huang, W., & Wang, M. (2019). Microstructure Effects on Effective Gas Diffusion Coefficient of Nanoporous Materials. *Transport in Porous Media*, 126(2), 431–453.
- Hadjiconstantinou, N. G. (2006). The limits of Navier-Stokes theory and kinetic extensions for describing small-scale gaseous hydrodynamics. *Physics of Fluids*, 18(11).
- Hadjiconstantinou, N. G. (2021). An atomistic model for the Navier slip condition. *Journal of Fluid Mechanics*, 912, 1–13.

- Hadjiconstantinou, N. G., & Swisher, M. M. (2022). On the equivalence of nonequilibrium and equilibrium measurements of slip in molecular dynamics simulations. *Physical Review Fluids*, 7(11), 1–10.
- Hahn, K., & Kärger, J. (1998). Deviations from the normal time regime of single-file diffusion. *Journal of Physical Chemistry B*, 102(30), 5766–5771.
- Hansen, J. S. (2022). *Nanoscale hydrodynamics of simple systems*. Cambridge University Press.
- Hansen, J. S., Todd, B. D., & Daivis, P. J. (2011). Prediction of fluid velocity slip at solid surfaces. *Physical Review E - Statistical, Nonlinear, and Soft Matter Physics*, 84(1), 1–8.
- Herrero, C., Omori, T., Yamaguchi, Y., & Joly, L. (2019). Shear force measurement of the hydrodynamic wall position in molecular dynamics. *The Journal of Chemical Physics*, 151(4), 041103.
- Heyes, D. M., Cass, M. J., Powles, J. G., & Evans, W. A. (2007). Self-diffusion coefficient of the hard-sphere fluid: System size dependence and empirical correlations. *Journal of Physical Chemistry B*, 111(6), 1455–1464.
- Hiby, J., & Pahl, M. (1952). Der Einfluß von Zweierstößen auf die molekulare Gasströmung. *Z. Naturforschg.*, 7(a), 542–553.
- Hilbert, D. (1912). Begründung der kinetischen Gastheorie. *Mathematische Annalen*, 72, 562–577.
- Ho, M. T., Li, J., Su, W., Wu, L., Borg, M. K., Li, Z., & Zhang, Y. (2020). Rarefied flow separation in microchannel with bends. *Journal of Fluid Mechanics*, 901.
- Holt, J. K., Park, H. G., Wang, Y., Stadermann, M., Artyukhin, A. B., Grigoropoulos, C. P., ... Bakajin, O. (2006). Sub – 2-Nanometer Carbon Nanotubes. *Science*, 312(May), 1034–1038.
- Hummer, G., Rasaiah, J. C., & Noworyta, J. P. (2001). Water conduction through the hydrophobic channel of a carbon nanotube. *Nature*, 414(6860), 188–190.
- Israelachvili, J. N. (2011). Solvation, entropic, structural, and hydration forces. In J. N. Israelachvili (Ed.), *Intermolecular and surface forces* (Third ed., p. 341–380). Boston: Academic Press.
- Janssen, L. M. (2018). Mode-coupling theory of the glass transition: A primer. *Frontiers in Physics*, 6, 1–18.

- Joshi, R. K., Carbone, P., Wang, F. C., Kravets, V. G., Su, Y., Grigorieva, I. V., ... Nair, R. R. (2014). Precise and ultrafast molecular sieving through graphene oxide membranes. *Science*, 343(6172), 752–754.
- Kannam, S. K., Todd, B. D., Hansen, J. S., & Daivis, P. J. (2012). Interfacial slip friction at a fluid-solid cylindrical boundary. *Journal of Chemical Physics*, 136(24).
- Kärger, J., & Valiullin, R. (2013). Mass transfer in mesoporous materials: The benefit of microscopic diffusion measurement. *Chemical Society Reviews*, 42(9), 4172–4197.
- Karniadakis, G., Beskok, A., & Aluru, N. (2005). Simple fluids in nanochannels. In *Microflows and nanoflows: Fundamentals and simulation* (pp. 365–406). New York, NY: Springer.
- Kavokine, N., Netz, R. R., & Bocquet, L. (2021). Fluids at the Nanoscale: From Continuum to Subcontinuum Transport. *Annual Review of Fluid Mechanics*, 53, 377–410.
- Kazemi, M., & Takbiri-Borujeni, A. (2016). Non-equilibrium molecular dynamics simulation of gas flow in organic nanochannels. *Journal of Natural Gas Science and Engineering*, 33, 1087–1094.
- Kennard, E. H. (1938). *Kinetic Theory of Gases, with an Introduction to Statistical Mechanics*. New York: McGraw-Hill.
- Kjellander, R., & Sarman, S. (1991). Pair correlations of non-uniform hard-sphere fluids in narrow slits and the mechanism of oscillatory solvation forces. *Journal of the Chemical Society, Faraday Transactions*, 87(12), 1869–1881.
- Knudsen, M. (1909). Die Gesetze der Molekularströmung und der inneren Reibungsströmung der Gase durch Röhren. *Annalen der Physik*, 333(1), 75–130.
- Koffman, L. D., Plesset, M. S., & Lees, L. (1984). Theory of evaporation and condensation. *Physics of Fluids*, 27(4), 876–880.
- Krekelberg, W. P., Shen, V. K., Errington, J. R., & Truskett, T. M. (2011). Impact of surface roughness on diffusion of confined fluids. *Journal of Chemical Physics*, 135(15).
- Krekelberg, W. P., Siderius, D. W., Shen, V. K., Truskett, T. M., & Errington, J. R. (2017). Position-Dependent Dynamics Explain Pore-Averaged Diffusion in Strongly Attractive Adsorptive Systems. *Langmuir*, 33(49), 13955–13963.

- Kremer, G. M. (2010). *An Introduction to the Boltzmann Equation and Transport Processes in Gases*. Springer Berlin Heidelberg.
- Kremer, G. M., & Rosa, E. (1988). On Enskog's dense gas theory. I. The method of moments for monatomic gases. *The Journal of Chemical Physics*, 89(5), 3240–3247.
- Kuščer, I. (1971). Reciprocity in scattering of gas molecules by surfaces. *Surface Science*, 25(2), 225–237.
- Leal, L. G. (2007). Basic Principles. In *Advanced transport phenomena. fluid mechanics and convective transport processes* (pp. 13–109). Cambridge University Press.
- Lei, W., Rigozzi, M. K., & McKenzie, D. R. (2016). The physics of confined flow and its application to water leaks, water permeation and water nanoflows: A review. *Reports on Progress in Physics*, 79(2), 25901.
- Li, J., Cai, C., & Li, Z. H. (2021). Knudsen diffusion differs from Fickian diffusion. *Physics of Fluids*, 33(4).
- Liang, T., & Li, Q. (2019). Accurate modeling of Knudsen diffusion in nanopores using a physical-based boundary model. *Journal of Applied Physics*, 126(8).
- Lichter, S., Roxin, A., & Mandre, S. (2004). Mechanisms for liquid slip at solid surfaces. *Physical Review Letters*, 93(8), 1–4.
- Liu, H., Silva, C. M., & Macedo, E. A. (1998). Unified approach to the self-diffusion coefficients of dense fluids over wide ranges of temperature and pressure - Hard-sphere, square-well, Lennard-Jones and real substances. *Chemical Engineering Science*, 53(13), 2403–2422.
- Liu, P., Harder, E., & Berne, B. J. (2004). On the calculation of diffusion coefficients in confined fluids and interfaces with an application to the liquid-vapor interface of water. *Journal of Physical Chemistry B*, 108(21), 6595–6602.
- Liu, W., Tang, G., Su, W., Wu, L., & Zhang, Y. (2018). Rarefaction throttling effect: Influence of the bend in micro-channel gaseous flow. *Physics of Fluids*, 30(8), 082002.
- Liu, Z., Lin, X., Lee, J. Y., Zhang, W., Han, M., & Gan, L. M. (2002). Preparation and characterization of Platinum-based electrocatalysts on multiwalled carbon nanotubes for proton exchange membrane fuel cells. *Langmuir*, 18(10), 4054–4060.

- Lockerby, D. A., Reese, J. M., Emerson, D. R., & Barber, R. W. (2004). Velocity boundary condition at solid walls in rarefied gas calculations. *Physical Review E*, 70(1), 4.
- Lord, R. G. (1991). Some extensions to the Cercignani-Lampis gas-surface scattering kernel. *Physics of Fluids A*, 3(4), 706–710.
- Loucks, R. G., Reed, R. M., Ruppel, S. C., & Jarvie, D. M. (2009). Morphology, Genesis, and Distribution of Nanometer-Scale Pores in Siliceous Mudstones of the Mississippian Barnett Shale. *Journal of Sedimentary Research*, 79(12), 848–861.
- Lund, L. M., & Berman, A. S. (1966). Flow and self-diffusion of gases in capillaries. Part I. *Journal of Applied Physics*, 37(6), 2489–2495.
- MacElroy, J. M., Pozhar, L. A., & Suh, S. H. (2001). Self-diffusion in a fluid confined within a model nanopore structure. *Colloids and Surfaces A: Physicochemical and Engineering Aspects*, 187-188, 493–507.
- Majumder, M., Chopra, N., Andrews, R., & Hinds, B. J. (2005). Enhanced flow in carbon nanotubes. *Nature*, 438, 44.
- Martini, A., Roxin, A., Snurr, R. Q., Wang, Q., & Lichter, S. (2008). Molecular mechanisms of liquid slip. *Journal of Fluid Mechanics*, 600, 257–269.
- Mason, E. A., Malinauskas, A. P., & Evans, R. B. (1967). Flow and diffusion of gases in porous media. *The Journal of Chemical Physics*, 46(8), 3199–3216.
- Maxwell, J. C. (1860). Illustrations of the Dynamical Theory of Gases. Part I: On the Motions and Collisions of Perfectly Elastic Spheres. *The London, Edinburgh, and Dublin Philosophical Magazine and Journal of Science*, XIX (Fourth Series).
- Maxwell, J. C. (1867). IV. On the Dynamical Theory of Gases. *Philosophical Transactions of the Royal Society of London*, 157, 49–88.
- Maxwell, J. C. (1879). VII. On stresses in rarefied gases arising from inequalities of temperature. *Philosophical Transactions of the Royal Society of London*, 170, 231–156.
- McDermott, T. C., & MacElroy, J. M. (2004). Diffusion within a near-critical nanopore fluid. *Molecular Physics*, 102(19-20), 2113–2121.
- Mistry, S., Pillai, R., Mattia, D., & Borg, M. K. (2021). Untangling the physics of water transport in boron nitride nanotubes. *Nanoscale*, 13, 18096–18102.
- Mittal, J., Errington, J. R., & Truskett, T. M. (2006). Thermodynamics predicts how confinement modifies the dynamics of the equilibrium hard-sphere fluid. *Physical Review Letters*, 96(17), 1–4.

- Mittal, J., Errington, J. R., & Truskett, T. M. (2007). Does confining the hard-sphere fluid between hard walls change its average properties? *Journal of Chemical Physics*, 126(24).
- Mittal, J., Truskett, T. M., Errington, J. R., & Hummer, G. (2008). Layering and position-dependent diffusive dynamics of confined fluids. *Physical Review Letters*, 100(14), 9–12.
- Mon, K. K., & Percus, J. K. (2002). Self-diffusion on fluids in narrow cylindrical pores. *Journal of Chemical Physics*, 117(5), 2289–2292.
- Montanero, J. M., & Santos, A. (1996). Monte Carlo simulation method for the Enskog equation. *Physical Review E - Statistical Physics, Plasmas, Fluids, and Related Interdisciplinary Topics*, 54(1), 438–444.
- Murata, K., Mitsuoka, K., Hiral, T., Walz, T., Agre, P., Heymann, J. B., . . . Fujiyoshi, Y. (2000). Structural determinants of water permeation through aquaporin-1. *Nature*, 407(6804), 599–605.
- Navier, C. L. M. H. (1823). Mémoire sur les lois du Mouvement des Fluids. *Mémoires de l'Académie Royale des Sciences de l'Institut de France*, 389–440.
- Neto, C., Evans, D. R., Bonaccorso, E., Butt, H. J., & Craig, V. S. (2005). Boundary slip in Newtonian liquids: A review of experimental studies. *Reports on Progress in Physics*, 68(12), 2859–2897.
- Nordsieck, A., & Hicks, B. (1967). Monte Carlo Evaluation of the Boltzmann Collision Integral. *Rarefied Gas Dynamics*, 695–710.
- Obliger, A., Ulm, F. J., & Pellenq, R. (2018). Impact of Nanoporosity on Hydrocarbon Transport in Shales' Organic Matter. *Nano Letters*, 18(2), 832–837.
- Phan, A., Fan, D., & Striolo, A. (2020). Fluid transport through heterogeneous pore matrices: Multiscale simulation approaches. *Physics of Fluids*, 32(10), 101301.
- Philibert, J. (2005). One and a Half Century of Diffusion: Fick, Einstein, before and beyond. *Diffusion fundamentals*, 2(1), 1–10.
- Plimpton, S. (1995). Fast Parallel Algorithms for Short-Range Molecular Dynamics. *Journal of Computational Physics*, 117(1), 1–19.
- Pollard, W. G., & Present, R. D. (1948). On gaseous self-diffusion in long capillary tubes. *Physical Review*, 73(7), 762–774.
- Pöschel, T., & Schwager, T. (2005). Event-Driven Molecular Dynamics. In *Computational granular dynamics: Models and algorithms* (1st ed., pp. 135–189). Springer.

- Pranami, G., & Lamm, M. H. (2015). Estimating Error in Diffusion Coefficients Derived from Molecular Dynamics Simulations. *Journal of Chemical Theory and Computation*, 11(10), 4586–4592.
- Priezjev, N. V. (2007). Rate-dependent slip boundary conditions for simple fluids. *Physical Review E - Statistical, Nonlinear, and Soft Matter Physics*, 75(5), 1–7.
- Priezjev, N. V., & Troian, S. M. (2006). Influence of periodic wall roughness on the slip behaviour at liquid/ solid interfaces: Molecular-scale simulations versus continuum predictions. *Journal of Fluid Mechanics*, 554, 25–46.
- Roberts, G. T. (1971). The diffusive flow of gases between two parallel plates. *Journal of Physics A: General Physics*, 4(3), 401–412.
- Schmidt, M., & Löwen, H. (1997). Phase diagram of hard spheres confined between two parallel plates. *Physical Review E - Statistical Physics, Plasmas, Fluids, and Related Interdisciplinary Topics*, 55(6), 7228–7241.
- Schoen, M., Cushman, J. H., Diestler, D. J., & Rhykerd, C. L. (1988). Fluids in micropores. II. Self-diffusion in a simple classical fluid in a slit pore. *The Journal of Chemical Physics*, 88(2), 1394–1406.
- Secchi, E., Marbach, S., Niguès, A., Stein, D., Siria, A., & Bocquet, L. (2016). Massive radius-dependent flow slippage in carbon nanotubes. *Nature*, 537(7619), 210–213.
- Sendner, C., Horinek, D., Bocquet, L., & Netz, R. R. (2009). Interfacial water at hydrophobic and hydrophilic surfaces: Slip, viscosity, and diffusion. *Langmuir*, 25(18), 10768–10781.
- Shan, B., Wang, P., Wang, R., Zhang, Y., & Guo, Z. (2022). Molecular kinetic modelling of nanoscale slip flow using a continuum approach. *Journal of Fluid Mechanics*, 939, 1–31.
- Shannon, M. A., Bohn, P. W., Elimelech, M., Georgiadis, J. G., Mariñas, B. J., & Mayes, A. M. (2008). Science and technology for water purification in the coming decades. *Nature*, 452(7185), 301–310.
- Sharipov, F., & Seleznev, V. (1998). Data on internal rarefied gas flows. *Journal of Physical and Chemical Reference Data*, 27(3), 657–706.
- Shen, C. (2005). *Rarefied Gas Dynamics: Fundamentals, Simulations and Micro Flows*. Springer Berlin Heidelberg.
- Sheng, Q., Gibelli, L., Li, J., Borg, M. K., & Zhang, Y. (2020). Dense gas flow simulations in ultra-tight confinement. *Physics of Fluids*, 32(9), 092003.

- Shu, J. J., Bin Melvin Teo, J., & Kong Chan, W. (2017). Fluid velocity slip and temperature jump at a solid surface. *Applied Mechanics Reviews*, 69(2).
- Sigurgeirsson, H., & Heyes, D. M. (2003). Transport coefficients of hard sphere fluids. *Molecular Physics*, 101(3), 469–482.
- Simonnin, P., Noetinger, B., Nieto-Draghi, C., Marry, V., & Rotenberg, B. (2017). Diffusion under confinement: Hydrodynamic finite-size effects in simulation. *Journal of Chemical Theory and Computation*, 13(6), 2881–2889.
- Siria, A., Poncharal, P., Biance, A. L., Fulcrand, R., Blase, X., Purcell, S. T., & Bocquet, L. (2013). Giant osmotic energy conversion measured in a single transmembrane boron nitride nanotube. *Nature*, 494(7438), 455–458.
- Skoulidas, A. I., Ackerman, D. M., Johnson, J. K., & Sholl, D. S. (2002). Rapid Transport of Gases in Carbon Nanotubes. *Physical Review Letters*, 89(18), 13–16.
- Sone, Y. (2007). Slightly Rarefied Gas: Asymptotic Theory of the Boltzmann System for Small Knudsen Numbers. In *Molecular gas dynamics. theory, techniques and applications* (pp. 73–168). Birkhäuser Boston.
- Sparreboom, W., van den Berg, A., & Eijkel, J. C. (2010). Transport in nanofluidic systems: A review of theory and applications. *New Journal of Physics*, 12, 1–23.
- Speedy, R. J. (1987). Diffusion in the hard sphere fluid. *Molecular Physics*, 62(Number 2), 509–515.
- Spijker, P., Markvoort, A. J., Nedeia, S. V., & Hilbers, P. A. (2010). Computation of accommodation coefficients and the use of velocity correlation profiles in molecular dynamics simulations. *Physical Review E - Statistical, Nonlinear, and Soft Matter Physics*, 81(1), 1–15.
- Stokes, G. G. (1845). On the Theories of the Internal Friction of Fluids in Motion, and of the Equilibrium and Motion of Elastic Solids. *Transactions of the Cambridge Philosophical Society*, VIII, 287–341.
- Stokes, G. G. (1846). Report of Recent Researches in Hydrodynamics. *Report of the British Association*, I, 1–31.
- Struchtrup, H. (2005). *Macroscopic Transport Equations for Rarefied Gas Flows. Approximation Methods in Kinetic Theory*. Springer Berlin Heidelberg.
- Sutera, S. P. (1993). The History of Poiseuille’s Law. *Annual Review of Fluid Mechanics*(25), 1–19.

- Tatsios, G., Stefanov, S. K., & Valougeorgis, D. (2015). Predicting the Knudsen paradox in long capillaries by decomposing the flow into ballistic and collision parts. *Physical Review E - Statistical, Nonlinear, and Soft Matter Physics*, 91(6), 1–6.
- Tehver, R., Toigo, F., Koplik, J., & Banavar, J. R. (1998). Thermal walls in computer simulations. *Physical Review E - Statistical Physics, Plasmas, Fluids, and Related Interdisciplinary Topics*, 57(1), 17–20.
- Thomas, J. A., & McGaughey, A. J. H. (2008a). Density, distribution, and orientation of water molecules inside and outside carbon nanotubes. *Journal of Chemical Physics*, 084715(128), 1–6.
- Thomas, J. A., & McGaughey, A. J. H. (2008b). Reassessing Fast Water Transport Through Carbon Nanotubes. *Nano Letters*, 8(9), 2788–2793.
- Thompson, P. A., & Robbins, M. O. (1990). Shear flow near solids: Epitaxial order and flow boundary conditions. *Physical Review A*, 41(12), 6830–6837.
- Thompson, P. A., & Troian, S. M. (1997). A general boundary condition for liquid flow at solid surfaces. *Nature*, 389(6649), 360–362.
- Thomson, W. (1901). Nineteenth Century Clouds over the Dynamic Theory of Heat and Light. *The London, Edinburgh, and Dublin Philosophical Magazine and Journal of Science*, 2(7), 1–40.
- Travis, K. P., Todd, B. D., & Evans, D. J. (1997). Departure from Navier-Stokes hydrodynamics in confined liquids. *Physical Review E*, 55(4), 4288–4295.
- Tysanner, M. W., & Garcia, A. L. (2004). Measurement bias of fluid velocity in molecular simulations. *Journal of Computational Physics*, 196(1), 173–183.
- Valougeorgis, D., & Naris, S. (2003). Acceleration schemes of the discrete velocity method: Gaseous flows in rectangular microchannels. *SIAM Journal of Scientific Computing*, 25(2), 534–552.
- Varghese, S., Hansen, J. S., & Todd, B. D. (2021). Improved methodology to compute the intrinsic friction coefficient at solid-liquid interfaces. *Journal of Chemical Physics*, 154(18).
- Verbeek, M. G. (2010). Smoluchowski thermostat: A realistic introduction of the tangential momentum accommodation coefficient. *Physical Review E*, 81(4), 1–5.

- Wang, F. C., & Zhao, Y. P. (2011). Slip boundary conditions based on molecular kinetic theory: The critical shear stress and the energy dissipation at the liquid-solid interface. *Soft Matter*, 7(18), 8628–8634.
- Wang, G. J., & Hadjiconstantinou, N. G. (2015). Why are fluid densities so low in carbon nanotubes? *Physics of Fluids*, 27(5), 052006.
- Wang, G. J., & Hadjiconstantinou, N. G. (2019). Universal molecular-kinetic scaling relation for slip of a simple fluid at a solid boundary. *Physical Review Fluids*, 4(6), 1–10.
- Wertheim, M. S. (1963). Exact solution of the Percus-Yevick integral equation for hard spheres. *Physical Review Letters*, 10(8), 321–323.
- Whitby, M., Cagnon, L., Thanou, M., & Quirke, N. (2008). Enhanced fluid flow through nanoscale carbon pipes. *Nano Letters*, 8(9), 2632–2637.
- Wu, K., Chen, Z., Li, X., Guo, C., & Wei, M. (2016). A model for multiple transport mechanisms through nanopores of shale gas reservoirs with real gas effect-adsorption-mechanic coupling. *International Journal of Heat and Mass Transfer*, 93, 408–426.
- Wu, L., Liu, H., Reese, J. M., & Zhang, Y. (2016). Non-equilibrium dynamics of dense gas under tight confinement. *Journal of Fluid Mechanics*, 794, 252–266.
- Xiao, J., & Wei, J. (1992). Diffusion of Hydrocarbons Theory. *Chemical Engineering Science*, 47, 1123–1141.
- Yeh, I. C., & Hummer, G. (2004). System-size dependence of diffusion coefficients and viscosities from molecular dynamics simulations with periodic boundary conditions. *Journal of Physical Chemistry B*, 108(40), 15873–15879.
- Zhang, L., Shan, B., Zhao, Y., & Guo, Z. (2019). Review of micro seepage mechanisms in shale gas reservoirs. *International Journal of Heat and Mass Transfer*, 139, 144–179.